7/

Analysis of a Permanent Magnet Hybrid Linear Stepping Motor

by

Rong-Jie Wang

Dissertation submitted to the Faculty of Engineering, University of Cape Town, in fulfillment of the requirments for the degree of Master of Science in Engineering.

Cape Town, February 1998

Declaration

This thesis is submitted for the degree of Master of Science in Engineering in the Department of Electrical Engineering at the University of Cape Town. It has never been submitted before for any degree or examination at this or any other university. The author confirms that it is his unaided work. Portions of the work have been published in an international referred journal and conference proceedings. The author confirms that he was the primary researcher in all instances where work described in this thesis was published under joint authorship.

R. Wang

3 March 1998.

Acknowledgements

My sincere thanks to my supervisor, Prof. Jacek F. Gieras, for sharing his expertise and for his guidance throughout my research, and without whom this work would certainly not have been completed.

Many thanks to the University of Cape Town (UCT), Foundation of Research and Development (FRD) and Eskom Tertiary Education Support Program (TESP) for their financial assistance to the project.

Synopsis

Hybrid linear stepping motors (HLSMs) are regarded as an excellent solution to positioning systems that require a high accuracy and rapid acceleration. The advantages such as high efficiency, high throughput, mechanical simplicity, high reliability, precise open-loop operation, low inertia of the system, etc. have made this kind of motor more and more attractive in such applications as factory automation, high speed positioning, computer peripherals, numerically controlled machine tools and welding apparatus.

This motor drive is especially suitable for machine tools in which the positioning accuracy and repeatability are the key problems. Using the microprocessor controlled microstepping mode, a smooth operation with standard resolution of a few hundred steps/mm can be obtained.

Although rotating hybrid stepping motors are well covered by literature, there are only a few papers on HLSMs published so far [22, 24, 9, 31, 55, 39, 12]. The objective of this thesis is to apply the reluctance network approach (RNA) and the finite element method (FEM) to performance calculations of HLSMs. A comparison with the experimental measurements is done to evaluate advantages and disadvantages of these two methods.

The static characteristics show that the FEM demonstrates a better correlation with the experimental results than the RNA. The reason is that some assumptions have been made in order to obtain a simplified model in the RNA. The RNA, in general, tends to overestimate the forces.

In the case of instantaneous characteristics simulation, both the FEM and RNA compare favourably with the experimental data though the FEM gives more accurate (albeit underestimated) results. However, the RNA is a very efficient approach considering the computation time.

The optimisation of the finite element model is very important for obtaining the best possible results. The density of the finite element meshes, the aspect ratio of the elements and

reducing the problem in size by using symmetry are vital considerations. The studied HLSM possesses a very small airgap, which made a judicious mesh scheme extremely important. Different methods of force calculations were analysed and it was found that both the Coulomb's approach and the *Maxwell stress tensor* are efficient and accurate methods to implement. The classical virtual work CVW method is very time-consuming since it requires two solutions. The determination of small incremental displacement is also difficult in the CVW.

The experimental investigations of the small HLSM need a very high accuracy. Considerable efforts are needed to minimize all sources of noise and interference. It has been found that amplitude of instantaneous force ripple increases when the phase current amplitude increases. The superimposition of the $3rd$ harmonic on phase current can effectively reduce the force ripple.

The transient tests focused on the start-up and braking characteristics. The start-up tests show that the higher the load is applied the longer the start-up time is required. On the contrary, the braking time can be significantly reduced with an increase in load. It can also be concluded that the higher the step resolution, the less settling time is needed for both start-up and braking processes.

The recommendations from this thesis for further research on the subject of the HLSM analysis are that the reluctance network model should be improved to take into account the magnetic saturation and edge effects and the FEM enhanced classical approach should be attempted to take advantages of the high accuracy of the FEM without significant increase in the solution time.

Contents

List of Figures

List of Tables

List of Symbols

Symbols

$\vec{A}$	Magnetic vector potential
A_e	Magnetic vector potential value in an element
A_i	Magnetic vector potential at ith node
$\vec{B}$	Magnetic flux density
B_n	Normal component of magnetic flux density
B_t	Tangential component of magnetic flux density
B_r	Remanent magnetic flux density of permanent magnet
c_f	Machine constant of the HLSM
$\vec{D}$	Electric flux density
$\vec{E}$	Electric field intensity
$\mathcal{F}$	Energy functional in finite element method
$\mathcal{F}_{\mathcal{M}}$	Magneto-motive force (MMF) of the permanent magnet
$\mathcal{F}_{\mathcal{A}}$	Magneto-motive force (MMF) of the phase A
$\mathcal{F}_{\mathcal{B}}$	Magneto-motive force (MMF) of the phase B
$\mathcal{F}_{mmf}$	Overall magneto-motive force (MMF)
f_{air}	Air flow force
f_{em}	Electromagnetic force
F_{xp}	Tangential force per pole
F_x	Tangential force of the motor
F_y	Normal force of the motor
G	Jacobian matrix in finite element method
$\|G\|$	Determinant of Jacobian matrix G in finite element method
$\vec{H}$	Magnetic field intensity
h	Full length of permanent magnet in polarisation direction

i_A	Phase A current
i_B	Phase B current
$\vec{J}$	Current density
L	Thickness of the forcer
l	Integration path of the airgap in finite element method
l_{dvi}	Length of an airgap element
l_g	Airgap length
$\vec{M}$	Magnetisation vector
$\vec{M}_r$	Remanent magnetisation vector
N_c	Number of turns per winding
N_i	Shape function of the ith node
P	Permeance per tooth
P_{max}	Maximum permeance per tooth in one tooth pitch
P_{min}	Minimum permeance per tooth in one tooth pitch
$\Re$	Reluctance
$\Re_M$	Permanent magnet internal reluctance
$\Re_p$	Reluctance per pole
$\Re_t$	Reluctance of a pair of tooth
S	Cross-section area of permanent magnet
V_e	Volume of one element
$\vec{v}$	Velocity
W	Magnetic co-energy
W'	Magnetic energy
w	Axial length of the forcer
W_t	Tooth width
W_v	Slot width
x	Relative position between the forcer and platen
z_p	Number of teeth corresponding to the forcer length
Φ	Airgap magnetic flux per pole
Φ_M	Magnetic flux of permanent magnet
Φ_A	Magnetic flux of phase A
Φ_B	Magnetic flux of phase B
ϕ	Load angle

ϵ	Electric permittivity
μ_o	Primary magnetic constant
μ	Magnetic permeability
μ_r	Relative permeability of permanent magnet
τ	Tooth pitch
σ	Electric conductivity
σ_n	Normal stress
σ_t	Tangential stress
ρ	Electric charge density
ν	Reluctivity

Abbreviations

CAD	Computer-aided design
CVW	Classical virtual work
EMF	Electromotive force
EMI	Electromagnetic interference
FE	Finite element
FEA	Finite element approach
FEM	Finite element method
FFT	Fast Fourier transform
HLSM	Hybrid linear stepping motor
LPM	Linear pulse motor
LSM	Linear stepping motor
MMF	Magneto-motive force
PCB	Printed circuit board
PM	Permanent magnet
PWM	Pulse-width modulation
RNA	Reluctance network approach
RNM	Reluctance network method
VR	Variable reluctance

Chapter 1

Introduction

1.1 Objective

The purpose of this thesis is to analyse a hybrid linear stepping motor (HLSM) using:

1. Classical approach, i.e. reluctance (permeance) network approach
2. Finite element method (FEM)
3. Experimental tests.

By comparing the results of the classical approach and the FEM with measurements taken, the advantages and disadvantages of both approaches can be realized.

The HLSM is a new type of machine, it was first described in the early 1970s [16, 15] where the name, *Sawyer linear motor*, was used. The theory of this type of machine still needs development and experimental verification.

The HLSM produces the highest thrust when compared with other linear electric motors such as the linear induction motors (LIM), synchronous motors and d.c. motors. This aspect makes it advantageous in many applications of industry and factory automation systems.

1.2 Motor construction and operation principle

1.2.1 Electro-mechanical system

A HLSM operates on the same electromagnetic principle as its rotary hybrid counterpart. The moving component of the HLSM is called the armature or *forcer* into which all permanent magnets (PMs) and control windings are incorporated. The *platen* is a passive steel bar (with

teeth) which must be manufactured with high accuracy (a physical HLSM is shown in Fig 1.1). The main magnetic flux penetrates from the N-pole of the PM into a laminated steel core, through toothed pole faces, then across the airgap, through the platen pole faces (also toothed), along the platen back steel, through the other sides pole faces, across the airgap and back to the S-pole of the PM via the other core.

With the rapid development of magnetic materials [36, 3], the price of rare-earth PMs have been dropping a lot. Thus, HLSMs often use rare-earth PMs to achieve high available force, more compact structure and high force inertial ratio therefore high positioning accuracy.

When the field winding is fed with a current, the resulting magnetic field has the tendency to reinforce PM magnetic flux at one pole face and weaken it at the other. The face receiving the highest flux concentration will attempt to align its teeth with the platen to minimize the reluctance. Each phase has two toothed poles. They are outer narrow poles and inner wide poles with windings. Two narrow poles are equivalent to one wide inner pole. Four sets of teeth on the forcer are spaced in such a way that only one set can be perfectly aligned with platen teeth for each step (Fig. 1.2).

By applying currents to the corresponding field winding, it is possible to concentrate flux at one of the four pole faces. This will result in forcer motion at one tooth interval to either right or left hand side. Fig 1.3 demonstrates the flux distribution of an energised HLSM with right moving tendency.

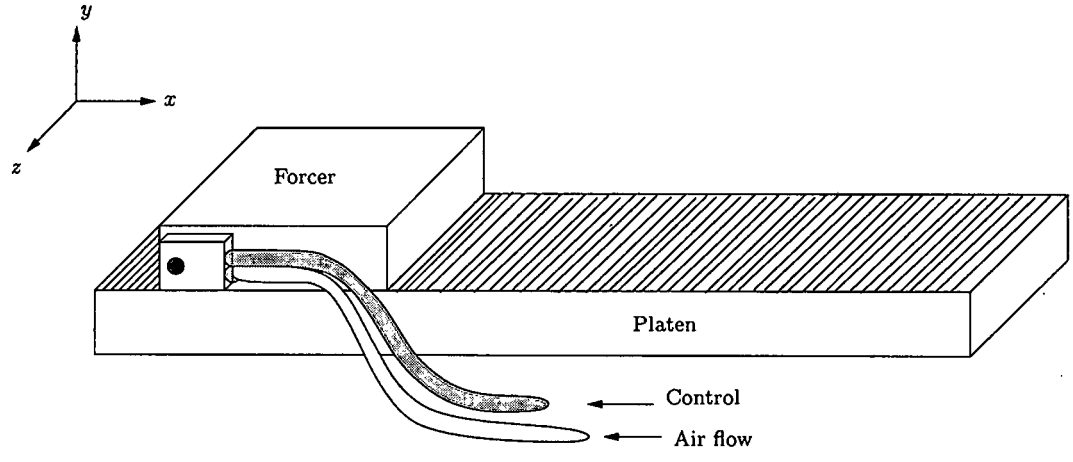

Figure 1.1: An arrangement of a HLSM with air cushion.

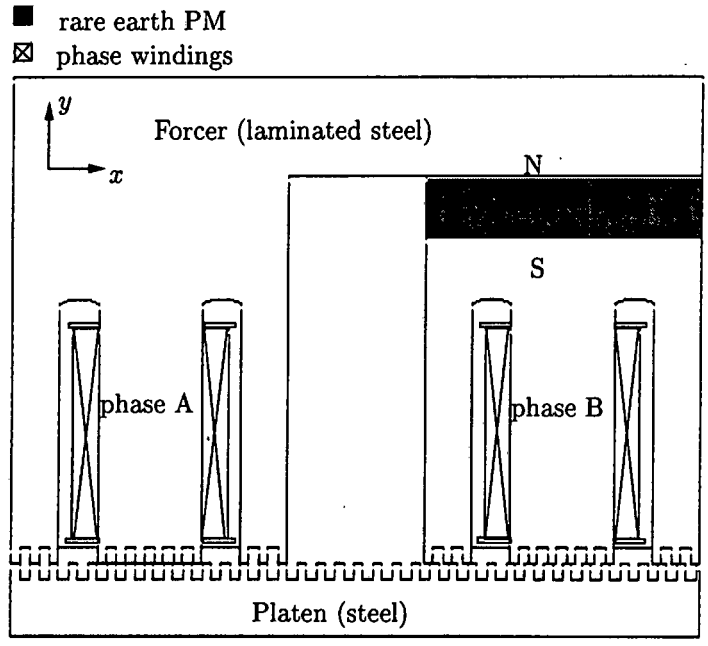

Figure 1.2: Longitudinal section of one stack of the HLSM.

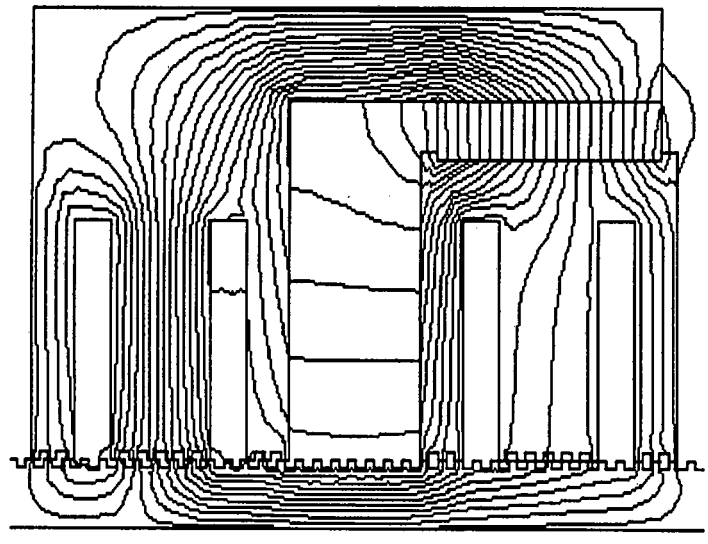

Figure 1.3: An energised HLSM with the forcer moving right.

1.2.2 Mechanical and energy balance equations

A clearance between the forcer and the platen is generated and kept by applying strong air flow to counteract the magnetic attraction. The force of air bearing increases as the airgap length decreases. The electromagnetic force varies with the excitation current, airgap length and relative tooth position on the platen. So the vertical force balance is actually a dynamic balance and can be expressed by the following equation:

$$f_{air}(y) \pm mg - f_{em}(i_A, i_B, x, y) = m\frac{\partial^2 y}{\partial t^2} \tag{1.1}$$

where f_{air} and f_{em} are air flow and electromagnetic force, respectively. The x is the tangential coordinate, y is the normal coordinate (according to Fig 1.2), mg is the gravitational force of forcer, and i_A and i_B are the forcer excitation currents.

The energy balance equation for tangential forces in the x direction is written as :

$$e_A i_A + e_B i_B = f_x(i_A, i_B, x, y)\frac{dx}{dt} + \frac{d}{dt}(\frac{1}{2}i_A^2 L_A + \frac{1}{2}i_B^2 L_B) \tag{1.2}$$

The EMFs e_A and e_B induced in each phase winding are the sums of EMFs generated by the PM flux linking the phase winding and the EMFs caused by phase currents i_A and i_B, i.e. $d(i_A L_A)/dt$ and $d(i_B L_B)/dt$. The force f_x is the instantaneous electromagnetic force in the x direction (thrust) developed by the HLSM.

The pulsation of current in the phase winding is a function of the linear speed v and tooth pitch τ, i.e. $\omega = v\pi/\tau$. The phase currents at no load for micro-stepping operation (subsection 1.2.4) are of the following forms:

$$i_A = \sum_n I_{mn}\sin(n\omega t) = \sum_n I_{mn}\sin(n\frac{v\pi}{\tau}t) \tag{1.3}$$

$$i_A = \sum_n I_{mn}\cos(n\omega t) = \sum_n I_{mn}\cos(n\frac{v\pi}{\tau}t) \tag{1.4}$$

Neglecting higher harmonics $n > 1$, the current in each phase can be regarded as sinusoidal, i.e. $i_A = I_{m1}\sin(\omega t)$ and $i_B = I_{m1}\cos(\omega t)$.

The force in the x direction (thrust) has two components: the stationary (synchronous) force and the force due to the variation of the phase inductances with displacement (reluctance force). In a practical HLSM the second component is negligible. With sinusoidal current in each phase and negligible variation of the phase inductance the force in the x direction can

be simply written as [21]

$$F_x = c_f z_p I_{m1} \sin\phi \tag{1.5}$$

where c_f is the constant dependent on the motor dimensions and the number of turns per phase, z_p is the number of platen teeth corresponding to the length of the forcer and ϕ is the load angle. This is a stationary force without cogging force being taken into account.

1.2.3 Controller

Within various drive technologies, the chopper regulation techniques are widely used in the stepper motor drive system. The pulse width modulation (PWM) and the thresh-hold modulation are two types of chopper regulations. The PWM controls the average of the motor current and is very effective for precise current control, while the thresh-hold modulation controls current to the peak level. The PWM is able to obtain higher accuracy than can be achieved by using simple thresh-hold system [21]. The block diagram of the L20 HLSM control system is shown in Fig 1.4. Table 1.1 outlines the general specifications of *Compumotor's L* type micro-stepping controller.

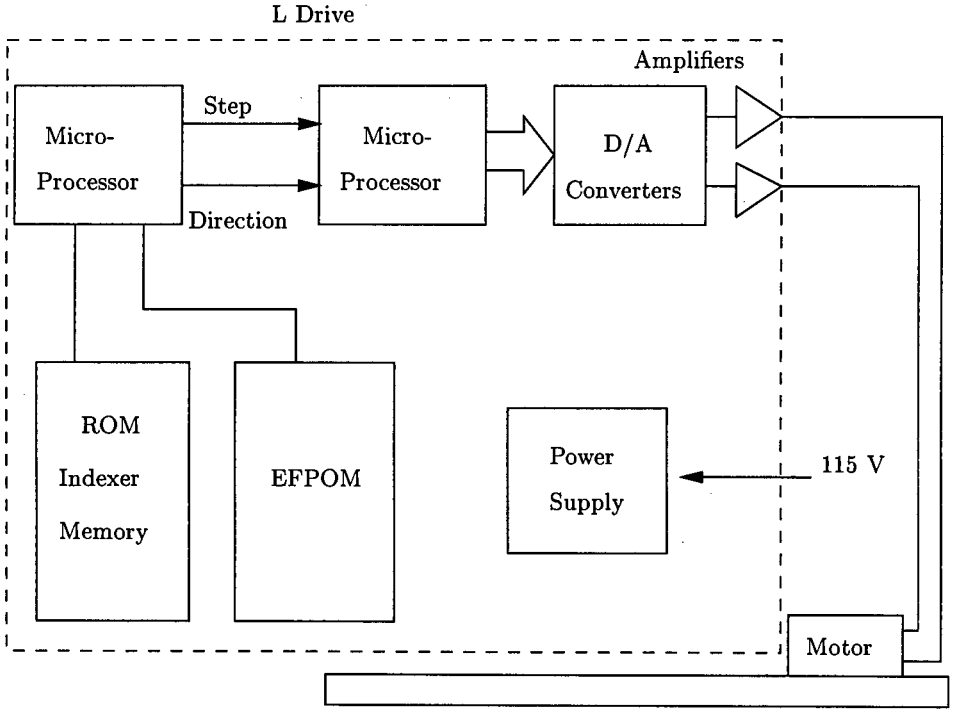

Figure 1.4: Block diagram of the HLSM control system

Table 1.1: Specifications of micro-stepping controller

Quantity	Value
Number of phases	2
Memory type	EPROM (1800 characters)
Repeatability	±0.0025 mm
Speed	2.5 m/s
Current rating	0-3 A (dipswitch selectable)
Power input	95-135 VAC 50/60 Hz
Motion program used	Power-up auto run (0.0508m/s)
Resolution	4 resolutions are built-in and dip selectable 5,000μstep/fullstep, 9,000μstep/fullstep 10,000μstep/fullstep, 12,500μstep/fullstep
Amplifiers type	20kHz fixed frequency PWM, current controlled, bipolar type MOSFET construction
Other function	Auto standby — 50% current reduction when motor not moving

1.2.4 Micro-stepping mode

When a two-phase stepping motor is driven in its full-step mode, both phases are energised at a time. In the half-step mode, the two phases are energised alternately as illustrated in Fig 1.5. It can be seen that energising both phases with equal currents produces an intermediate position half way between one-phase on positions. If the two phase currents are unequal, the forcer will be shifted to the stronger motor position. So it is possible to subdivide one basic step into many small steps by proportioning the currents in the two windings. This method is known as the micro-stepping drive and is often applied to the HLSMs.

The idea of micro-stepping drive originally comes from the sinusoidal bipolar drive of a HLSM as a synchronous machine. If a HLSM is driven from a two-phase sine wave supply, it is supposed to be step-less and very smooth. But in practical situation the step-less motion can not be achieved due to the detent effect, variable reluctance effects and other adverse effects [21]. Thus, it is necessary to adopt micro-stepping mode. The excitation current pattern in the winding closely resembles two sine waves with a 90^o phase shift between them as shown in Fig 1.6. In this way, the step size is reduced and the low-speed smoothness is greatly improved. However, accurate micro-stepping places increased demands on the accuracy of the current control in the drive, particularly at low current levels. This requires the PWM technique being used.

The phase currents necessary to generate the intermediate steps following a sinusoidal

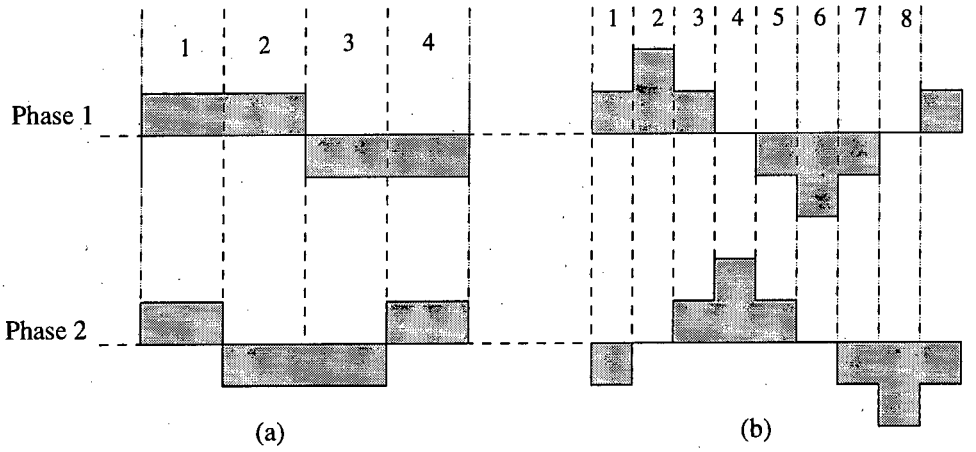

Figure 1.5: Phase current profiles in (a) full step and (b) half step modes.

profile. However, the same profile will not produce the optimum response with different types of motors. So a mini-stepping drive needs to have provision for adjusting the current profile. The intermediate current levels are stored as data in the EPROM of the L20 controller, with some means of selecting alternative data sets to supply different current profiles.

The change in the profile is realized in terms of adding or subtracting a third-harmonic component to or from the basic sine wave which is capable of reducing the adverse effects such as variable reluctance effect, detenting effect and sub-harmonics in the induced voltage. Under micro-stepping mode, the studied HLSM can get a resolution as high as 492 steps/mm.

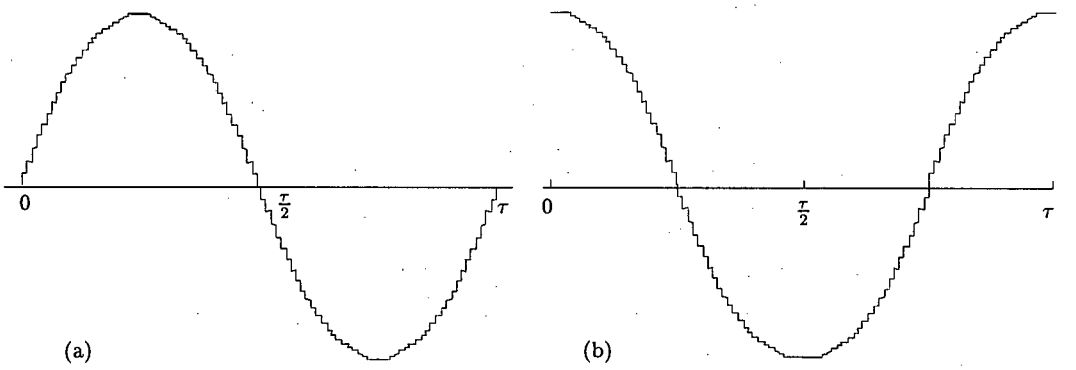

Figure 1.6: A sinusoidal step-wave current for the micro-stepping drive, where (a) and (b) represent phases A and B, respectively.

1.3 Applications of HLSMs

Linear stepping motor (LSM) is designed to perform linear motion. It converts a digital electric input into a mechanical motion. Compared with other devices that can perform the same or similar functions, a control system using a stepping motor has the following advantages:

1. No feedback is normally required for either position control or speed control
2. Positional error is non-cumulative
3. High thrust output can be realised
4. Stepping motors are compatible with the modern digital equipment

For these reasons, various types of stepping motors have been used in computer peripherals, numerically controlled machine tools, robotics, auto-welding, control rod drives in nuclear reactors, etc.

Basically, linear motors offer solutions to a variety of applications that require high-speed, low mass moves, the linear motor is an alternative to conventional rotary-to-linear conversion devices such as leadscrews, rack and pinion. belt drives, pneumatic and hydraulic actuators. However, they are not subject to the same linear velocity and acceleration limitations as in a system converting rotary to linear motion. Moreover, the speed, distance and acceleration are easily programmed in a highly repeatable fashion.

Additional benefits of the linear stepping motors include high throughout, mechanical simplicity, high reliability, long travel, low maintenance, small work envelope, easily-achieved X-Y motion and precise open-loop operation.

Fig 1.7 describes an experimental surface motor in Professor Yamada's laboratory at the Shinshu University [6]. This motor actually consists of four HLSMs, one pair of which are used to produce force in the X - direction while the other pair HLSMs in the Y - direction. Driving by a micro-stepping controller, the motor can travel in any direction on a stationary base.

Some already implemented or potential industrial applications are given as follows [34, 14, 21, 38]:

- Robots and manipulation
- Transfer systems

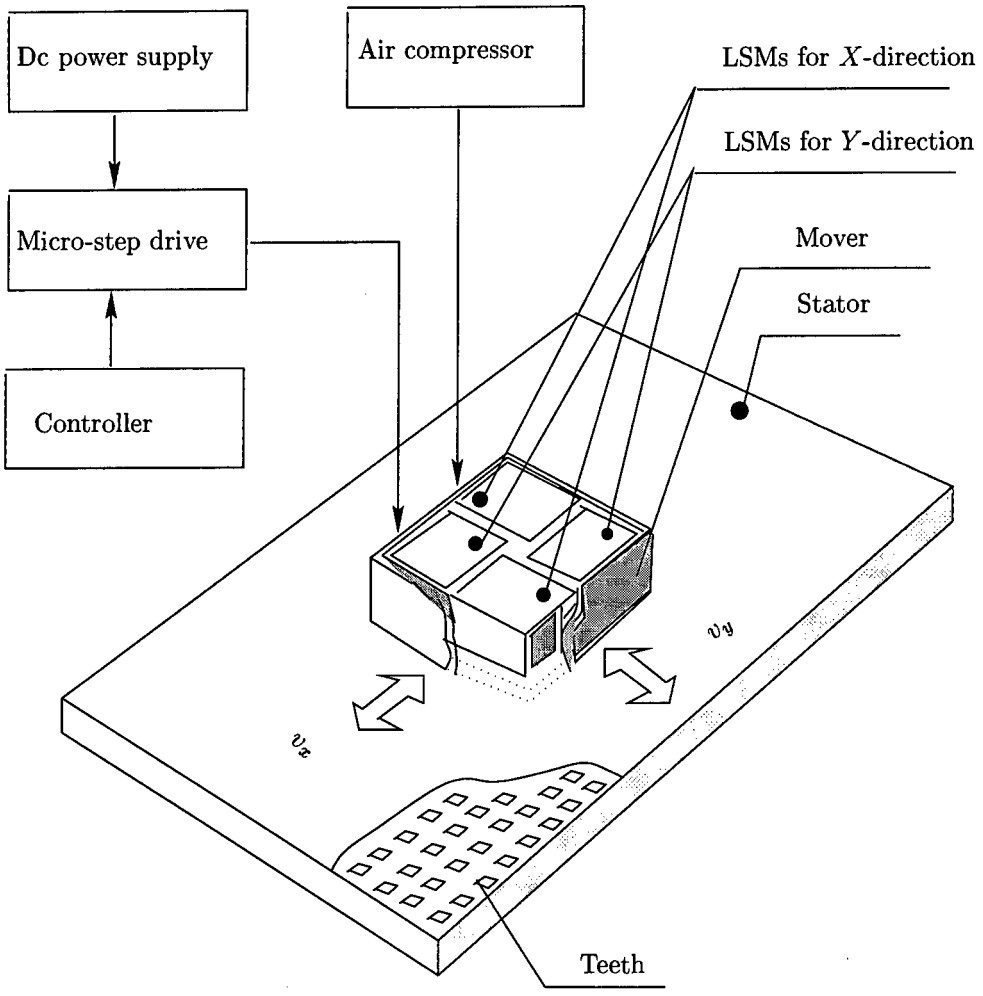

Figure 1.7: Surface motor consisting of four HLSMs with an air bearing (Shinshu University).

- Fibre optics manufacture
- Industrial sewing machines
- Semiconductor wafer processing
- Medical application (e.g. for artificial heart driving [51])
- $X - Y$ plotters and printing heads
- Light assembly automation and inspection
- Flying cutters, laser cut and trim systems
- Gauging, packaging and automotive manufacturing

- High speed linear positioning and velocity control
- Printed circuit board (PCB) assembly and inspection systems
- Water jet cutting, metering/dispensing and wire harness making
- Optical switching and alignment (e.g. optical switches and micromirrors carrier [54])
- Machine tools
- Vibration generator [20]
- Welding apparatus
- Factory automation systems

1.4 Literature review

1.4.1 Sawyer linear motor

The emergence of the stepping motor is owing to the two important patents claimed in 1919 and 1920, respectively [21]. Although the first description of a three-phase VR stepping motor was found in one issue of JIEE published in 1927, the practical application of modern stepping motors started in earlier days.

In pace with the advent of the digital control, a comprehensive research on stepping motors was started in academic institutions and laboratories of advanced industrial countries since 1950s. The first hybrid stepping motor appeared in 1952 in USA. Since then rapid progresses in the research have been bringing hybrid stepping motors into quite broad industrial applications.

It was not until 1969 that the earliest version of the HLSM, *Sawyer linear motor* (Fig 1.8) [16, 15], was introduced to improve linear motion capability and eliminate mechanical interface. There have been some published research about the HLSM [22, 24, 9, 31, 55, 39, 12] since then.

A lot of contribution [21] on stepping motors were made during this period. However, most of this research has been dedicated to the rotary stepping motor [1, 19, 21, 27, 29, 26, 48].

1.4.2 FEM analysis

Some of the literature dealt with modelling and analysis of HLSMs by using the FEM. Khan and Ivanov described the utilisation of the 2D FEM for modelling and computation of magnetic

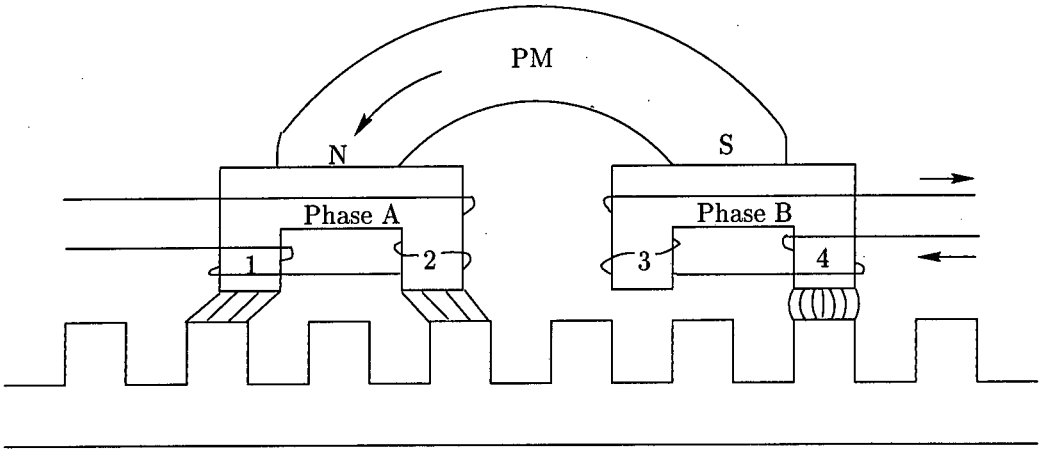

Figure 1.8: The Sawyer linear motor.

fields in a 4-phase cylindrical passive armature linear step motor used in control rod drives of nuclear reactors in [23]. The characteristic obtained by the FE modelling shows a better agreement with experimental one than that from analytical method.

Mezhinsky and Karpovich used a time-efficient FEM approach to predict the static and position error characteristic of a HLSM by modelling only one pair of teeth in their paper [31].

In general this method provides a comparatively cheap and accurate tool for the analysis and design of the HLSM except for the following:

- The FEM package capable of assigning boundary conditions in the terms of magnetic flux density is required
- The analysed motor should be structurally simple and symmetrical
- The adjacent poles with different polarities have no significant influence on the motor modelling

Apparently, all the presented motors are either possessing of a relatively big airgap (0.5 – 0.75mm) [24] and/or of a symmetric structure which can utilise full advantages of the FE computation without much adaptations. The main reasons for the unpopularity of applying the FEM to HLSMs are the presence of tiny airgaps [8] and that the motors often have asymmetric structures. These can cause great difficulties in FEM modelling and no easy way round this problem. It should also be mentioned that intensive research has been done on the applications of the FEM to electromagnetic problems by many authors [28, 5, 45, 7] since 1970s. Most of the FEM packages that are used today are based on this research.

Methods of modelling that can be applied to HLSMs have been discussed by J.L. Coulomb [7], K. Komeza [25], S. Mcfee [30], J. Mizia [32] etc. Classical virtual work needs two FE solutions to determine a single force/torque. However, Coulomb presented a one-solution virtual work method in 1983. This helps reducing computation efforts and also avoiding the round-off errors arisen from small displacement which is particular important to the FE modelling of HLSMs. As the author is aware there are no published works about implementation of this algorithm into FE analysis of HLSMs so far.

Several authors compared the different formulae for forces and torques computations and gave some practical conclusions about the advantages and disadvantages of different methods [11, 25, 30].

1.4.3 Reluctance network analysis

Another school of scholars researched into using the reluctance network approach (RNA) [9, 12, 55, 39, 24, 52, 35] for HLSMs analysis. Some of studied cases concerned only the symmetrically structured HLSMs [39, 35] and showed a reasonable agreement with the experimental results.

Khan et al [24] described a complicated analytical method for calculating static characteristic of a linear stepping motor (LSM). The proposed method is based on the RNA applied to phase magnetic circuit of the LSM. the reluctance of various parts of phase magnetic circuit was calculated analytically by assuming probable flux paths with consideration of complex nature of magnetic field distribution. Magnetic saturation was partially taken into accounted by an efficient iterative algorithm.

Ellerthorpe and Blaney [9] analysed an asymmetrical two-phase HLSM with air bearing by using a simplified approach to the air flow and permeance models. First the airgap was calculated by using these models and then the output forces were derived on the basis of coenergy method. It is an efficient approach except that the approximation of reluctance by sinusoidal functions was incorrect.

Because of the long computation time in the FEA and not accurate estimation of reluctances in classical RNA, some authors identified the need to combine the two methods in an attempt to obtain the best possible results with a reasonable computation time [18, 33]. This hybrid approach has also been extended to the CAD domain [53]. Generally speaking, the RNA is somewhat case sensitive and uncertainties and doubts in this commonly-used method still exist.

1.4.4 Experimental investigation

Although most of the published results were presented with some necessary experimental data, there are some Japanese papers paid more emphasis on the experimental investigations of the LSMs.

Basak et al [2] designed and tested a prototype of the novel slot-less LSM. Hirai et al [17] of Yaskawa Elec. Corp. described an experimental process for improving the transient response stability of two-axis Sawyer LSM in quick positioning applications. Sanada et al [44] proposed a new cylindrical LSM with an interior PM mover which has not only the ability of linear motion but also rotary motion. The basic characteristics was examined based on experimental results. Amongst others, Professor Yamada's team at Shinshu University undertook an comprehensive investigation of the reliability evaluation of the linear pulse motor (LPM) for artificial heart driving [51]. The LPM was put under accelerated-life testing.

1.4.5 Manufacturers of HLSMs

Nowadays, rotary stepping motors are manufactured in many countries. However, HLSMs are designed and manufactured only in USA, Japan and some European countries. The major manufacturers of HLSMs are American and Japanese companies.

There are more than 25 companies in U.S. which produce and/or deal with HLSMs. Some of them are specialised in designing and fabricating HLSMs (e.g. Northern Magnetics Inc., Compumotor Division of Parker Hannifin, American Precision Industries of Motion Technologies Group, etc). Most of internationally well-known companies in Japan such as Sanyo Denki, Nippon Pulse Motor, Minebea, Nippon Electric, Daini Seikosha, Fanuc Ltd. Yaskawa Elec. Corp. have specific divisions engaged in researching, designing and manufacturing HLSMs.

Chapter 2

Experimental Tests

2.1 General requirements

First step to the analysis of a HLSM is to obtain vital data and performances characteristics from experimental tests. The tested motor is relatively a new type machine and further theoretical analysis needs experimental verification.

An experimental investigation on a small electrical machine requires a high accuracy. All the measured parameters need to be transformed into measurable voltage or current signals. Considerable efforts are normally necessary to eliminate all sources of noise and interference which would cause the electro-magnetic interference EMI problem and influence the sensitive measuring instrumentations.

2.2 Testing bench

2.2.1 Motor and testing equipment

The tested HLSM is shown in Fig 2.1a. The arrangement of test bench including the motor, controller, compressor, storage scope, data acquisition system and other instruments is shown in Fig 2.1b. Design data of the HLSM manufactured by *Compumotor (USA)* [9, 37, 38] are given in Table 2.1.

Since the airgap maintained by strong air flow is variable and subject to increasing with higher air pressure, the precise control of air pressure is important. The recommended air pressure is around 275 kpa for unloaded forcer [37]. In practical measurements, a higher air pressure is first used. If the HLSM generates loud tune, this means too much air flow has been applied. Then the air flow can be reduced by turning down the regulator button until

Table 2.1: Design data of the tested HLSM.

Quantity	Value
Stack number	2
Coil number	4
Rated steady-state thrust	approx. 80 N
Maximum normal force	approx. 800 N
Maximum top load	22.7 kg
Accuracy (worst case)	±0.09 mm
Repeatability	±0.0025 mm
Default speed	0.0508 m/s
Peak current per phase	0–3 A (adjustable)
Airgap length	0.0127 mm
Platen tooth pitch	1.016 mm
Tooth width	0.4572 mm
Slot width	0.5588 mm
Number of turns per coil	57
The diameter of each wire	0.4572 mm
Magnet height	2.54 mm
Magnet length	12.7 mm
Permanent magnet type	NdFeB ($B_r = 1.23$T)
Forcer weight	0.8 Kg
Platen width	49.53 mm
Platen material	1018 steel
Forcer length	117.475 mm
Forcer material	laminated steel (0.3556mm thick)

Table 2.2: Specifications of the GM190 air compressor

Rated power	Voltage	Current	Frequency
1.1 kW	220 V	7 A	50 Hz
Volume	Compression rate	Max. operating pressure	Operating temperature
24 L	2860 rpm	800 kpa	$-10°C$ *to* $80°C$

the noise becomes unnoticeable. The compressor specifications are given in Table 2.2.

It has been observed that a big difference, sometimes up to 30% (the worst case), could occur between the same measurements taken at different time. The reasons are multifold: the variations in impedance and inductance of windings with temperature, the airgap fluctuation and the current shift of controller. To stabilise the tested motor, it is necessary to let the motor warm-up for some time. This is especially important when performing transient measurements.

When using accelerometer for transient measurements, it is preferred to use charge amplifier function which produces an output voltage proportional to the input charge since it can eliminate the influence of cable capacitance [41].

In Fig 2.2 a flow chart outlines the inter-connection of the equipment and the general procedures for measurements. An IBM compatible PC-based data acquisition system is used to sample all measurements. The HP54651A RS-232 interface module and optical link together with *ScopeLink* $v2.02$ software were installed to transfer and receive data between the computer and the storage scope. The sampling rate and number of samples are adjustable. The logged data from storage scope has been saved as a text file and then imported to other softwares such as *MathLab* and *GnuPlot* where a further data processing can be carried out.

2.2.2 Determination of the airgap length

Since the airgap length is a very important parameter for the simulation of the HLSM by using both the FEM and the classical circuit approach, it is necessary to find an accurate value of the airgap length on the basis of experimental measurements.

As described in Chapter 1, the airgap of the tested motor was generated and maintained by the strong air pressure, which is actually very small and variable. One of the techniques to evaluate the tiny airgap length is to use an opto-coupler in order to pick-up the amplitude difference between two electrical signals transferred from small variations in the airgap length. Then, the amplified signals are logged onto a storage scope and finally transferred to a PC-based data acquisition system. Fig 2.3 shows the experimental set-up for determining the small airgap of a HLSM.

It has been found that the airgap is actually varying in a certain range. When different excitation profiles are applied (e.g. current free state, one phase on and two phases on), there are always appreciable changes in the airgap length. To minimize the influences arise from the different excitation schemes, a set of air pressure values have been chosen to help keeping

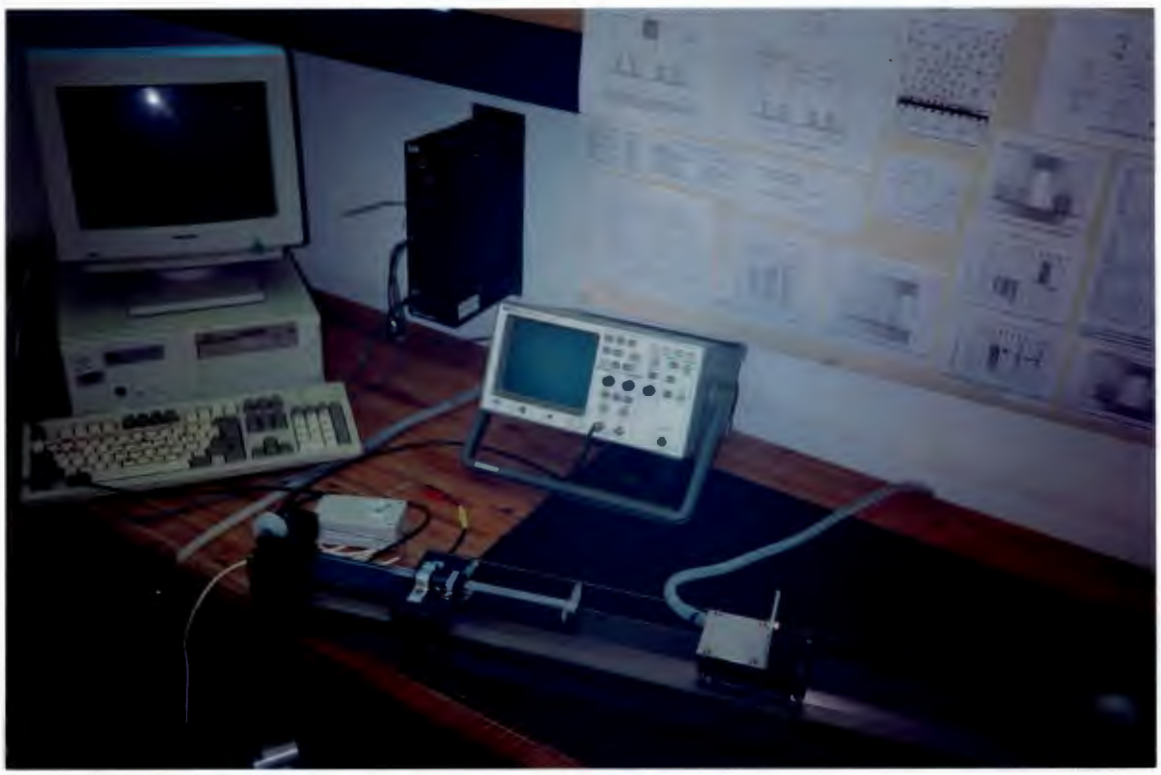

(a)

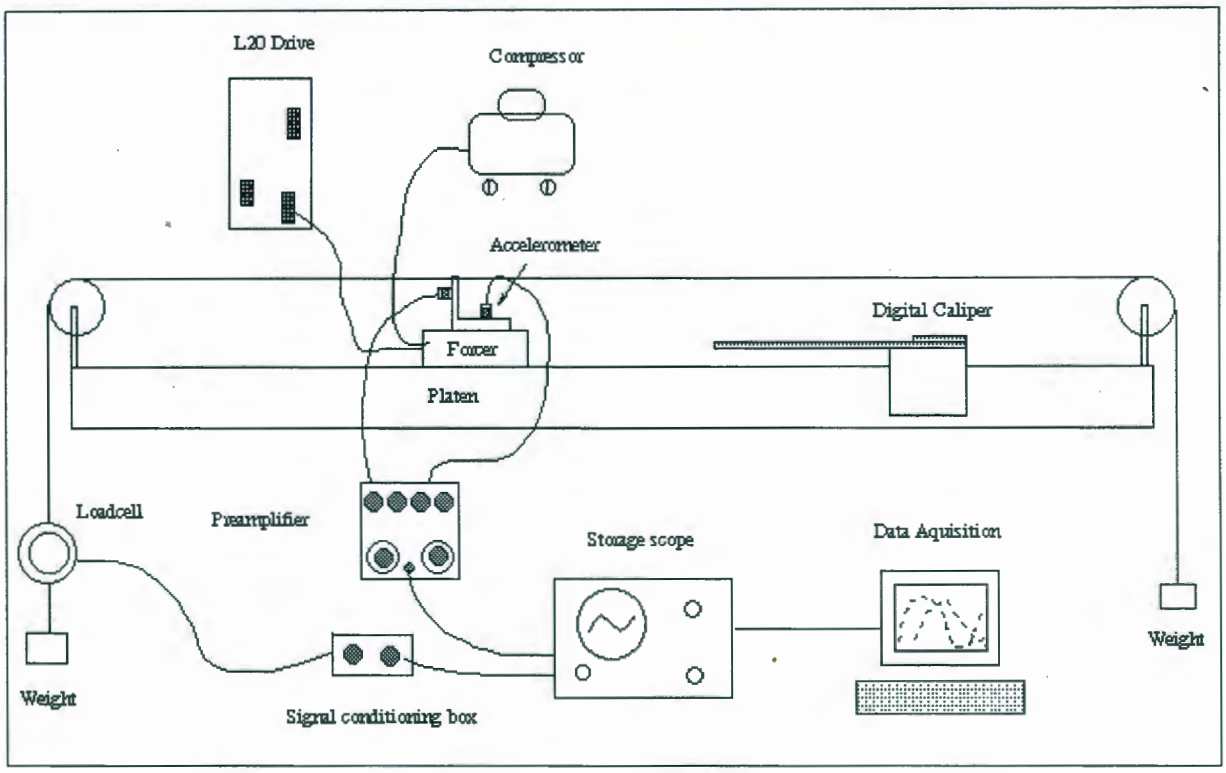

(b)

Figure 2.1: Test bench: (a) general view (b) arrangement of the HLSM and instruments.

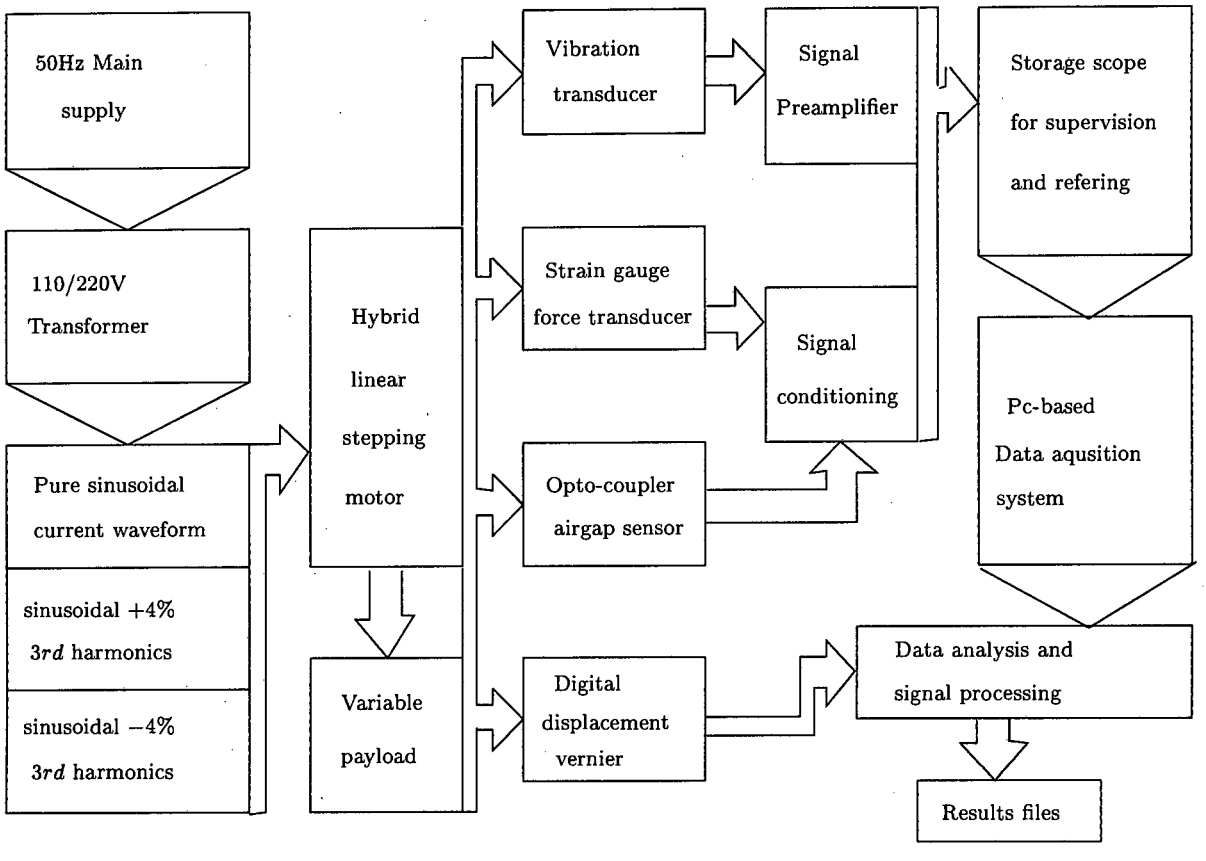

Figure 2.2: The flow chart of the testing scheme of the HLSM

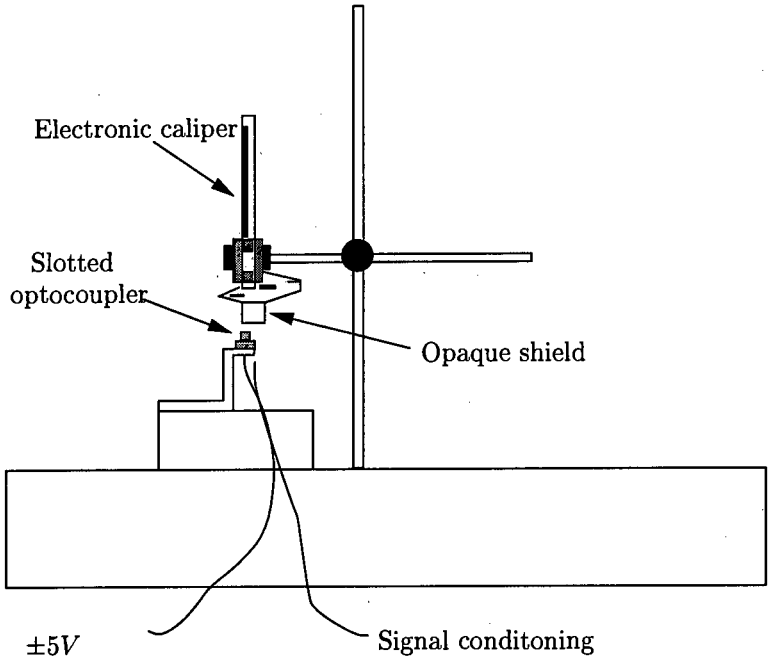

Figure 2.3: The experimental set-up for determining the small airgap of HLSM.

a more stable airgap length (see Table 2.3).

The measured typical airgap length ranges from 0.01 to 0.02 mm. However, the average airgap is less than 0.015 mm. An average airgap length of 0.0127 mm has been used in both the FEM and the classical approach simulations.

Table 2.3: Specific air pressure values for different excitation profiles

Quantity	Value
Current free state	274 kpa
One phase excited state	294 kpa
Two phases excited state	353 kpa

2.3 Steady state characteristics

2.3.1 Force-displacement characteristics and holding force

The tested HLSM is kept stationary by supplying rated current to only one phase. The forcer position at no load is defined as the equilibrium position. The relationship between force and

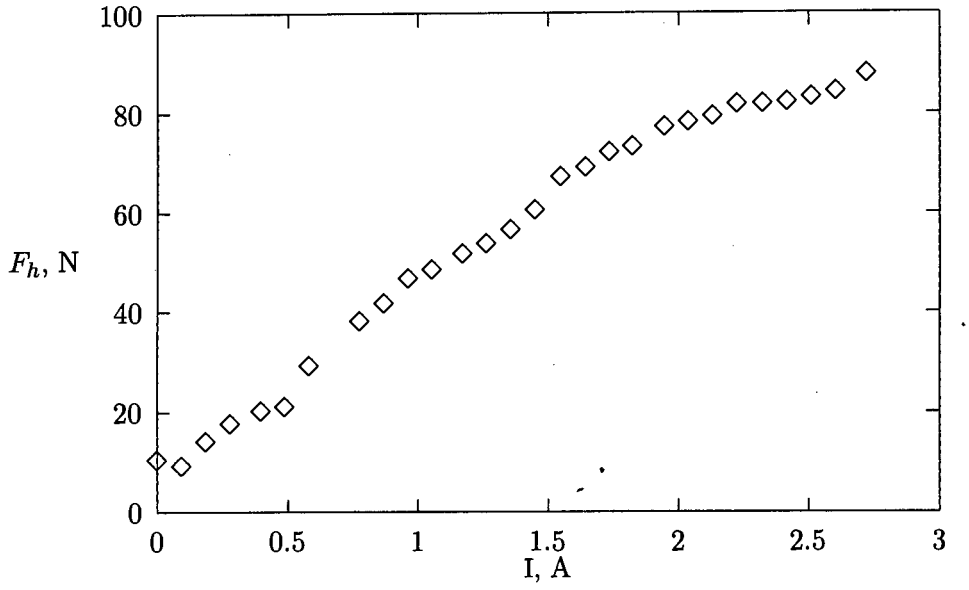

Figure 2.5: Measured force – current characteristics

2.3.3 Instantaneous force characteristics

The instantaneous force characteristics have been taken by testing the output force characteristics when the motor was driven in two-phase on excitation scheme and reached its steady state. Since the available strain gauge is not sensitive enough to pick up the force ripple, the B&K type 8301 piezoelectric accelerometers have been attached to the HLSM and positioned centrally between the front and back faces.

The acceleration signals have been amplified by the B&K type 2650 charge amplifier and then logged onto the storage scope and data acquisition system. The ripple forces were simply calculated by the following formula.

$$f_r = m\frac{V_s}{V_u}K \tag{2.1}$$

where V_s is the signal amplitude (V) of the indicating instrument (storage scope), V_u is the $Volt/unit$ output value selected on 2650 type preamplifier, K is a constant dependent on the setting of transducer sensitivity on the 2650 amplifier, and m is the mass of the forcer.

For comparison, different excitation current profiles at different resolution settings have been used in the measurements. The results obtained from the experimental tests are given in Figs 2.6 to 2.12. It can be seen that the stepping resolution of the HLSM has no significant

influence on the amplitude of ripple forces for both the tangential and normal forces. When the HLSM was driven by pure sinusoidal current, the maximum tangential force ripple was near 65 N as shown in Fig 2.6. The superimposition of the $3rd$ harmonic did help improving the force characteristics since the maximum tangential ripple force was reduced up to 16% accordingly (Figs 2.7 and 2.8). Both harmonic-added and harmonic-subtracted schemes work equally well in reducing the amplitude of force ripple.

However in the case of normal force characteristics, it shows even better improvement by subtracting the $3rd$ harmonic component from the current profile than that can be achieved by adding harmonic to the profile. The measured normal forces showed up to 35% improvement than before (see Fig 2.11).

Fig. 2.12 gives the relations of the amplitude of tangential force ripple for different peak phase current levels. It has been found that the amplitude of tangential force ripple increases when higher phase current is applied. However the relation between them is not so linear as compared with some previously published results [29]. This can be explained because the higher order harmonic components cannot be neglected when the magnetic circuit becomes highly saturated.

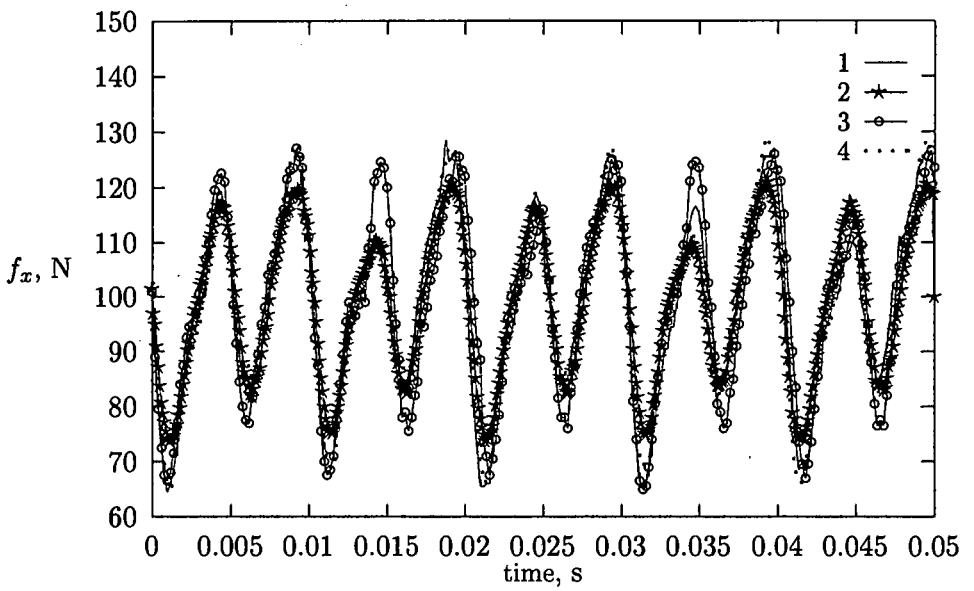

Figure 2.6: Measured instantaneous output force when phase A is fed with a pure cosine wave and phase B is fed with a sine wave: 1 – $50\mu step/fullstep$ resolution, 2 – $90\mu step/fullstep$, 3 – $100\mu step/fullstep$, 4 – $125\mu step/fullstep$.

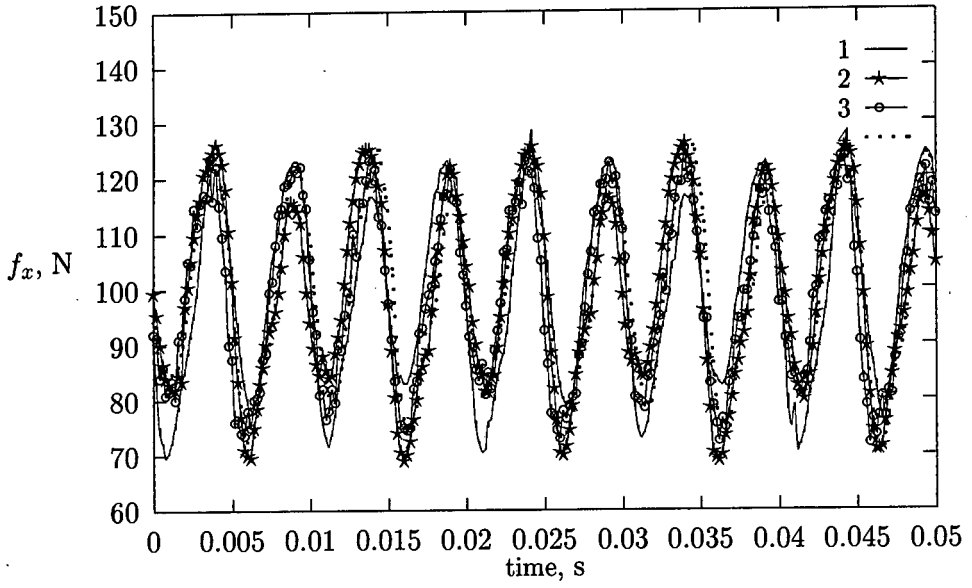

Figure 2.7: Measured instantaneous output force when phases A and B are fed with quasi-sinusoidal wave (4% of the 3rd harmonic added): 1 – $50\mu step/fullstep$, 2 – $90\mu step/fullstep$, 3 – $100\mu step/fullstep$, 4 – $125\mu step/fullstep$.

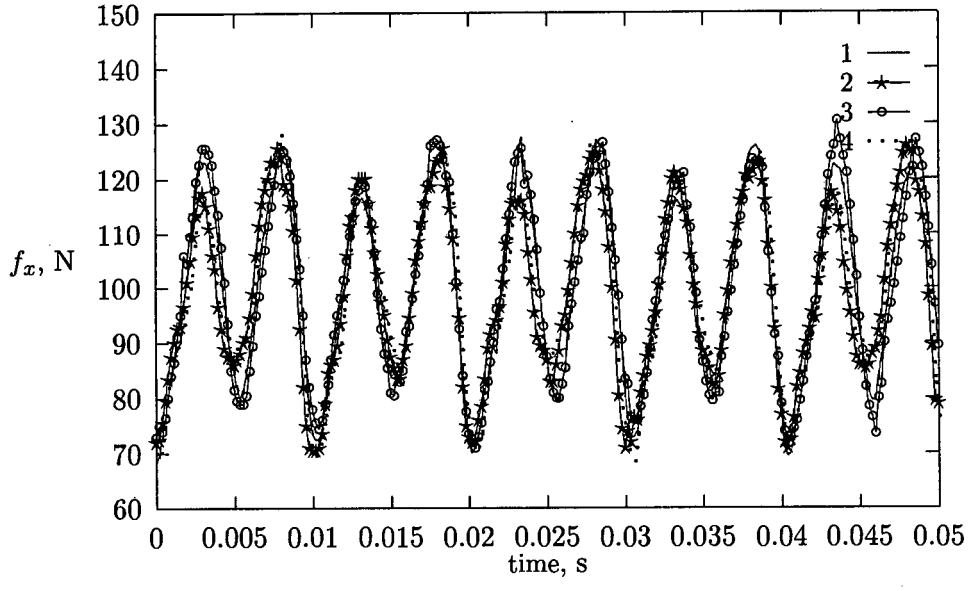

Figure 2.8: Measured instantaneous output force when phases A and B are fed with quasi-sinusoidal (4% of the 3rd harmonics subtracted): 1 – $50\mu step/fullstep$, 2 – $90\mu step/fullstep$, 3 – $100\mu step/fullstep$, 4 – $125\mu step/fullstep$.

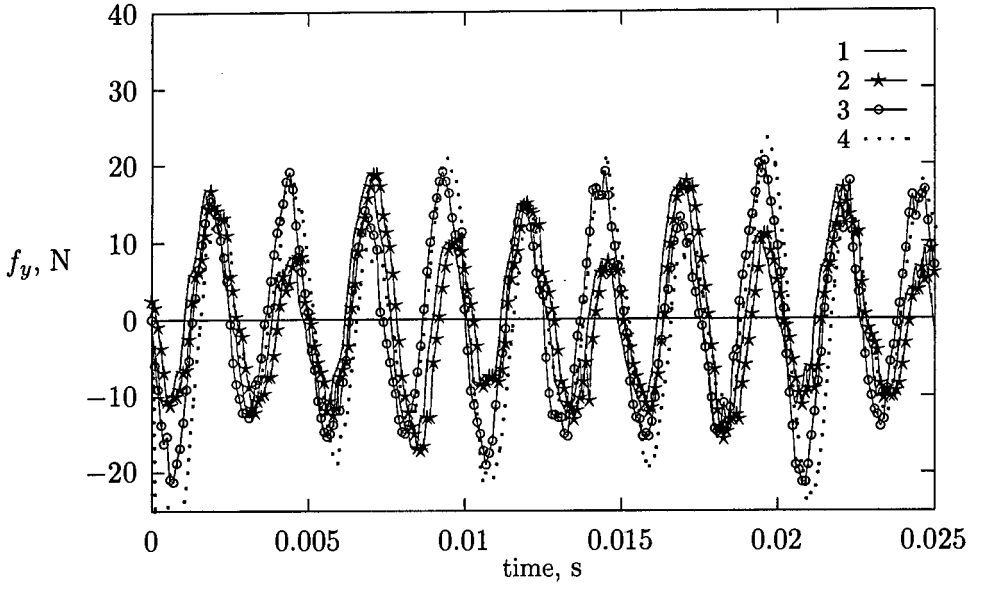

Figure 2.9: Measured normal force pulsation when phase A is fed with a pure cosine wave and phase B is fed with a sine wave: 1 – $50\mu step/fullstep$, 2 – $90\mu step/fullstep$, 3 – $100\mu step/fullstep$, 4 – $125\mu step/fullstep$.

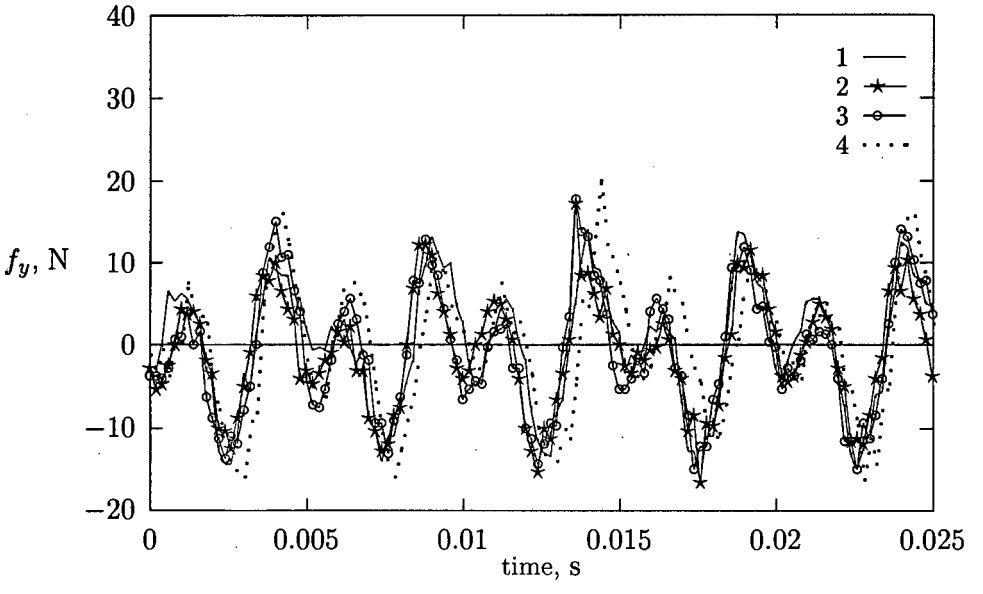

Figure 2.10: Measured normal force pulsation when phases A and B are fed with a quasi-sinusoidal wave (4% of the 3rd harmonic added): 1 – $50\mu step/fullstep$, 2 – $90\mu step/fullstep$, 3 – $100\mu step/fullstep$, 4 – $125\mu step/fullstep$.

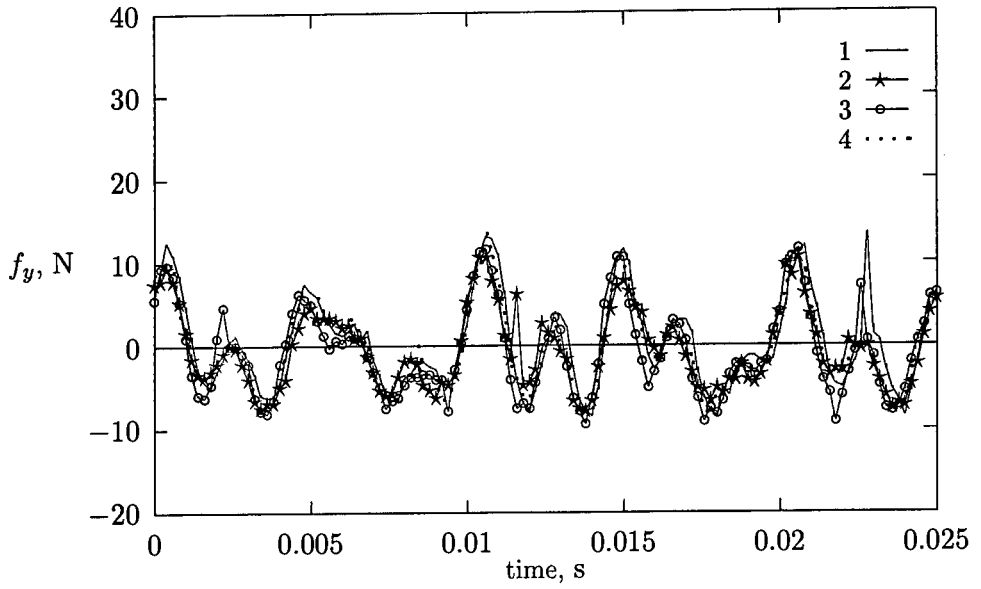

Figure 2.11: Measured normal force pulsation when phases A and B are fed with quasi-sinusoidal wave (4% of the 3rd harmonics subtracted): 1 – $50\mu step/fullstep$, 2 – $90\mu step/fullstep$, 3 – $100\mu step/fullstep$, 4 – $125\mu step/fullstep$.

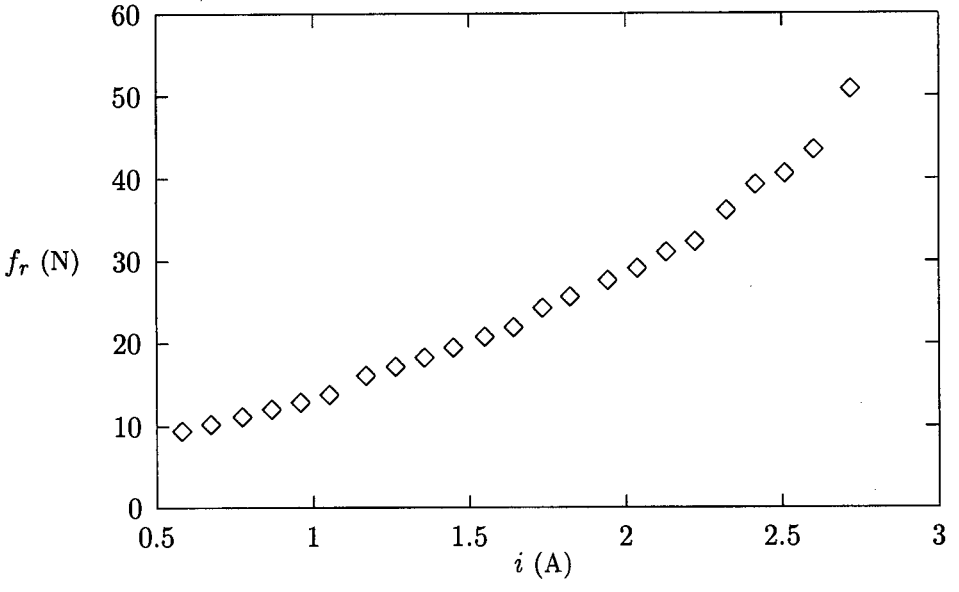

Figure 2.12: Tangential force ripple amplitude as a function of peak current.

2.4 Transient characteristics

2.4.1 Start-up tests

The transient performance measurements of the HLSM have been focused on the start-up and the braking states. The start-up tests were done by supplying power to the HLSM and at the same time recording the motor acceleration which are varying as a function of time. The time span from the moment that the power is being supplied to the HLSM to the moment that the HLSM is reaching steady state is called start-up settling time.

Whenever there is a force exerted on the accelerometer, the piezoelectric material in it will produce an instant charge which can be transformed into a measurable voltage signal through the preamplifier. The calibrated signal can then be logged onto a storage scope and then data acquisition system. By recording each instant value continuously, the acceleration versus time characteristic during the period of start-up can be obtained. It has been noticed that the motor becomes stalled quite often when the top load exceeds 2kg because the working pressure of the compressor is about 600kpa. Thus the tests have only been performed under no-load, 1kg top load and 2kg top load conditions as shown in Figs 2.13 to 2.15.

It takes about 1.7s for the HLSM to reach its steady state from being powered up while no load is applied. As expected somewhat longer time will be needed when certain amount load is attached to the HLSM. The time span of start-up with 1kg and 2kg top load attached are 1.8s and 2s, respectively.

2.4.2 Braking tests

The braking characteristic is also a key parameter of the HLSM performance. It has been done by recording the motion status from the instant at which the power to the motor was cut off until the motor came to a standstill. Figs 2.16 to 2.18 show the deceleration-time characteristics of the HLSM at no-load, 1kg top load and 2kg top load conditions.

It can be seen that the braking time inversely proportional to the attached weight. In no-load situation it takes about 0.11s for the HLSM to come to a standstill from the moment of switching off the power (see Fig 2.16), while the settling time span 0.08s and 0.04s with 1kg top load and 2kg top load put on, respectively. Both the start-up and braking tests have been conducted with the default resolution setting, i.e. $100\mu steps/fullstep$. The relations between settling time and resolutions is illustrated in Figs 2.19 and 2.20. Apparently the higher the resolution is set the less the settling time is needed.

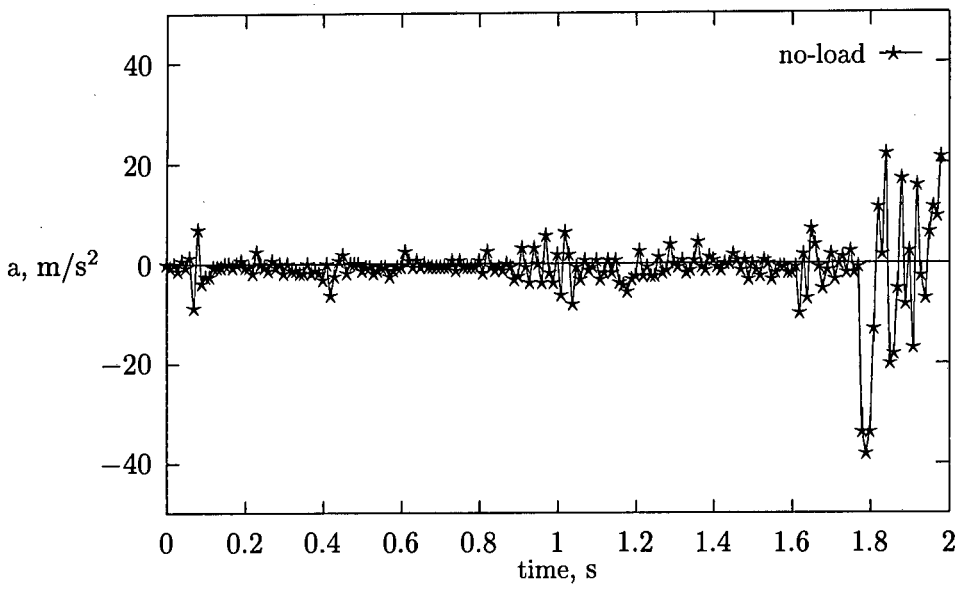

Figure 2.13: Acceleration-time characteristic of HLSM at no-load state.

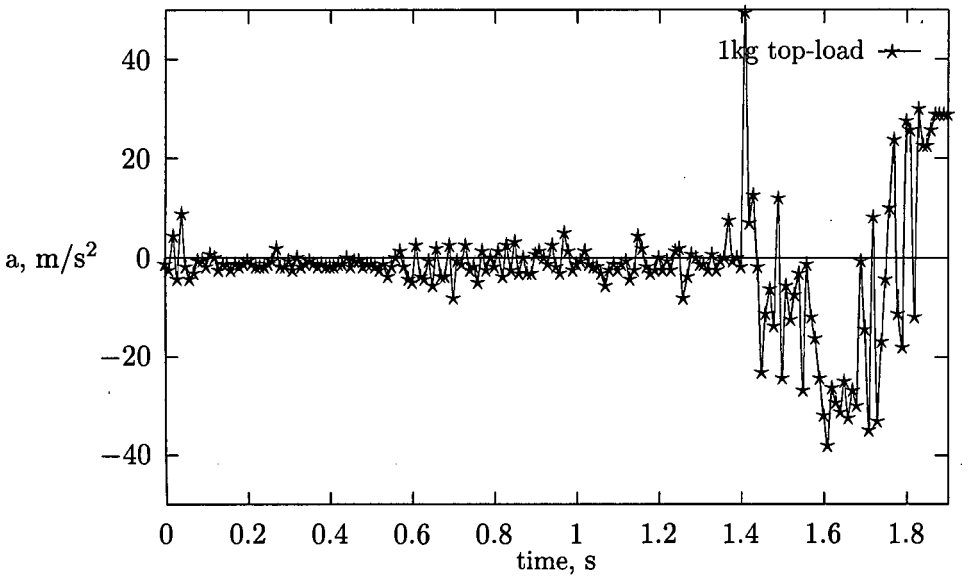

Figure 2.14: Acceleration-time characteristic of HLSM with 1kg top load applied.

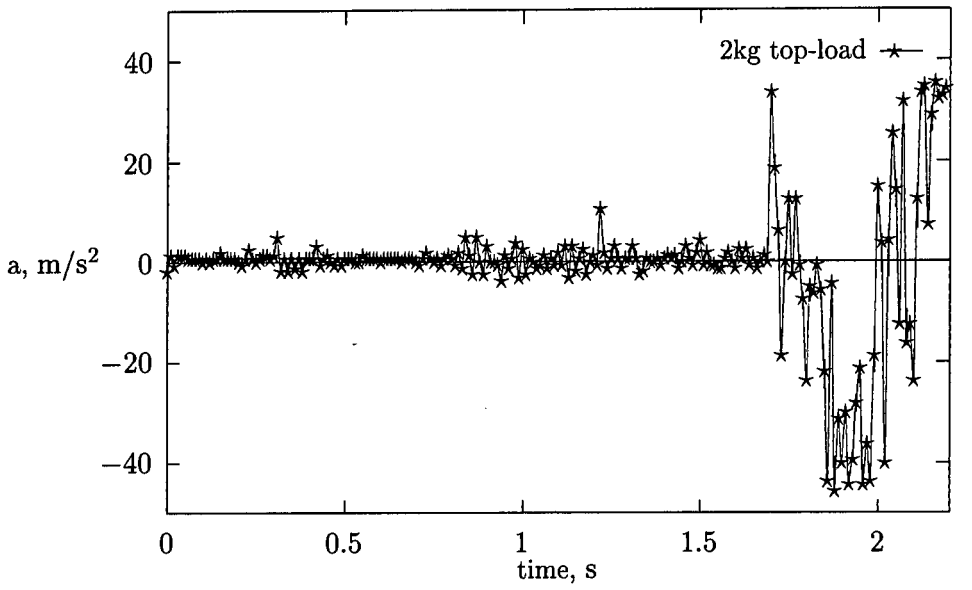

Figure 2.15: Acceleration-time characteristic of HLSM with 2kg top load applied.

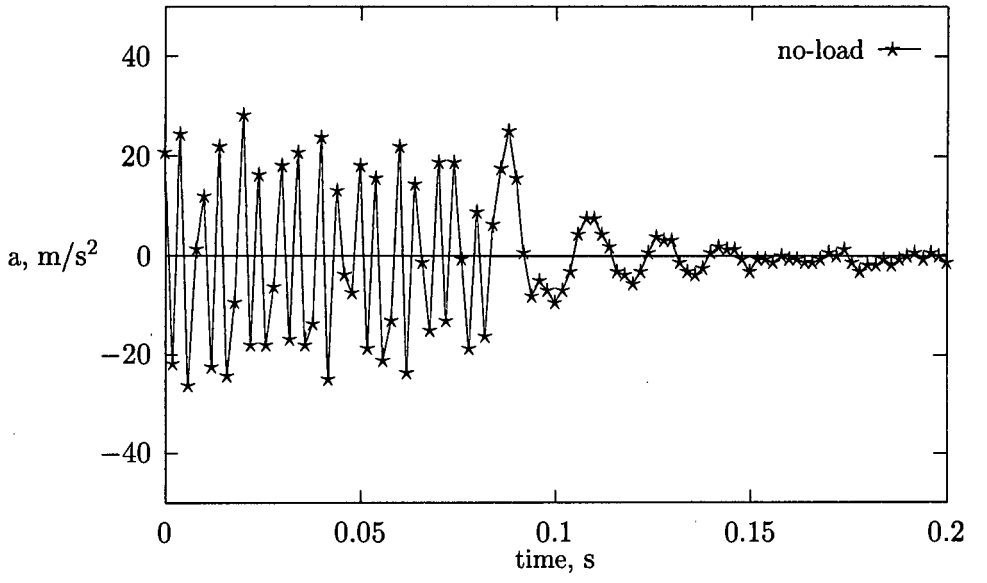

Figure 2.16: Deceleration-time characteristic of HLSM at no-load state.

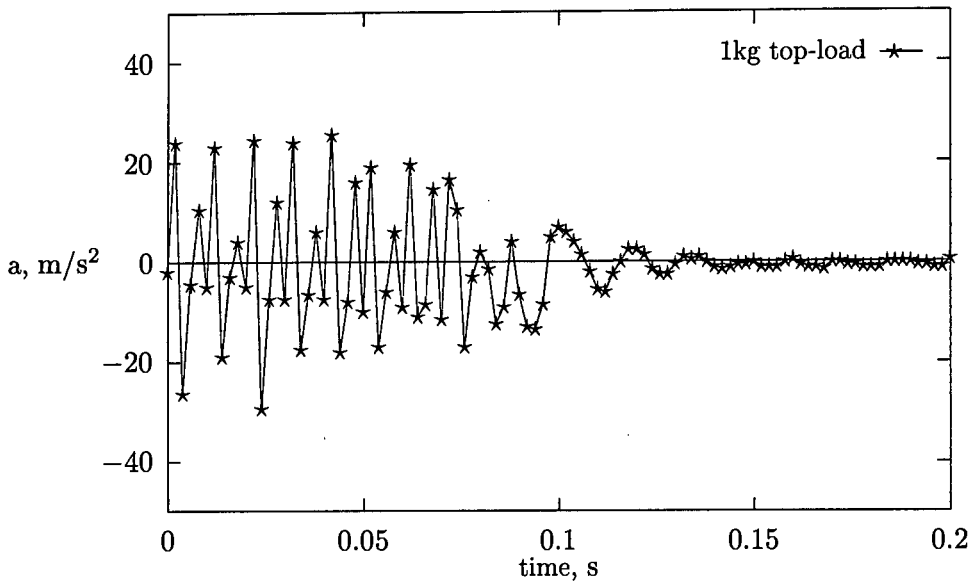

Figure 2.17: Deceleration-time characteristic of HLSM with 1kg top load applied.

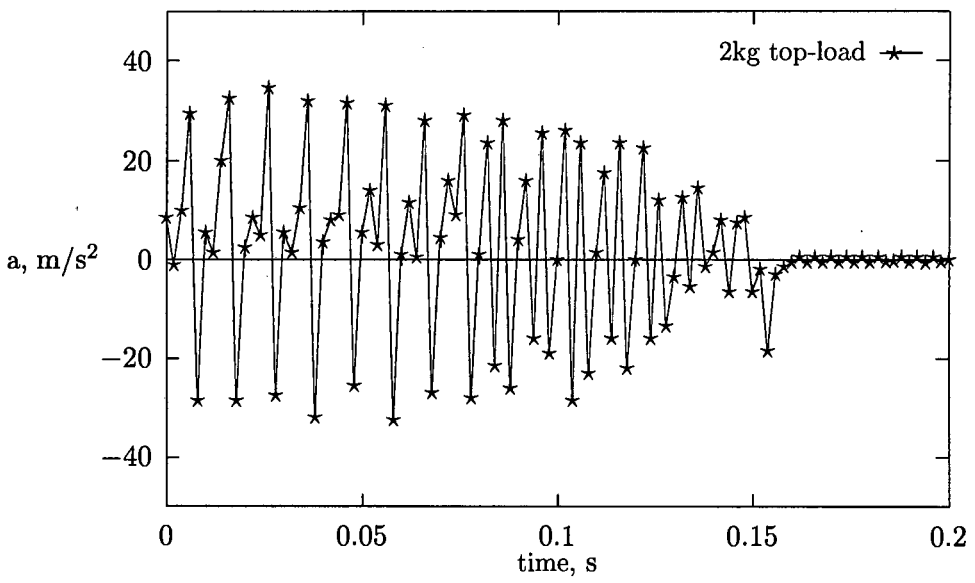

Figure 2.18: Deceleration-time characteristic of HLSM with 2kg top load applied.

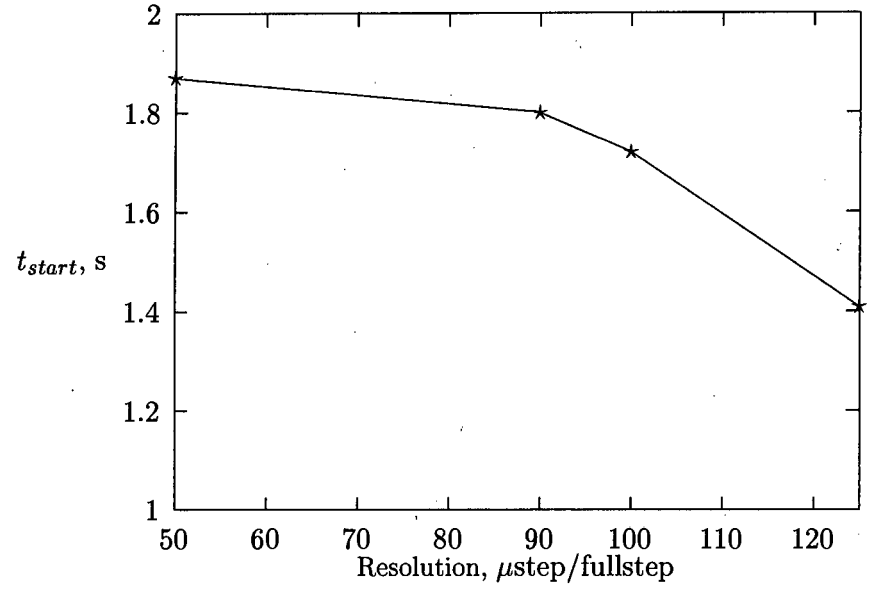

Figure 2.19: Relations between start-up time and step resolution settings

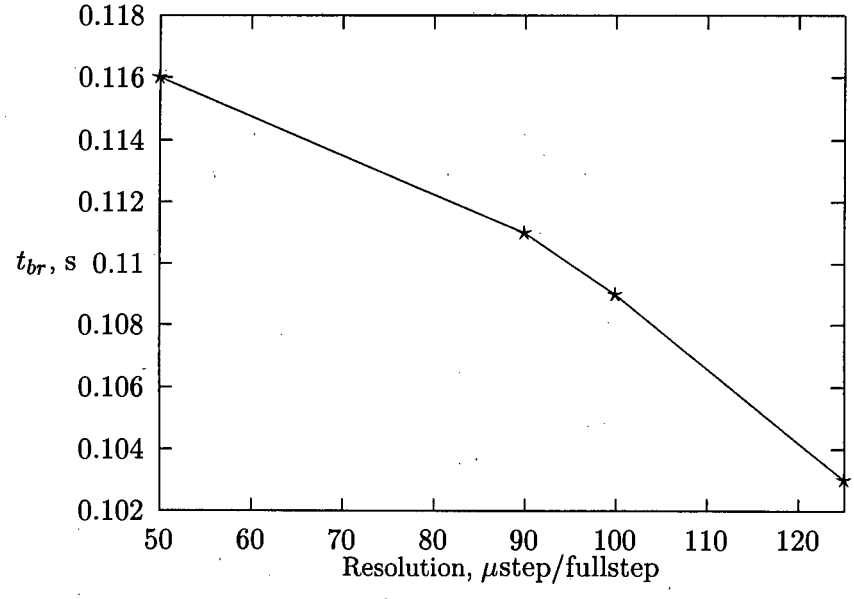

Figure 2.20: Relations between braking time and step resolution settings

Chapter 3

Finite Element Method Approach

The modern and efficient way for calculating and analysing the steady-state characteristics of electrical machines is the finite element method (FEM). In this chapter, fundamental equations of electromagnetic fields are discussed and the finite element models are described.

3.1 Fundamental equations of electromagnetic fields

3.1.1 Maxwell equations

The most fundamental description of electromagnetic field is in terms of the electric field intensity vector $\vec{E}$ and magnetic field intensity vector $\vec{H}$.

Both of them are related to the electric and magnetic flux density vectors $\vec{D}$ and $\vec{B}$, as well as to the field sources: electric charge density ρ and the electric current density vector $\vec{J}$. The relationships between these field vectors are expressed by Maxwell equations as follows:

$$\nabla \times \vec{H} = J + \frac{\partial \vec{D}}{\partial t} \tag{3.1}$$

$$\nabla \times \vec{E} = -\frac{\partial \vec{B}}{\partial t} \tag{3.2}$$

$$\nabla \cdot \vec{D} = 0 \tag{3.3}$$

$$\nabla \cdot \vec{B} = 0 \tag{3.4}$$

It has been assumed in the above equations that the velocity $\vec{v} = 0$ and the volume of charge

density $\rho_v = 0$. Additional equations describing the materials are:

$$\vec{D} = \epsilon \vec{E} \tag{3.5}$$

$$\vec{B} = \mu \vec{H} \tag{3.6}$$

$$\vec{J} = \sigma \vec{E} \tag{3.7}$$

where σ - electric conductivity, μ - magnetic permeability and ϵ - electric permittivity.

3.1.2 Magnetic and electrical potentials

Since the divergence of the *curl* of any twice differentiable vector vanishes, the vector $\vec{A}$ which is commonly known as the magnetic vector potential can be defined as

$$\vec{B} = \nabla \times \vec{A} \tag{3.8}$$

which satisfies the identity

$$\nabla \cdot \vec{B} = \nabla \cdot \nabla \times \vec{A} = 0 \tag{3.9}$$

According to Helmholtz theorem, a vector is uniquely defined if, and only if, both its *curl* and divergence are known, as well as its value at some one space point is given. If the *curl* expression of $\vec{A}$ is substituted into the first Maxwell equation (3.1), then

$$\nabla \times (\nabla \times \vec{A}) = \mu(\vec{J} + \frac{\partial \vec{D}}{\partial t}) \tag{3.10}$$

Using the identity

$$\nabla \times (\nabla \times \vec{A}) = \nabla(\nabla \cdot \vec{A}) - \nabla^2 \vec{A} \tag{3.11}$$

The eqn (3.10) becomes

$$\nabla(\nabla \cdot \vec{A}) - \nabla^2 \vec{A} = \mu \vec{J} + \mu\epsilon \frac{\partial \vec{E}}{\partial t} \tag{3.12}$$

Since $\nabla \cdot \vec{A} = 0$ and at power frequencies 50 or 60Hz $\sigma \vec{E} \gg j\omega\epsilon\vec{E}$, the magnetic vector potential can be expressed with the aid of Poisson's equation, i.e.:

$$\nabla^2 \vec{A} = -\mu \vec{J} \tag{3.13}$$

3.1.3 Boundary constraints

Apart from the current density $\vec{J}$, a set of boundary conditions is needed to solve Possion's equation. Three types of boundary constraints are commonly used. They are

1. Dirichlet boundary condition

$$\vec{A} = f(b) \tag{3.14}$$

2. Neumann boundary condition

$$\frac{\partial \vec{A}}{\partial n} = 0 \tag{3.15}$$

3. Binary constraints (symmetric structure)

$$\vec{A}_1 + k\vec{A}_2 = m \tag{3.16}$$

where $f(b)$ is a specified function along the boundary, m and k are problem dependent parameters. There are two types of symmetry which allow the three dimensional ($3D$) objects to be modelled in two dimensions ($2D$). They are the translational and rotational symmetry, respectively [8].

Obviously, the tested linear stepping motor falls into the first category. Inevitably the $2D$ simplification neglects fringing and leakage flux in the axial or z direction, which are so-called edge effects.

3.2 Finite element method

3.2.1 Energy functional and variational principle

One of the primary steps in the finite element analysis is to formulate the energy functional for the studied field problem. The nonlinear partial differential equation for a magnetostatic problem in a $2D$ Cartesian system is given by

$$\frac{\partial}{\partial x}(\nu\frac{\partial \vec{A}}{\partial x}) + \frac{\partial}{\partial y}(\nu\frac{\partial \vec{A}}{\partial y}) = -\vec{J} \tag{3.17}$$

where reluctivity ν is the reciprocal of the magnetic permeability μ.

Expressed in variational terms as an energy functional, the electromagnetic field described in the above equation can be written as

$$\mathcal{F} = \int\int_{area} (\int_0^B \vec{H} d\vec{B} - \int_0^A \vec{J} d\vec{A}) dxdy \tag{3.18}$$

here $\vec{H} = \nu \vec{B}$ and $\vec{A}$ is the magnetic vector potential.

In isotropic materials the energy functional can be simplified according to different material properties. For hard magnetic materials, there are

$$\vec{B} = \mu_0 \vec{H} + \vec{M} \approx \mu_m \vec{H} + \vec{M}_r \tag{3.19}$$

$$\mathcal{F} = \int\int_{area} (\frac{\vec{B}^2}{2\mu_m} - \frac{\vec{M}_r \vec{B}}{\mu_m} - \vec{J}\vec{A}) dxdy \tag{3.20}$$

where $\vec{M}$ is the magnetisation vector, $\vec{M}_r$ is the remanent magnetisation vector and μ_m is the magnetic permeability of the material.

For soft magnetic materials, the second term in the above equation vanishes as a result of the remanent magnetisation $\vec{M}_r = 0$. The energy functional $\mathcal{F}$ becomes

$$\mathcal{F} = \int\int_{area} (\frac{\vec{B}^2}{2\mu} - \vec{J}\vec{A}) dxdy \tag{3.21}$$

Since there exists no excitation current in the airgap region ($\vec{J} = 0$), so

$$\mathcal{F} = \int\int_{area} \frac{\vec{B}^2}{2\mu} dxdy \tag{3.22}$$

3.2.2 Discretization of the field region

In the FE program used in the simulation, the first-order triangular finite elements of unrestricted geometry and material inhomogeneities have been used for discretizing the field region. All the elements are connected at nodal points.

In two dimensions the magnetic vector potential $\vec{A}$ has some useful properties. For Cartesian problems in the $x - y$ plane, the current and therefore magnetic vector potential is in the z direction. So the $\vec{A}$ can be expressed in the scalar form of A.

The magnetic vector potential solution in a certain element A_e is defined in terms of shape functions of the triangular geometry and its nodal values of potential as follows

$$A_e = \sum_{i=1}^{n} N_i A_i \tag{3.23}$$

where N_i is the shape function of the ith node, A_i is the magnetic vector potential at the corresponding node.

The energy functional is re-written for each element within a model as follows.

$$\mathcal{F} = \sum_{i=1}^{n} \int\int_{area} [\frac{1}{2\mu}|\nabla \times (\sum_{i=1}^{n} N_i \vec{A}_i)|^2 - \frac{1}{\mu}\vec{M}_r \nabla \times (\sum_{i=1}^{n} N_i \vec{A}_i) - j\sum_{i=1}^{n} N_i \vec{A}_i] dxdy \tag{3.24}$$

The minimisation of the functional is performed with respect to each of the nodal potentials as follows

$$\frac{\partial \mathcal{F}}{\partial \vec{A}_i} = \sum_{e=1}^{n} \frac{\partial \mathcal{F}_e}{\partial \vec{A}_i} = 0 \tag{3.25}$$

When the minimisation described by above equation is carried out for all the triangles of the field region, the following matrix equation can be obtained, in which the unknown vector potential $[A]$ is determined, i.e.

$$[S] \cdot [A] = [J] \tag{3.26}$$

where $[S]$ is nonlinear, symmetric, sparse and band structured matrix and $[J]$ is the excitation matrix.

The nonlinear equation is first quasi-linearised by Newton-Raphson algorithm and then the obtained matrix equation is solved directly. In each Newton-Raphson iteration, the reluctivity is updated with respect to the $B-H$ curve of the material. The kth iteration of the magnetic vector potential yields the $(k+1)$st iteration according to

$$A^{k+1} = A^k - [\xi]^{-1}[SA^k - J] \tag{3.27}$$

where $[\xi]$ is the Jacobian matrix of the partial derivatives of the iteration function $[SA^k - J]$.

3.3 Force calculations

In this section, both the *Maxwell stress tensor* and the co-energy method are considered. A comparison has been made between these two approaches and computational advantages have been emphasised.

3.3.1 Maxwell stress tensor

The *Maxwell stress tensor* gives the stress in terms of the magnetic field strength. If B_n and B_t are the normal and tangential component of the magnetic flux density, respectively, then the resulting normal and tangential stresses are

$$\sigma_n = \frac{B_n^2 - B_t^2}{2\mu_0} \tag{3.28}$$

$$\sigma_t = \frac{B_n B_t}{\mu_0} \tag{3.29}$$

These results offer a simple and effective way of calculating forces provided that two conditions have been met:

- The stresses given above are not the true local force densities. This only means that the total force obtained by integrating the stresses over a closed surface can be determined mathematically in this way.
- The closed surface should be entirely in the air instead of passing any material.

More specifically, in $2D$ Cartesian problem, the integration over a closed surface is reduced to an integral around a closed path. The normal and tangential force components are therefore given by

$$F_y = \frac{w}{2\mu_0} \int_l (B_n^2 - B_t^2) dl \tag{3.30}$$

$$F_x = \frac{w}{\mu_0} \int_l B_n B_t dl \tag{3.31}$$

where w is the axial length of the forcer (perpendicular to the $x-y$ plane) and l is the integration path.

Theoretically, the results from this method should be accurate and consistent. However, the discretization of the field region, especially for the electromagnetic devices with small airgap, can be of great influence.

If the airgap is large, then the method can yield accurate results. Since the modelled HLSM has a very small airgap (0.0127mm), only a single layer of mesh has been used in the airgap region. To obtain accurate results, the following steps are helpful:

- the airgap mesh should be *hand-made* by controlling the number of subdivisions along the airgap boundary and of regular shape;

- for the best accuracy contours should pass close to the centroids of elements.

3.3.2 Classical virtual work method

The classical virtual work (CVW) method has been considered as a more accurate and consistent way for force or torque calculation since this approach determines the force acting on an object as a derivative of the system's total stored co-energy with respect to a positional displacement of the object within the system.

Therefore, it reduces greatly the adverse effects of local errors due to coarseness of the mesh discretization on the final result [32].

Two FE solutions are needed, one for each position of the object along the moving direction. Then, the calculated co-energy values from the two solutions are used to form a finite difference approximation to the derivative, i.e.:

$$F_d = \frac{\partial W}{\partial d} \approx \frac{W_1 - W_0}{d_1 - d_0} \tag{3.32}$$

where W is co-energy and ∂d or $d_1 - d_0$ is the displacement along the moving direction.

Since the extremization solution procedure used in the FEM optimise the calculation of stored co-energy, and judicious meshing of the simulated model leads to cancellation in the integrated discretization errors [28], the CVW should be a perfect method in principle.

However, the derivative approximation can introduce round-off error in computing the difference of nearly identical co-energies and the sampling of co-energies could be insufficient for modelling the non-linearity of the changing characteristics.

3.3.3 Coulomb's approach to virtual work method

The classical virtual work method needs two solutions which takes a considerable computational time. Coulomb's approach to virtual work uses differentiation of magnetic energy and needs only one solution [7]. Although Coulomb's approach stems from the magnetic energy expression, it is also possible to derive the same results by using the magnetic co-energy formulation. For magnetostatic problems governed by the magnetic vector potential $\vec{A}$, the magnetic energy W' is

$$W' = \int_V \int_0^H \vec{H} d\vec{B} dV \tag{3.33}$$

It has been assumed that the magnetic flux in all the paths is constant during a displacement within the system. The global tangential force F_x exerted on the movable but rigid part of the system is then

$$F_x = -\frac{\partial W'}{\partial x} = \frac{\partial}{\partial x} \int_V \int_0^H \vec{H} d\vec{B} dV \tag{3.34}$$

After the discretization of the field domain, the above equation is written for each element separately. Then the isoparametric elements are used for obtaining a general derivation of the tangential force.

$$F_x = -\sum_e [\int_{V_e} \frac{\partial}{\partial x} (\int_0^B \vec{H} d\vec{B}) dV + \int_{V_e} \int_0^B \vec{H} d\vec{B} \frac{\partial}{\partial x} (dV)] \tag{3.35}$$

in which

$$\frac{\partial}{\partial x}(dV) = |G|^{-1} \frac{\partial |G|}{\partial x} dV \tag{3.36}$$

and $|G|$ is the determinant of the Jacobian matrix G.

$$G = \begin{bmatrix} \frac{\partial x}{\partial u} & \frac{\partial y}{\partial u} \\ \\ \frac{\partial x}{\partial v} & \frac{\partial y}{\partial v} \end{bmatrix} = \sum_i \begin{bmatrix} \frac{\partial N_i}{\partial u} \\ \\ \frac{\partial N_i}{\partial v} \end{bmatrix} \begin{bmatrix} x_i & y_i \end{bmatrix} \tag{3.37}$$

After some mathematical transformations, the eqn (3.38) can be written as

$$F_x = -\sum_{\square e} (\frac{\vec{B}^T}{\mu_0} \frac{\partial \vec{B}}{\partial x} + \frac{\vec{B}^T \vec{B}}{2\mu_0} |G|^{-1} \frac{\partial |G|}{\partial x}) \cdot V_e \tag{3.38}$$

where V_e is the volume of the element.

For linear triangular element, the above equation can be simplified further (see Appendix A). The final equation has the following form:

$$F_x = \sum_e \sum_i \frac{1}{4\mu_0} [(y_2 - y_3)\Delta_1^2 + 2(x_3 - x_2)\Delta_1\Delta_2 - (y_2 - y_3)\Delta_2^2] \tag{3.39}$$

where Δ_1 and Δ_2 are defined as

$$\Delta_1 = \frac{A_1(x_3 - x_2) + A_2(x_1 - x_3) + A_3(x_2 - x_1)}{|G|} \tag{3.40}$$

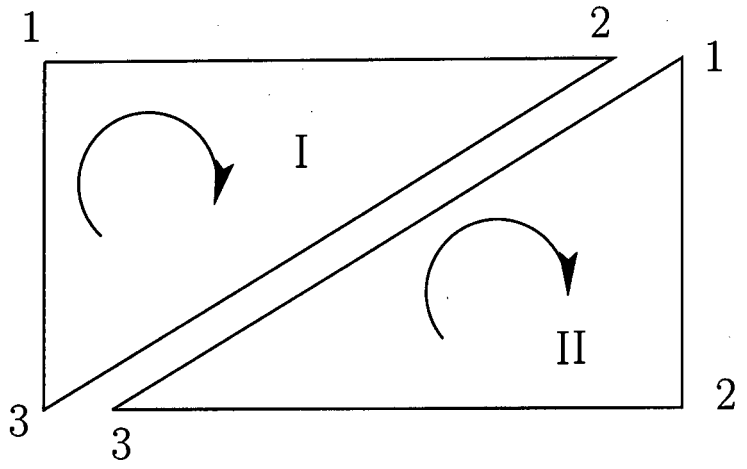

Figure 3.1: Triangle element in the airgap

$$\Delta_2 = \frac{A_1(y_3 - y_2) + A_2(y_1 - y_3) + A_3(y_2 - y_1)}{|G|} \tag{3.41}$$

Similarly, the dual formulation for calculating the normal force in the y-direction is obtained as

$$F_y = \sum_e \sum_i \frac{1}{4\mu_0}[(x_3 - x_2)\Delta_1^2 + 2(y_3 - y_2)\Delta_1\Delta_2 - (x_3 - x_2)\Delta_2^2] \tag{3.42}$$

In the FE simulation of the studied HLSM, only one layer meshes have been generated in the airgap region. All the elements are of the same shape (see Fig 3.1). To facilitate the FEM implementation, all the upper nodes are assumed to be movable while the lower nodes are fixed. For each element the movable node is always defined as node 1, the other nodes are labelled according to a certain sequence, say, *clockwise*. The element containing two movable nodes should be considered separately observing the same labelling rules.

From eqns (3.43) to (3.44), it can be seen that Δ_1 and Δ_2 represent B_x and B_y, respectively. For some commercial FE softwares, both the magnetic vector potential and the magnetic flux density can be calculated by using built-in functions. This offers two selections from the implementation point of view. The only difference is on how to extract the magnetic flux density values.

Fig. 3.2 shows part of the 2D FE meshes in the airgap region of a HLSM. The elements in the airgap region are of such shape as shown in Fig 3.1. Eqns (3.38) and (3.39) can be re-written for each elements as follows.

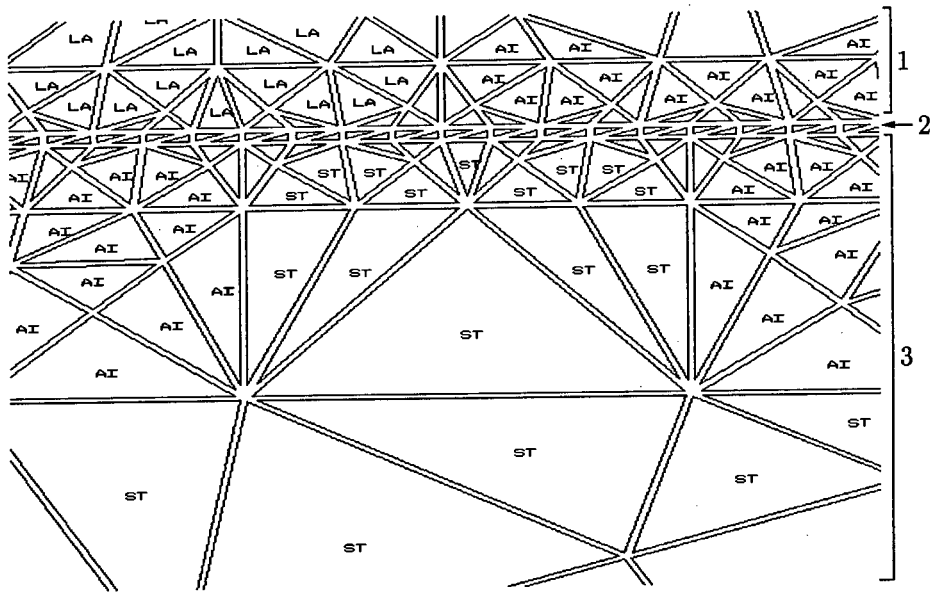

Figure 3.2: Part of FE meshes in a HLSM with the airgap layer. 1 – forcer, 2 – airgap, 3 – platen.

$$F_x = \sum_e \frac{-l_{dvi}}{2\mu_0} \Delta_1 \cdot \Delta_2 \tag{3.43}$$

$$F_y = \sum_e \frac{-l_{dvi}}{2\mu_0} (\Delta_2^2 - \Delta_1^2) \tag{3.44}$$

where l_{dvi} is the length of an element along the airgap (in the x direction).

Obviously, the above eqns (3.43) and (3.44) have the same forms as *Maxwell stress tensor*. However, with some special features such as a best selected integral path (a path connecting all the middle points of airgap element edges) and magnetic flux densities taken from the central point of each airgap element.

Also it is interesting that only two factors have direct influence on the accuracy of force calculation. These are the number of divisions in the airgap and the accuracy of magnetic flux density values. The number of division in the airgap may be decided with consideration of the airgap width and the compromise in computation time within certain accuracy requirements. The accuracy of magnetic flux density is more dependent on the method used.

3.4 Finite element model

3.4.1 Geometric shape of the physical model

The forcer of the analysed HLSM consists of two stacks (see Fig 3.3). Each stack has two coils of different phases. Because of its asymmetric structure, both stacks have to be modelled. Since the magnetic circuit of one stack is independent of the other, it is acceptable to carry out the FE analysis on each stack separately.

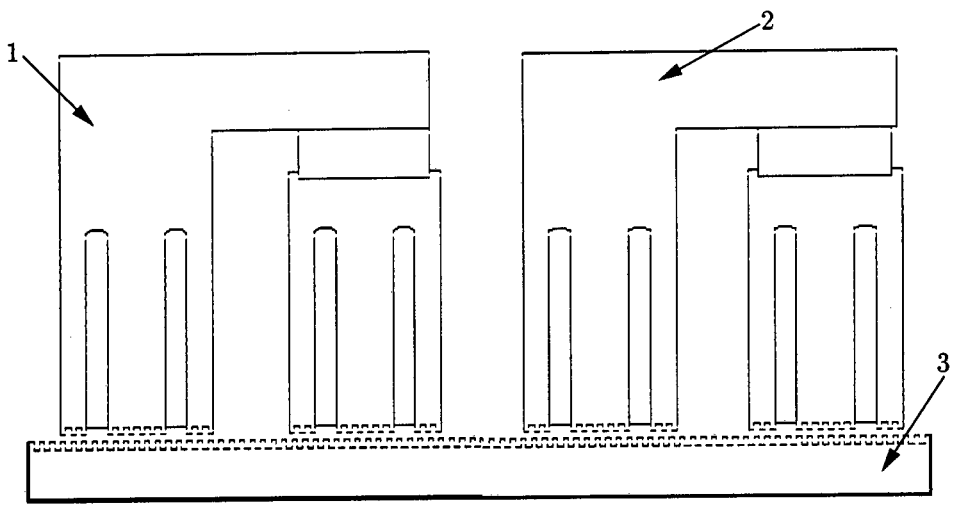

Figure 3.3: Cross section of the complete HLSM: 1–1st stack, 2–2nd stack, 3–platen.

Through the FE analysis, the following assumptions have been made:

- The edge effects are neglected and no field variations occurs in the axial direction (z-direction).
- The excitation currents are perpendicular to the $x - y$ plane.
- All the fringing and leakage fields in the z direction are neglected.
- All the materials for the forcer (laminated steel) and the platen (solid steel) are isotropic materials.

3.4.2 Finite element mesh and boundary constraints

The distribution of node density is very important considering of maximum 5,100 nodes and 10,240 elements available for a single FE model in the FE package used for the analysis. The

accuracy in the airgap area The accuracy of the field calculation in the airgap area should be rather high.

Since the modelled HLSM has a tiny airgap of 0.0127 mm, the meshes in the airgap layer become small and dense so that it may maintain a low aspects ratio (i.e. the ratio between any two sides of a triangle should be close to unity) for each element. This means that a high density of nodes along airgap boundaries is needed.

Figs 3.4 and 3.5 demonstrate the complete FE mesh layout of each stack of the HLSM, which contains 7,535 and 7,580 elements, respectively.

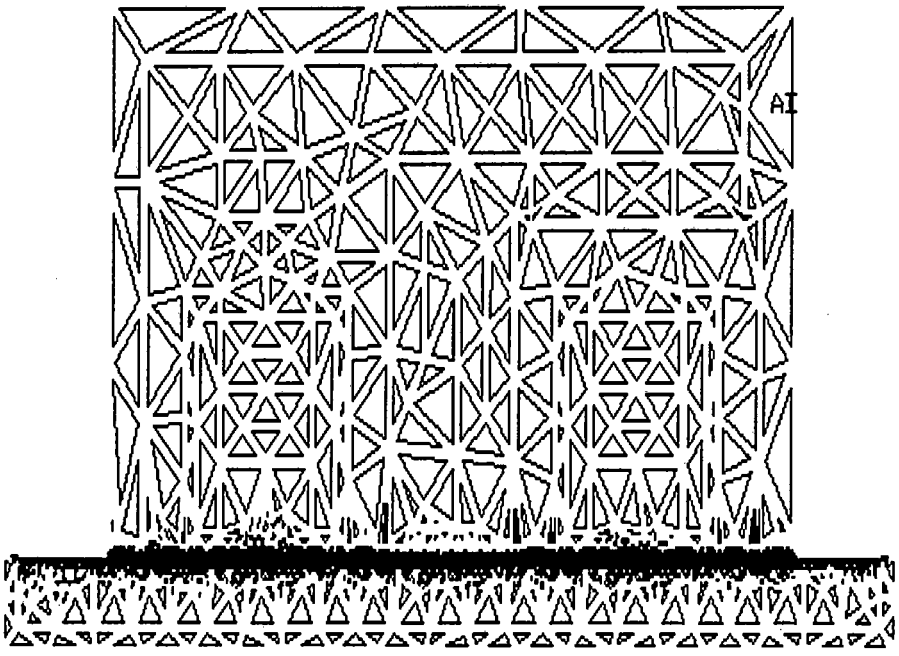

Figure 3.4: Complete FE mesh layout of the 1st stack of the HLSM (7535 elements)

A Dirichlet boundary condition has been set up on the defined outer boundary of the HLSM magnetic circuit with the vector potential of value $\vec{A} = 0$.

The defined boundary is placed certain distance (e.g. several tooth pitch) away from the conduct surfaces since directly imposing the natural boundary condition can cause a big influence on the calculation results.

In the investigated 2-stack HLSM, each stack is considered as a single finite element model. Because of very dense and small elements being used in the airgap region and its surrounding area, the control of transition of the element size from tiny one to fairly big one is important

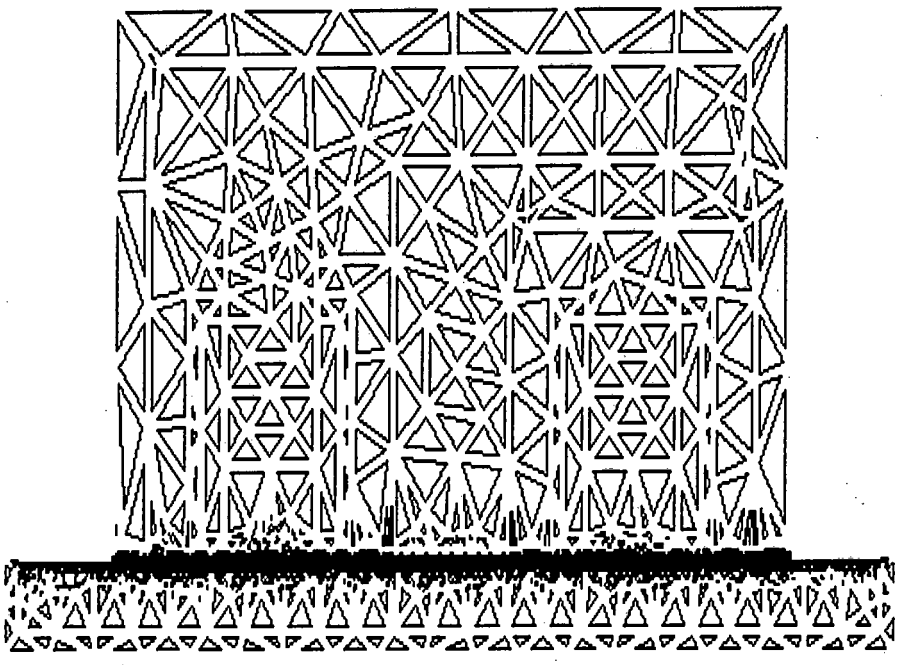

Figure 3.5: Complete FE mesh layout of the 2nd stack of the HLSM (7580 elements)

to keep a reasonable aspect ratio (near unity).

One effective measure of controlling the mesh generation process while using automatic mesh generator is to draw several accelerating lines near the region where very small elements cannot be avoided. The intervals between lines are suggested to increase in such a way as to satisfy a rough rule of geometrical ratio while the number of nodes on corresponding lines decrease in a similar way.

Since each FE model of the HLSM contains a high number of nodes, it takes quite a long time (e.g. 15Minutes) to generate the meshes. For saving the computation time and keeping identical meshes in the area of interests, one efficient way is to perform meshing only on three basic models, i.e. the 1st stack of forcer, the 2nd stack of forcer and the platen. Then complete models corresponding to different tooth position can be assembled by using mesh-sliding technique. Table 3.1 contains some details of the final FE models of the HLSM.

3.4.3 FEM implementation of material properties

The non-linearity of the forcer yoke (laminated steel), platen (1024 steel) and rare-earth permanent magnets (NdFeB) have been included in the FE simulation by building $B-H$ curves

Table 3.1: Data of final FE model of HLSM

Stack code	Node num.	Elem. num.	Airgap elem. num.	Max. elem. aspect ratio	Order of elem.	Elem. num. per tooth pitch
1st	3819	7535	1448	5	2nd	20
2nd	3847	7580	1428	5	2nd	20

according to manufacturer's data specification sheets. The rare-earth permanent magnets have a linear demagnetization curve (see Appendix B).

3.4.4 Phase current profile

Since the *MagNet 5.1* FEM package is unable to do transient analysis of electrical machines, only the static force and instantaneous force characteristics have been simulated.

The HLSM operates in a microstepping mode [38]. To include discrete current value at each mini-step into the FE simulation, a current versus displacement (which refers to relative displacement between forcer and platen) table was first set-up. Then, at each step, the FE package looks up the corresponding current value. Table 3.2 gives current profiles (for one phase) used in the simulation. The current waveform for the other phase should be of a cosine shape since there is 90^o phase shift.

Table 3.2: Current profiles for one phase used in FEM simulation

Excitation status	Current values/waveform
current-free state	0
static state	2.7A
steady-state (pure sine wave)	$2.7\sin\frac{2\pi}{\tau}x$
steady-state (pure sine +4% 3rd harmonic)	$2.7(\sin\frac{2\pi}{\tau}x + 0.04\sin\frac{6\pi}{\tau}x)$
steady-state (pure sine −4% 3rd harmonic)	$2.7(\sin\frac{2\pi}{\tau}x - 0.04\sin\frac{6\pi}{\tau}x)$

3.4.5 Comments on the optimisation of FE model

The optimisation of the finite element model is to investigate all the aspects of the model for the best results. The density of the finite element meshes, the aspect ratio of the elements (especially in the airgap region) and the number of FE models needed to be built are crucial.

There is one potential area of difficulty in the modelling of the HLSM. This arises as a result of the small airgap. Normally the airgap requires three or four layers of elements which

means setting fine subdivisions circumferentially in order to achieve high accuracy in the field calculation. On the other hand, putting multi-layer elements in the small airgap results in high aspect ratios, unless the subdivisions along the airgap direction has been tremendously increased. This in turn leads to a higher number of small elements.

Since most of commercially available FEM packages have a limit on maximum number of nodes for a single model, the layers of elements are often reduced to one or two. This effect can be tackled by using higher order elements, leading to the longer computation time [8].

Also it is important to consider the edge effects. In the aligned position, the problem does not arise. However, in the unaligned position, the edge effects can cause difficulties. In this meaning, the three-dimensional modelling is preferred.

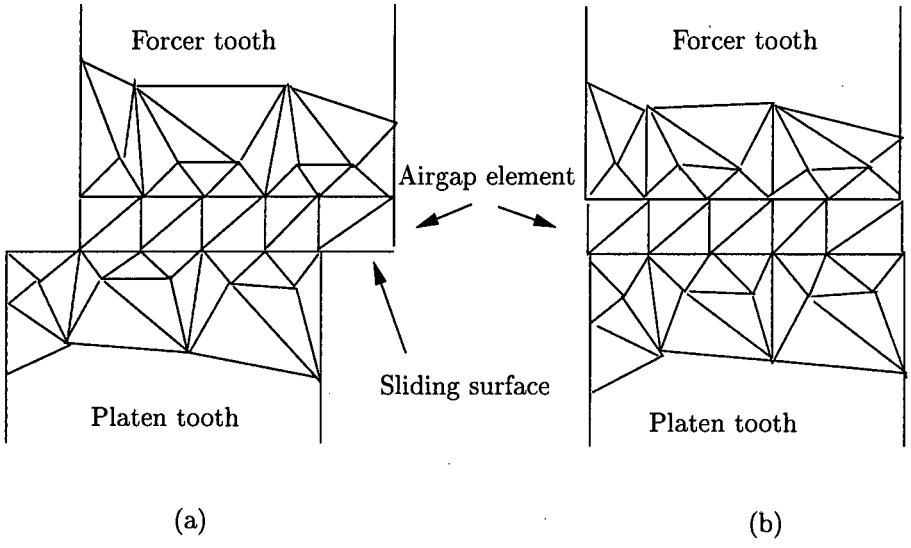

Figure 3.6: Sliding surface of a pair opposing tooth.(a) unalignment, (b) full alignment after one mini-step moving to left

For monitoring the changing forces over a tooth pitch (one cycle), the number of subdivisions set with equal intervals should be sufficient. Certainly, the choice of subdivisions is normally a process towards the accommodation of physical dimensions, element shape and accuracy requirements.

For the FEM force calculation on the basis of *Maxwell stress tensor*, the co-energy finite difference method or its alternative – Coulomb's virtual work method, the elements of the models corresponding to different motor positions are preferred to be identical. Thus it necessitates the utilisation of the node sliding method (see Fig 3.6) in assembling both movable and fixed parts of the HLSM to maintain the consistence of elements.

3.5 FEM simulation scheme and performance calculations

3.5.1 FE simulation scheme

Both the Coulomb's approach and commonly used methods such as *Maxwell stress tensor* are employed for calculations of forces through the simulation. To facilitate and speed-up the simulation a set of computer programmes were written in C++ code and interfaced with the FE package *MagNet 5.1a.*

Fig 3.7 demonstrates the overall logical flow chart of the simulation. The written computer programmes have been used for the following purposes:

- Set and transfer parameters to the FE package for each FE model
- Extract magnetic field values from FE solutions
- Perform post-FE calculations

3.5.2 FEM magnetic field calculations

Fig 3.8 shows the magnetic flux distribution in the tooth layer region, in which it can be observed that the magnetic saturation in the tooth tip area did happen as a result of the concentration of magnetic flux.

Usually, the four basic states (called full steps) of the forcer are used to describe static characteristics of a HLSM. Fig 3.9 illustrates the calculated typical field distributions in the airgap between forcer and platen due to their different relative positions.

It has been found that different teeth position will cause different permeance distribution between the forcer and platen and consequently different field distribution. When the relative teeth position of forcer and platen changes from perfect alignment (Fig 3.9c) to partial alignment (Fig 3.9b) and finally complete misalignment (Fig 3.9a), the corresponding reluctance between the two parts will vary from minimum to maximum.

For a practical HLSM, the three teeth alignment status exist at the same time in any motor step. Thus, there is a non-uniform flux distribution as far as the whole device is concerned.

The basic rules are that where teeth are perfectly aligned the average normal magnetic field intensity is high while the tangential magnetic field intensity is negligible and where teeth are completely misaligned both normal and tangential average magnetic field intensity are extremely small. However, the maximum average tangential magnetic field intensity may only be produced when teeth are partially aligned.

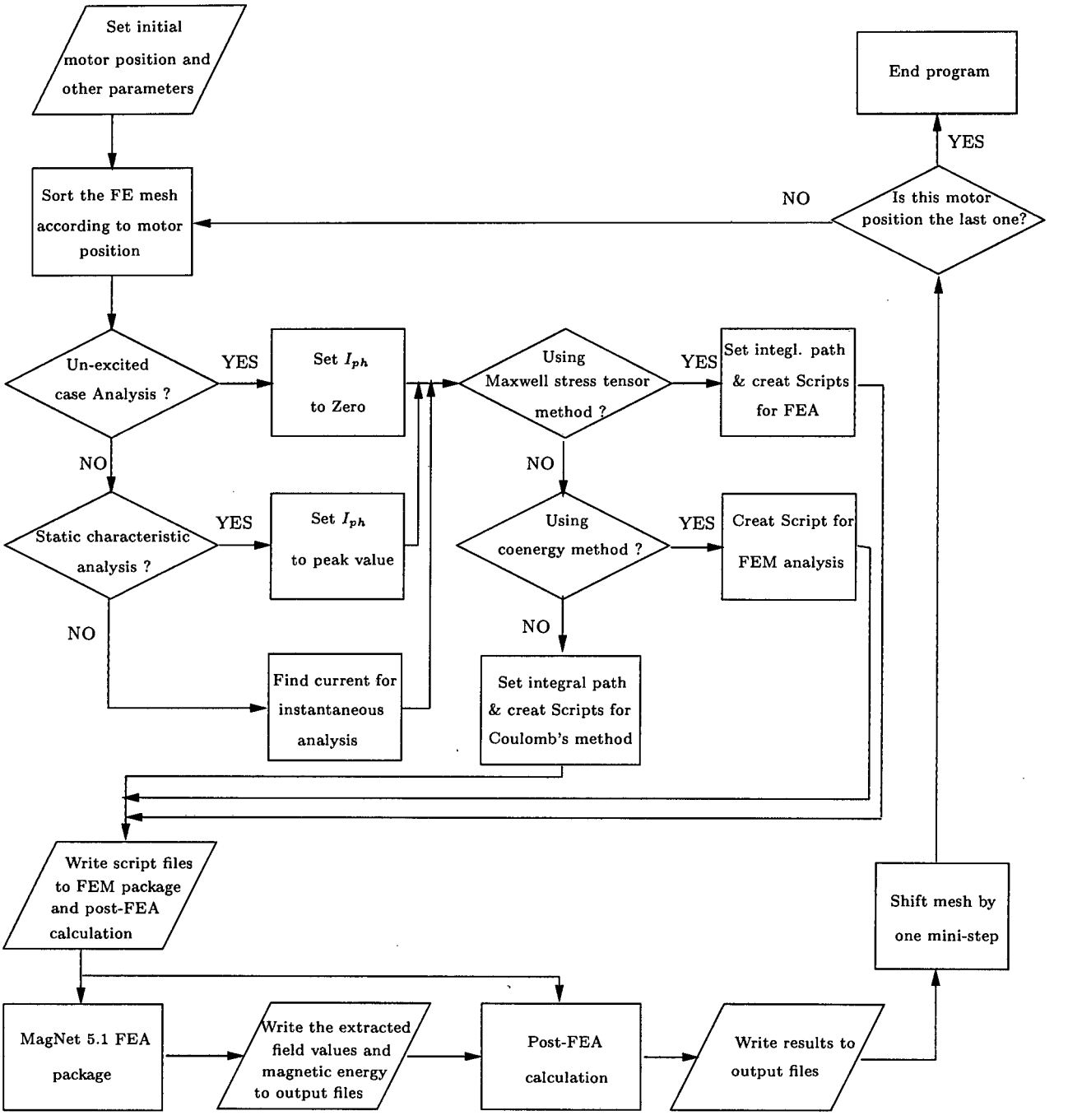

Figure 3.7: Flow chart showing the calculation of force characteristics.

It can be deduced from the *Maxwell stress tensor* that the maximum normal force between a pair of opposing teeth can be obtained only when the teeth are perfectly aligned and the maximum tangential force is produced only when the teeth are partially aligned.

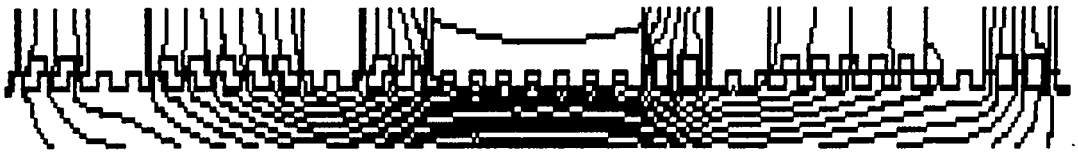

Figure 3.8: Magnetic flux distribution in the tooth layer region.

3.5.3 FEM performance calculations

Figs 3.10 to 3.17 show the calculated steady-state performance of the HLSM. It can be seen in Fig 3.10 that the calculated maximum holding force is about 75 N. The tooth positions corresponding to maximum force value are not on half step positions, which implies that the tangential force reaches maximum at a different point than a quarter of tooth pitch.

An investigation into an optimal design of the tooth layer [53] has revealed that the tooth layer dimensions may greatly change the static force waveform. In this specific case, the position for generating maximum holding force is when the tooth pair is 0.33mm overlapped.

The relations between peak current values and holding forces are illustrated in Fig 3.11. It can be seen that the holding force increases as the peak current value increases and the curve is quite linear before the peak current reaches 1.5 A, after which the rate of increase in holding force has been reduced.

The calculated instantaneous tangential force characteristics corresponding to different phase current profiles are demonstrated in Figs 3.12 and 3.13. When the HLSM is driven with pure sinusoidal waveform, the minimum available force is 73 N and the maximum force ripple is 50 N.

After 4% of the 3rd harmonic has been added to or subtracted from the previous phase current, the maximum output force becomes 8 N less than its pure sinusoidal excitation profile. however, the maximum force ripple has been reduced to 39 and 37 N, respectively. Fig 3.13 shows that an augment in the amplitude of the 3rd harmonic (injecting 10% into phase current) can further improve the force ripple to 30 N.

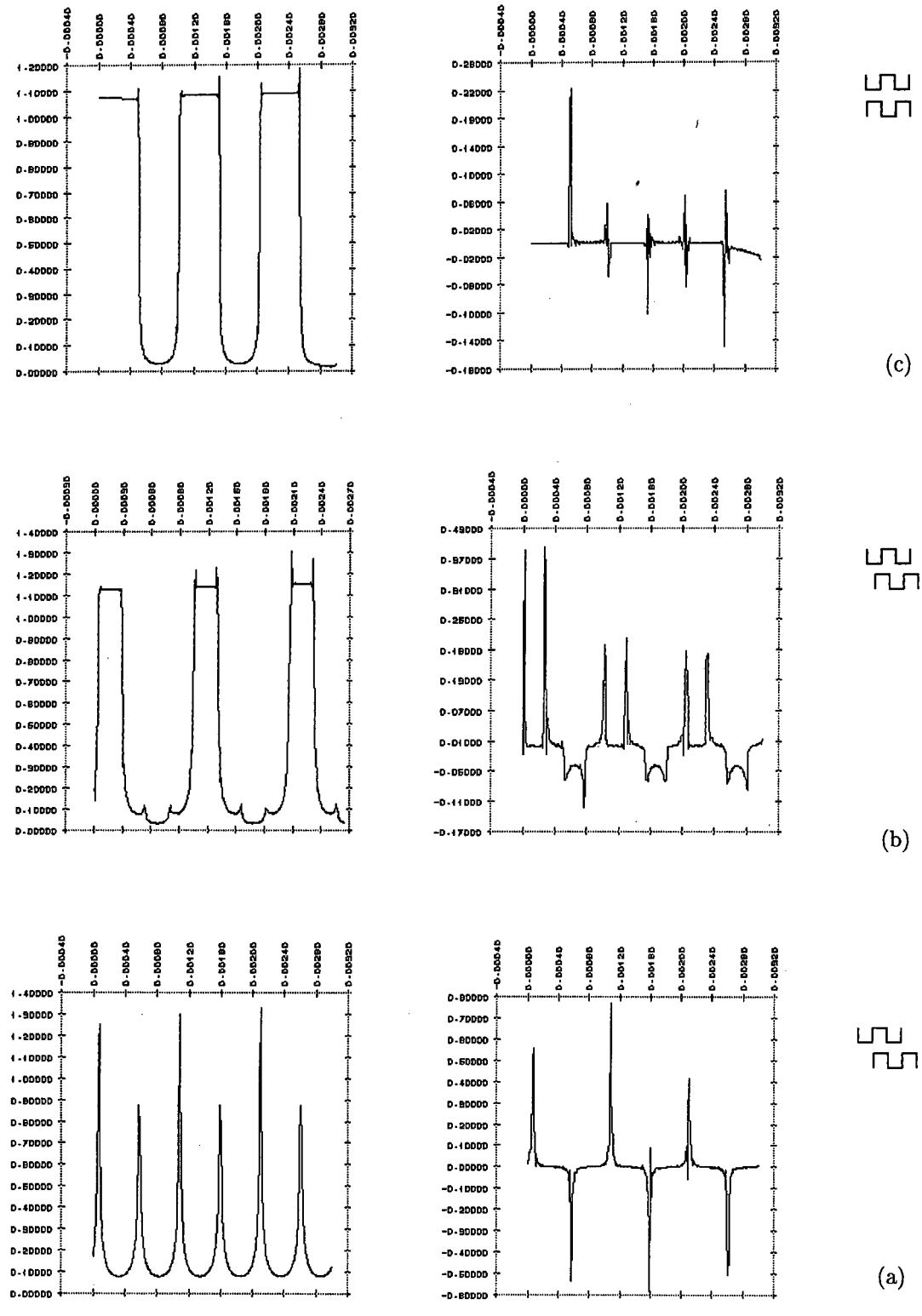

(c)

(b)

(a)

By vs. Contour length

Bx vs. Contour length

Figure 3.9: Magnetic field distribution of the HLSM for different tooth alignments: (a) complete misalignment, (b)partial alignment, (c)perfect alignment.

Owing to the existence of the PM, there is a strong normal force between the forcer and platen even when the HLSM is unenergised as shown in Fig 3.14.

The FEM simulated results show the normal force almost doubled when the HLSM is energised. The normal force is very sensitive to the small change in the airgap as illustrated in Fig 3.15. It can be seen in Fig 3.16 that the normal force increases as peak current value increases. The relationship between them is nearly linear.

Fig 3.17 gives the relationship between the amplitude of tangential force ripple f_r and peak current value, where f_r is obtained by picking up the difference between the maximum and minimum force in one period for each peak current. Obviously the amplitude of force ripple tends to increase as the peak current increases.

Theoretically, Coulomb's approach and *Maxwell stress tensor* should give the same results in force calculation. This has been confirmed by FE numeric calculations shown in Figs 3.10, 3.13 and 3.14.

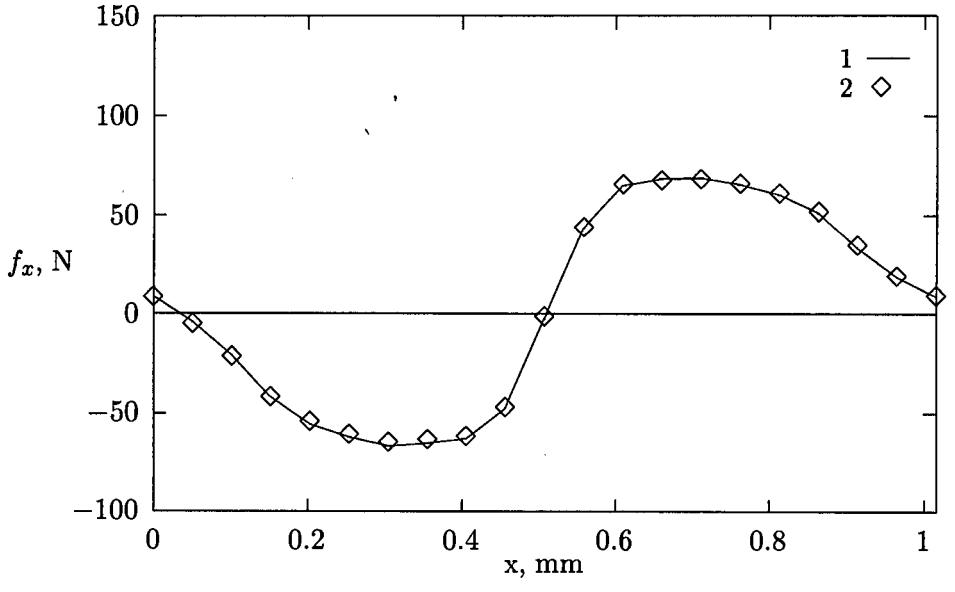

Figure 3.10: Steady state characteristics (only one phase is energised with phase current 2.7A): 1 – Coulomb's approach, 2 – Maxwell stress tensor.

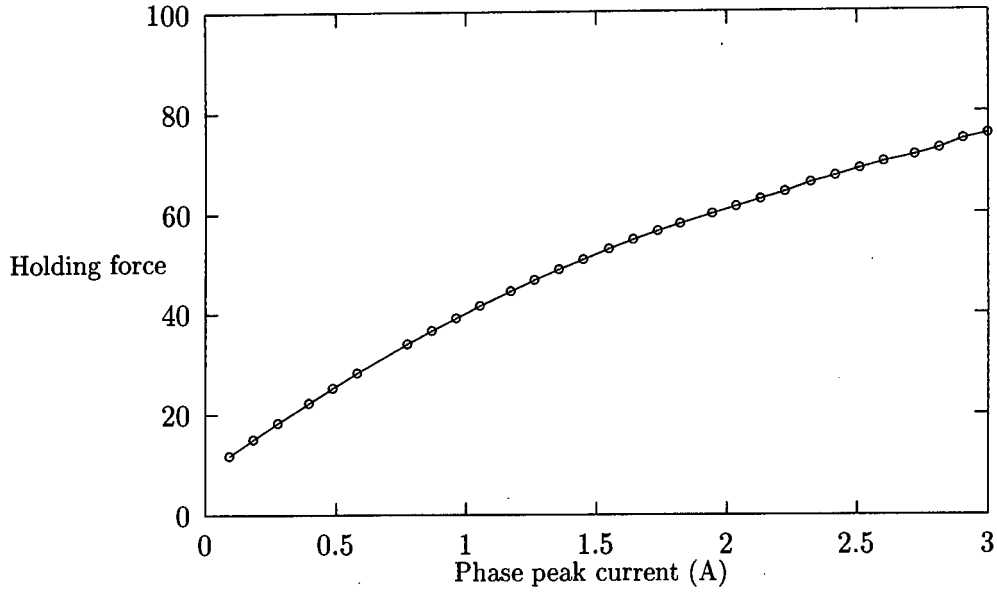

Figure 3.11: Holding force versus peak phase current.

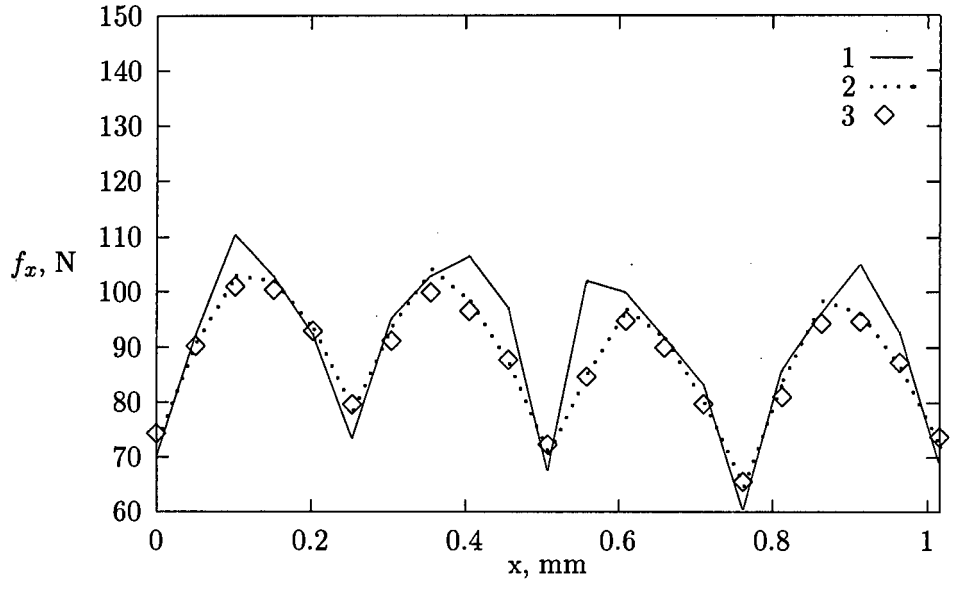

Figure 3.12: Instantaneous tangential force plotted against the displacement x (with a set of different phase current profiles): 1 – pure sinusoidal excitation, 2 – 4% of the 3rd harmonic added, 3 – 4% of the 3rd harmonic subtracted.

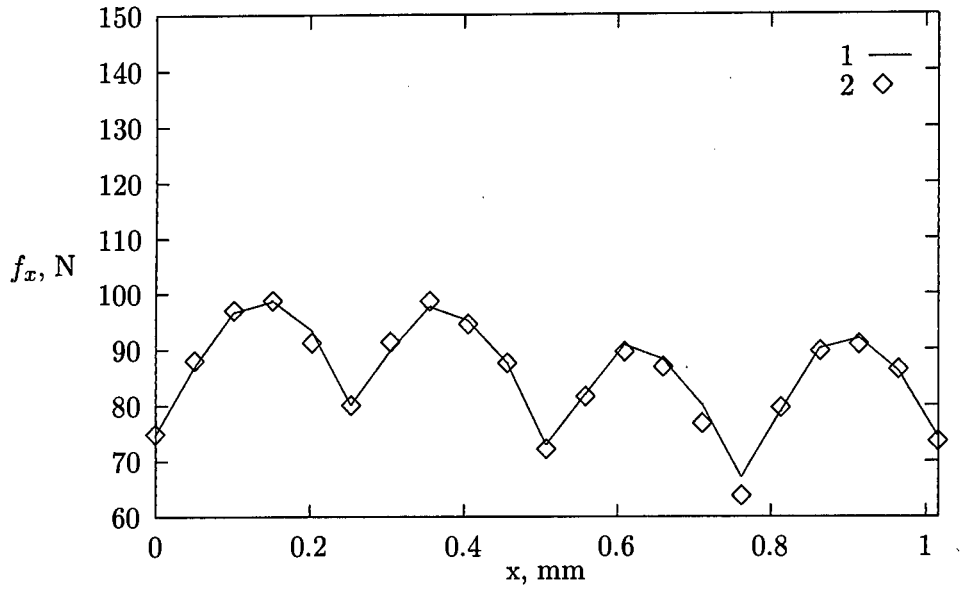

Figure 3.13: Instantaneous tangential force plotted against the displacement x (when a 10% of the 3rd harmonic has been injected into phase current): 1 – Coulomb's approach, 2 – Maxwell stress tensor.

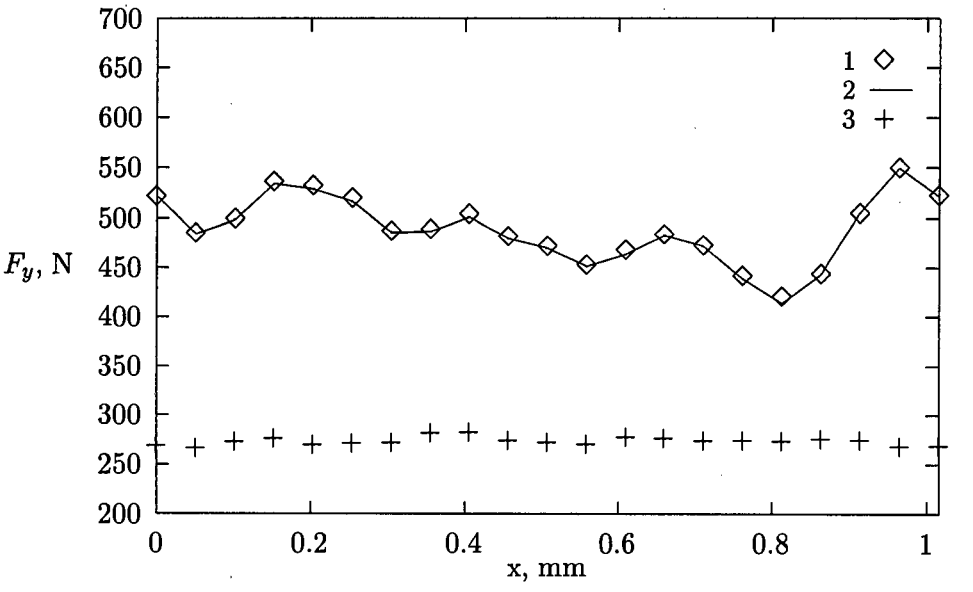

Figure 3.14: Normal force plotted against the displacement x: 1 – Coulomb's approach (two phases energised), 2 – Maxwell stress tensor (two phase energised), 3 – Coulomb's approach (HLSM unenergised).

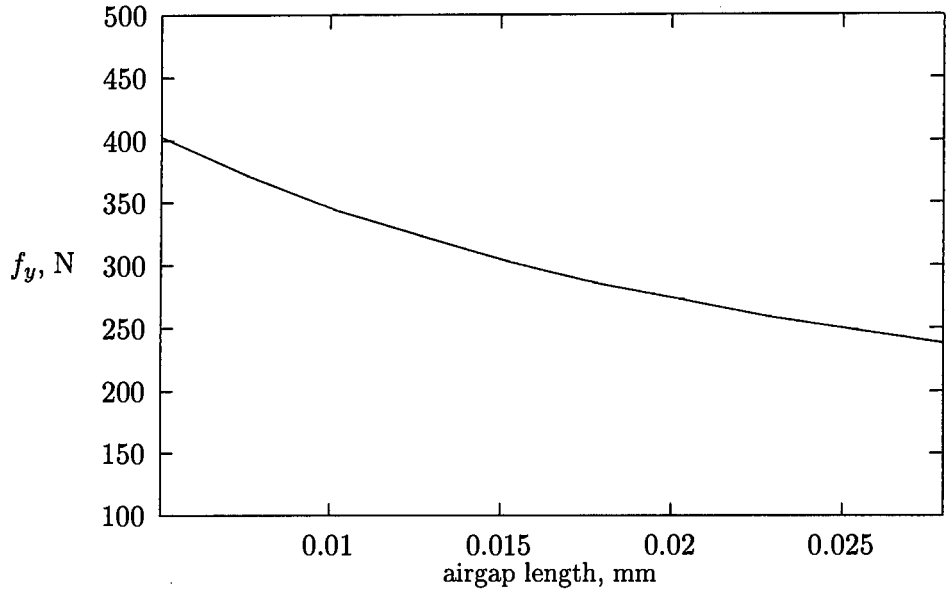

Figure 3.15: Calculated normal force between forcer and platen versus airgap length at current free state.

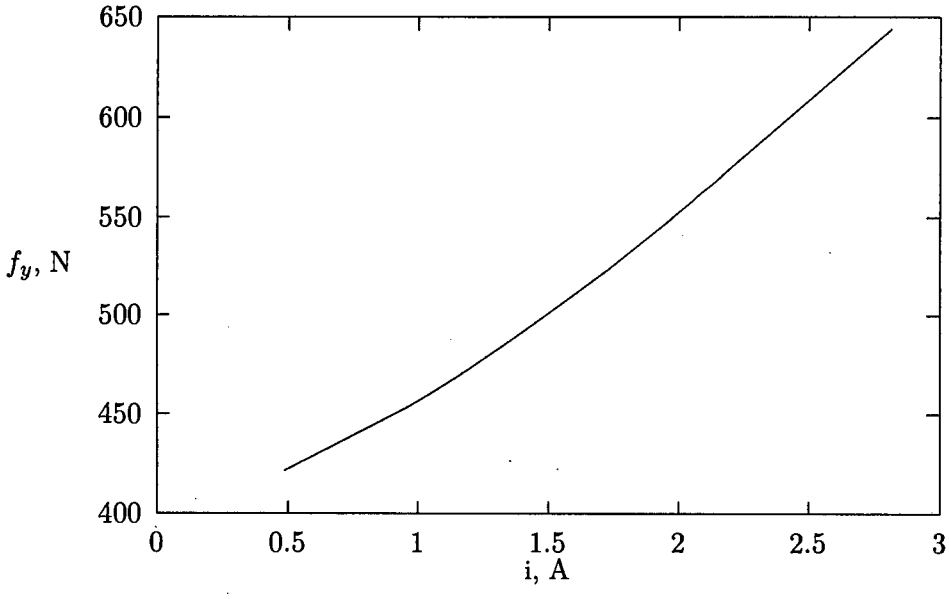

Figure 3.16: Normal force versus peak current.

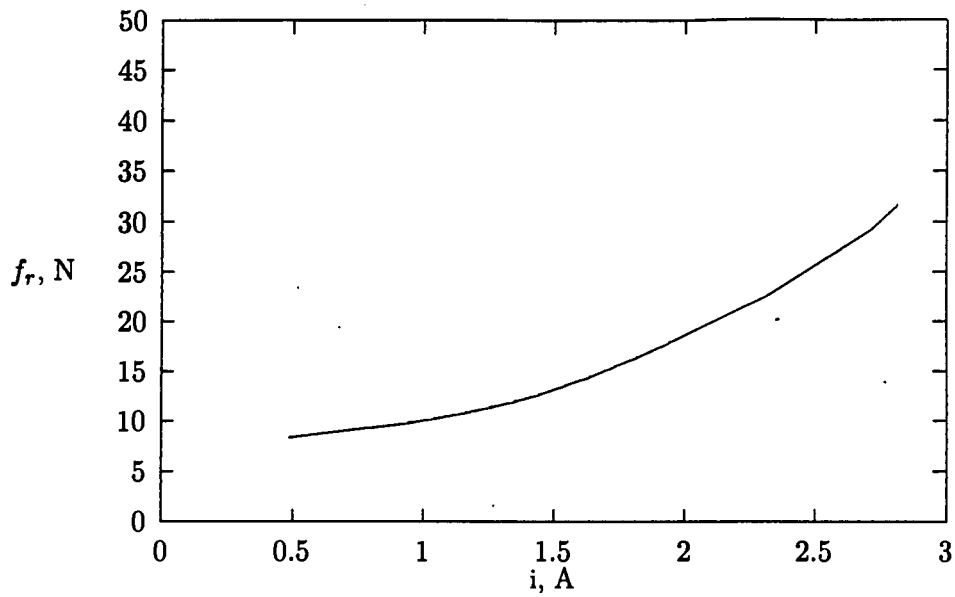

Figure 3.17: Amplitude of tangential force ripple as a function of peak current (two phases energised).

Chapter 4

Reluctance Network Approach

Although the FEM is a very effective method to deal with the analysis of electrical machines, it normally needs long computation time in the FEM analysis of large models even on fairly fast computers.

In recent years, a lot of research has been done on modelling electrical devices with the aid of the reluctance network method (RNM). Turowski and Wiak [43, 47] have extended the RNM even to the three dimensional non-linear magnetostatic field problems.

Part of this research relates to the stepping motors [29, 22, 24, 42]. Because of the hybrid stepping motors have many stator-rotor (forcer-platen) teeth configurations and their operating characteristics, especially the force (torque) characteristics, are greatly affected by the teeth and windings arrangements, it is necessary to develop the equivalent circuit for each structure separately. For those motors of asymmetrical structure, additional difficulties may arise.

In this chapter the equivalent magnetic circuit of the HLSM is first described, then the RNM combined with the co-energy principle is used for calculating motor performance.

4.1 Reluctance network concept

In the reluctance network method the cross-section of the machine has been replaced by flux tubes. The shape and the number of flux tubes vary with the flux path. The subdivision of a flux tube can be needed when a higher accuracy is required.

The basic element in the RNM is the reluctance element which can be represented by the following equation:

$$\Re_\mu = \int_l \frac{dL}{\mu S} \tag{4.1}$$

where L is the length of the flux tube, μ is the magnetic permeability and S is the cross section of the flux tube.

Each part of the machine such as stator/rotor (forcer/platen) and airgap can be modelled separately. Then the full network can be defined as a linear equation system, which satisfies the following integral equation:

$$\oint_l H \cdot dl = \mathcal{F}_{mmf} \tag{4.2}$$

where H is the magnetic field intensity and $\mathcal{F}_{mmf}$ is the overall MMF. The network model can finally be solved by circuital approach.

4.2 Magnetic circuit model

4.2.1 Equivalent circuit of the HLSM

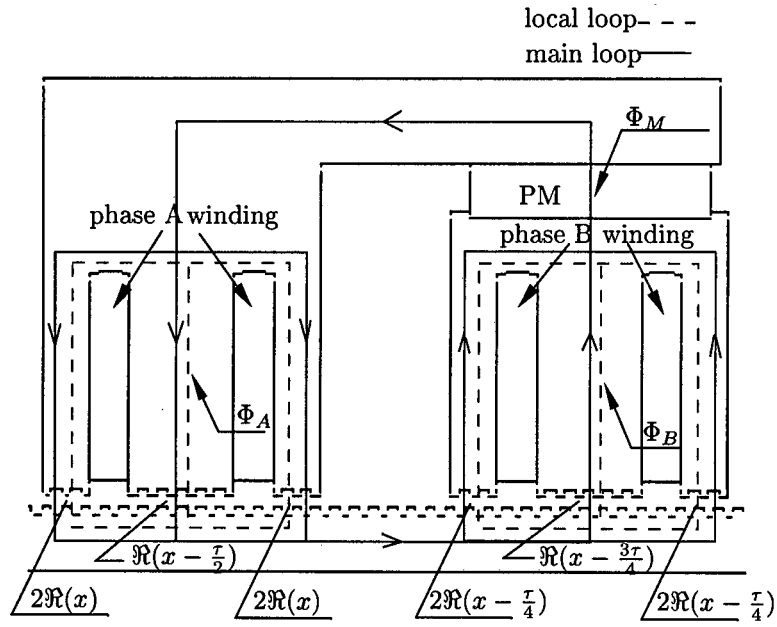

Figure 4.1: The outline of the magnetic circuit of a HLSM

For the approximate calculation of forces, a simple equivalent magnetic circuit is used. As shown in Fig 4.1, the fluxes of individual poles are dependent on the PM MMF, winding

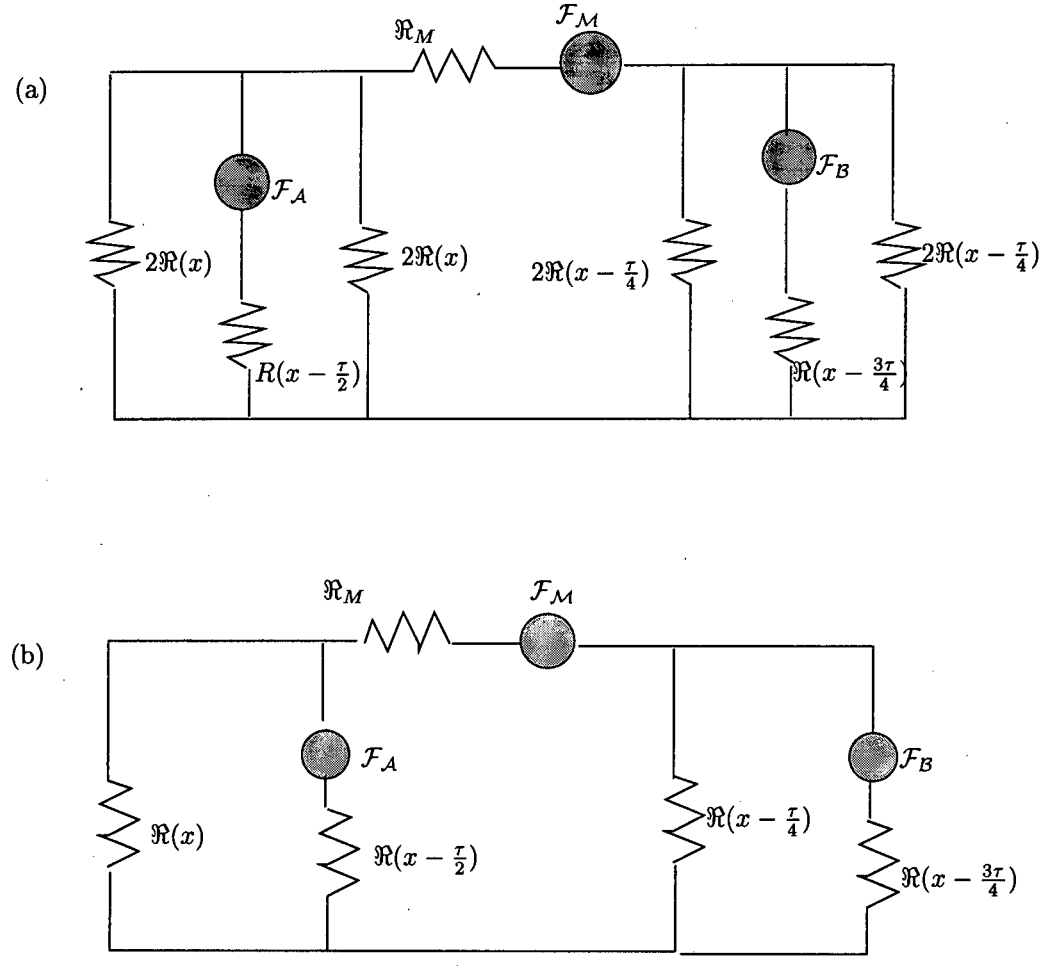

Figure 4.2: The equivalent magnetic circuit of a two-phase HLSM: (a) magnetic circuit corresponding to Fig. 4.1; (b) simplified magnetic circuit with equal number of teeth per pole.

currents and reluctances. The PM flux Φ_M circulates in the main loop while the winding excitation fluxes Φ_A and Φ_B create local flux loops.

Apart from these fluxes fringing and leakage flux exists which takes path entirely or partially through air or non-ferromagnetic parts of the forcer. The amount of such flux is small as compared with the main flux and can, therefore, be neglected. The equivalent magnetic circuit is obtained and shown in Fig. 4.2(a).

After further simplification, the circuit can be brought to that in Fig. 4.2(b), in which the $\mathcal{F}_M$, $\mathcal{F}_A$ and $\mathcal{F}_B$ are MMFs of the PM, phase winding A and B, respectively, $\Re(x)$, $\Re(x-\frac{1}{2}\tau)$, $\Re(x-\frac{1}{4}\tau)$ and $\Re(x-\frac{3}{4}\tau)$ are the reluctances corresponding to each pole (τ refers to the tooth pitch), which vary with the tooth alignments.

The following assumptions have been made in the above analysis to obtain a simplified reluctance network model:

- Since a highly permeable steel is used in both the forcer and platen, only the airgap and the PM reluctances are considered.
- Because the forcer is made of the thin laminations (0.3556 mm), the eddy current losses are negligible.
- The two-piece pole is equivalent to the one-piece pole.
- This method does not take into account the magnetic saturation.

4.2.2 Permeance model and its calculation

For calculation of tooth layer reluctance of the HLSM, the following formulae developed by Chai [4] have been used:

(a) for $0 \leq x \leq \frac{W_v}{2}$,

$$\Re = \frac{1}{\mu_0 L}[C1 + \frac{4}{\pi}\ln(1+\frac{\pi x}{2l_g}) + \frac{2}{\pi}\ln(1+\frac{\pi(W_v-2x)}{2l_g+\pi x}) + \frac{2x}{2l_g+\pi(W_v-x)}]^{-1} \tag{4.3}$$

(b) for $\frac{W_v}{2} \leq x \leq W_t$,

$$\Re = \frac{1}{\mu_0 L}[C1 + \frac{4}{\pi}\ln(1+\frac{\pi W_v}{4l_g}) + \frac{4}{\pi}\ln C2 + C3]^{-1} \tag{4.4}$$

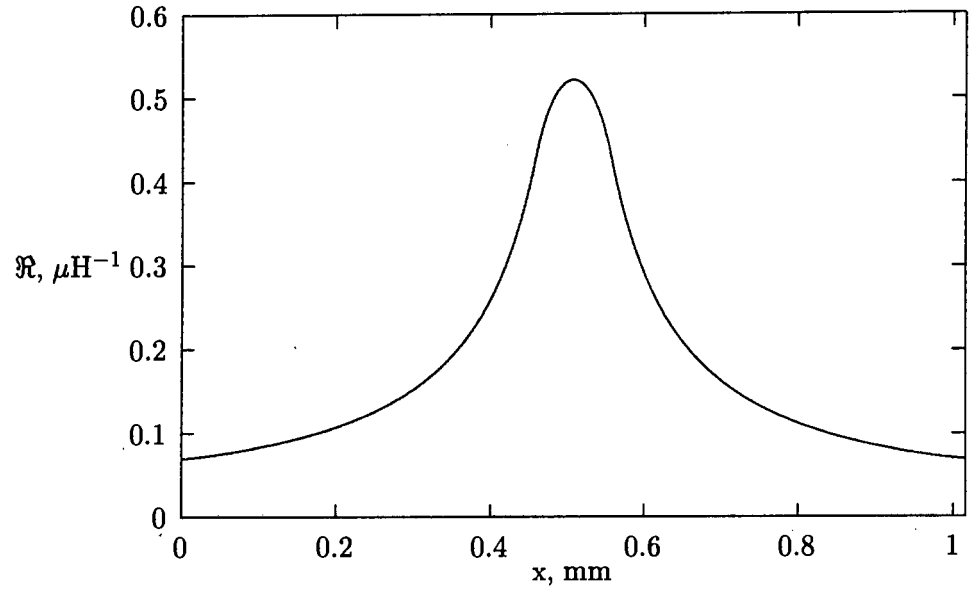

Figure 4.3: The airgap reluctance distribution over one tooth pitch

(c) for $W_t \leq x \leq \frac{W_v+W_t}{2}$,

$$\Re = \frac{1}{\mu_0 L}[C3 + \frac{4}{\pi}\ln(\frac{4l_g + \pi W_v}{4l_g + 2\pi(x - W_t)}) + \frac{4}{\pi}\ln C2 + \frac{2x - 2W_t}{2l_g + \pi(x - W_t)}]^{-1} \tag{4.5}$$

where C1, C2 and C3 are defined as,

$$C1 = \frac{W_t - x}{l_g} \tag{4.6}$$

$$C2 = \frac{4l_g + \pi W_v}{4l_g + 2\pi(W_v - x)} \tag{4.7}$$

$$C3 = \frac{2W_v - 2x}{2l_g + \pi(W_v - x)} \tag{4.8}$$

where W_t is the tooth width, W_v is the slot width, l_g is the airgap length, x represents the displacement between opposing teeth, L is the thickness of the tooth and $\Re$ is the reluctance of a pair of teeth.

For a pole consisting of n teeth, the reluctance of one pole is $\Re_p = \frac{1}{n}\Re_t$ where $\Re_t$ stands for the reluctance of a pair of teeth. The calculated reluctance per pole over one tooth pitch is shown in Fig 4.3.

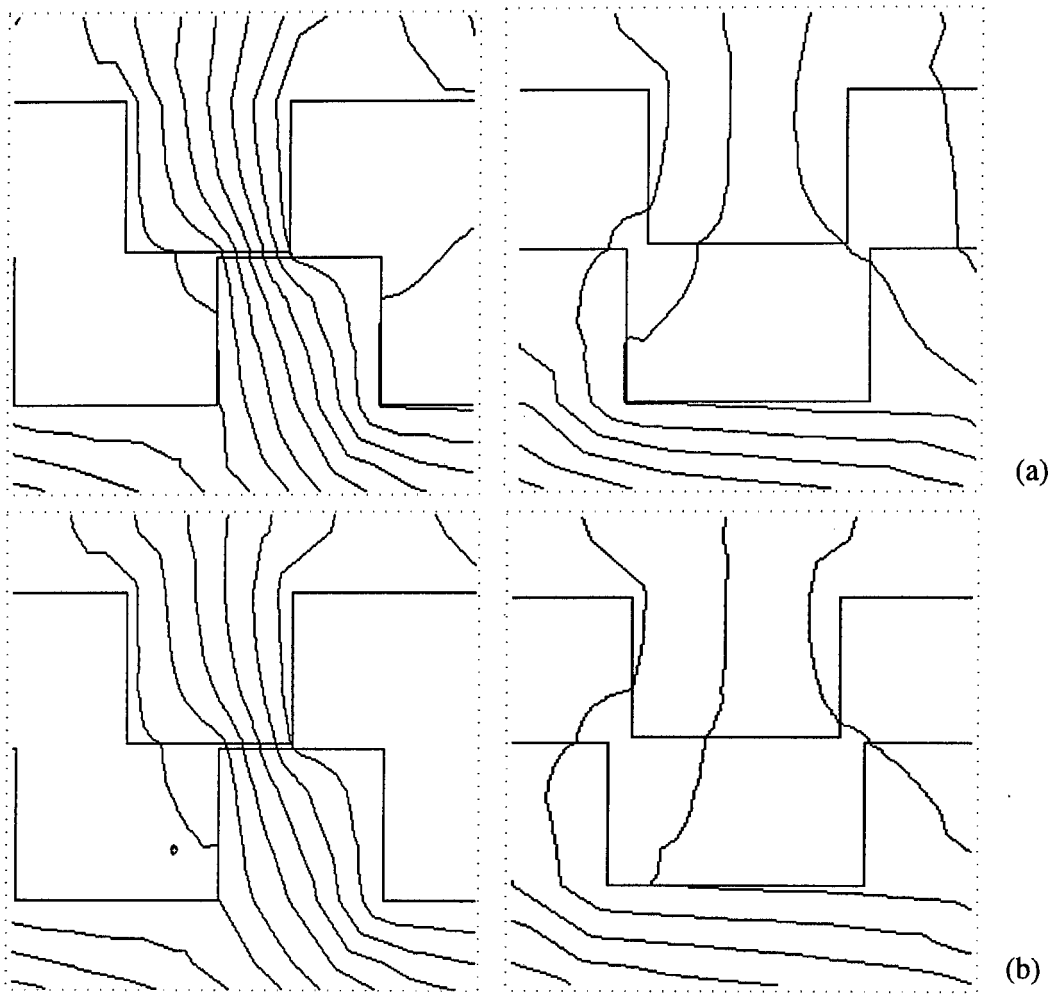

Figure 4.4: Comparison of flux patterns for partial alignment and misalignment of teeth: (a) high saturation, (b) low saturation.

In the non-saturated magnetic circuit ($\mu \to \infty$) all the flux lines are perpendicular to the magnetic material surfaces. As the teeth begin to saturate, which does happen in a practical motor, the effective length of the flux path in the air decreases (Fig 4.4). This results in a higher permeance for the flux emanating from the sides of teeth [4].

Toothed surface of the forcer and platen involves the permeance variation with respect to the linear displacement according to a periodical function. Similar as in [4], the permeance fluctuation can be approximated with the aid of the following equation:

$$P = \frac{1}{2}[(P_{max} + P_{min}) + (P_{max} - P_{min})\cos\frac{2\pi}{\tau}x] \tag{4.9}$$

where τ is the dimension of one tooth pitch and P_{max} and P_{min} are defined respectively as

$$P_{max} = \mu_0 L[\frac{W_t}{l_g} + \frac{2}{\pi}\ln(1 + \frac{\pi W_v}{2l_g})] \tag{4.10}$$

$$P_{min} = \mu_0 L[\frac{W_v - W_t}{l_g + 0.25\pi(W_v - W_t)} + \frac{8}{\pi}\ln\frac{l_g + 0.25\pi W_v}{l_g + 0.25\pi(W_v - W_t)}] \tag{4.11}$$

The approximation can further help finding the derivative of reluctance with respect to the displacement, i.e.

$$\frac{\partial P}{\partial x} = -\frac{\pi}{\tau}(P_{max} - P_{min})\sin\frac{2\pi}{\tau}x \tag{4.12}$$

The calculated permeances over one tooth pitch by using Chai's permeance formulae and its periodical approximation are plotted in Fig 4.5. The space harmonics distribution obtained by applying the fast Fourier transform (FFT) to the curve (calculated from Chai's permeance formulae) is displayed in Fig 4.6. It can be seen that the higher harmonics are very small when compared with the 1st harmonic component and therefore can be neglected. This approximation leads to the small discrepancies between the results in Fig 4.5.

4.2.3 Modelling of the permanent magnet

In the magnetic circuit approach the PM can be modelled as an MMF source $\mathcal{F}_{\mathcal{M}}$ in series with an internal reluctance $\Re_M$ [9] and described by the following equations:

$$\mathcal{F}_M = \frac{B_r h}{\mu_0 \mu_r} \tag{4.13}$$

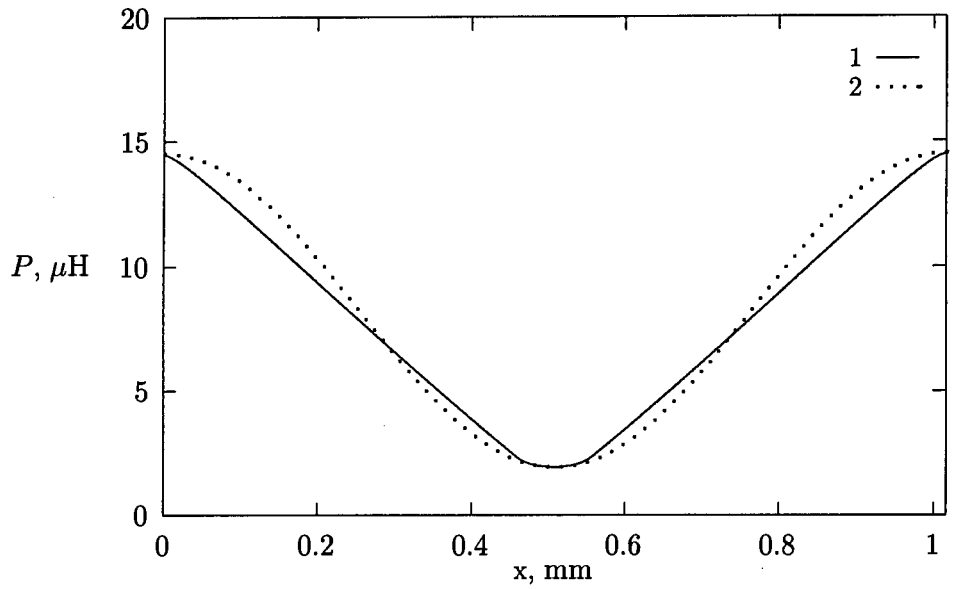

Figure 4.5: Comparison of calculated permeance per pole. (1) according to eqns 4.3 to 4.8, (2) according to eqn 4.9.

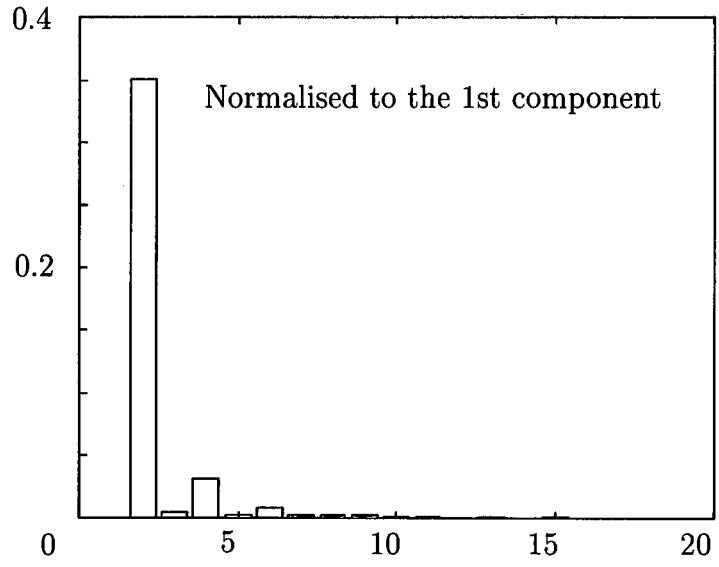

Figure 4.6: Space harmonic distribution of permeance.

$$\Re_M = \frac{h}{\mu_0 \mu_r S} \tag{4.14}$$

where B_r is the remanent flux density, h is the full length of the PM in the polarisation direction, μ_r is the relative permeability of the PM and S is the cross-section area of the PM.

4.2.4 Phase current waveform and excitation MMF

In microstepping mode the phase current waveform of the HLSM is of sinusoidal shape. As described in Chapter 1, the third harmonic of amplitude I_3 has been added to or subtracted from the phase currents to suppress the force ripple.

For comparison purposes, the pure sinusoidal excitation case in which phase A was driven by the pure cosine wave while phase B with the pure sine wave has also been simulated. The general current waveforms are given as follows [9]:

$$i_A = I_1 \cos(\frac{2\pi x}{\tau} - \phi) \pm I_3 \cos(\frac{6\pi}{\tau} - 3\phi) \tag{4.15}$$

$$i_B = I_1 \sin(\frac{2\pi x}{\tau} - \phi) \pm I_3 \sin(\frac{6\pi}{\tau} - 3\phi) \tag{4.16}$$

where ϕ is the phase angle depending on the load. The MMFs for phase A and B can be simply written as

$$\mathcal{F}_A = N_c i_A \tag{4.17}$$

$$\mathcal{F}_B = N_c i_B \tag{4.18}$$

where N_c is the number of turns for each phase winding which are assumed to be identical.

4.3 Principle for calculation of HLSM performance

4.3.1 Calculation of flux

For the calculation of either tangential or normal forces, it is always necessary to find the flux of each pole. However, there is no shortcut for the flux calculation. This is because the flux of each pole has to be determined by the winding MMFs, PM flux and all the reluctances.

The flux of each pole can only be obtained by solving the magnetic circuit model as shown in Fig 4.2.

4.3.2 Tangential force calculation

Having built the reluctance network model, next step is to evaluate the reluctance forces of the HLSM. According to the co-energy principle the tangential force is the change in the stored energy as the relative position (in x – direction) between the forcer and the platen changes. The tangential force per pole is then

$$F_{xp} = \frac{1}{2}\Phi^2\frac{\partial \Re}{\partial x} = -\frac{1}{2n}\Phi^2[\frac{1}{P^2}\frac{\partial P}{\partial x}] \tag{4.19}$$

where Φ is the flux through the pole. Thus for an m pole HLSM, the overall available tangential force is simply

$$F_t = -\sum_{i=1}^{m}\frac{1}{2n}\Phi^2[\frac{1}{P^2}\frac{\partial P}{\partial x}] \tag{4.20}$$

4.3.3 Normal force calculation

The normal force can be written in the form of the derivative of co-energy W with regard to the airgap length l_g, i.e.

$$F_n = \frac{\partial W}{\partial l_g} = -\sum_{i=1}^{m}\frac{1}{2n}\Phi^2[\frac{1}{P^2}\frac{\partial P}{\partial l_g}] \tag{4.21}$$

The derivative of the permeance per tooth against airgap length can be found by:

(a) for $0 \leq x \leq \frac{W_v}{2}$,

$$\frac{\partial P}{\partial l_g} = \mu_0 L[\frac{x - W_t}{l_g^2} - \frac{2x}{l_g(l_g + 0.5\pi x)} + \frac{2x - W_v}{C_2 C_1} - \frac{x}{C_1^2}] \tag{4.22}$$

(b) for $\frac{W_v}{2} \leq x \leq W_t$,

$$\frac{\partial P}{\partial l_g} = \mu_0 L[\frac{x - W_t}{l_g^2} - \frac{W_v}{l_g C_2} + \frac{x - W_v}{C_1^2} + \frac{W_v - 2x}{C_1 C_2}] \tag{4.23}$$

(c) for $W_t \leq x \leq \frac{W_v + W_t}{2}$,

$$\frac{\partial P}{\partial l_g} = \mu_0 L[\frac{x - W_v}{C_1^2} + \frac{W_t - x}{C_3^2} + \frac{W_v - 2x}{C_1 C_2} + \frac{2(x - W_t - 0.5W_v)}{C_2 C_3}] \tag{4.24}$$

where C_1, C_2 and C_3 are,

$$C_1 = l_g + 0.5\pi(W_v - x) \tag{4.25}$$

$$C_2 = l_g + 0.25\pi W_v \tag{4.26}$$

$$C_3 = l_g + 0.5\pi(x - W_t) \tag{4.27}$$

4.4 Reluctance network simulation

4.4.1 Computer flow chart

In accordance with the previous sections of this chapter a computer program has been written to conduct the magnetic circuit analysis.

The simulations have been done for different excitation modes including current-free, one-phase on and two-phase on states. When two phases are energised, the pure sinusoidal excitation mode has first been considered.

Then the techniques of ripple force suppression by either adding or subtracting certain amount of the 3rd of harmonic have been simulated. Fig 4.7 shows the flow chart for the instantaneous forces computation.

4.4.2 Calculated HLSM steady-State characteristics

Following the above mentioned procedures, the steady-state characteristics of the HLSM have been calculated as shown in Figs 4.8 to 4.13.

Static characteristics

The calculated static characteristics of the HLSM are given in Figs 4.8 and 4.9. The obtained maximum holding force at rated current (2.721 A) is close to 140 N.

In general, the holding force varies with the peak excitation current forming a linear curve. This is not true in a practical machine since the magnetic saturation does occur even when no current is applied to the HLSM.

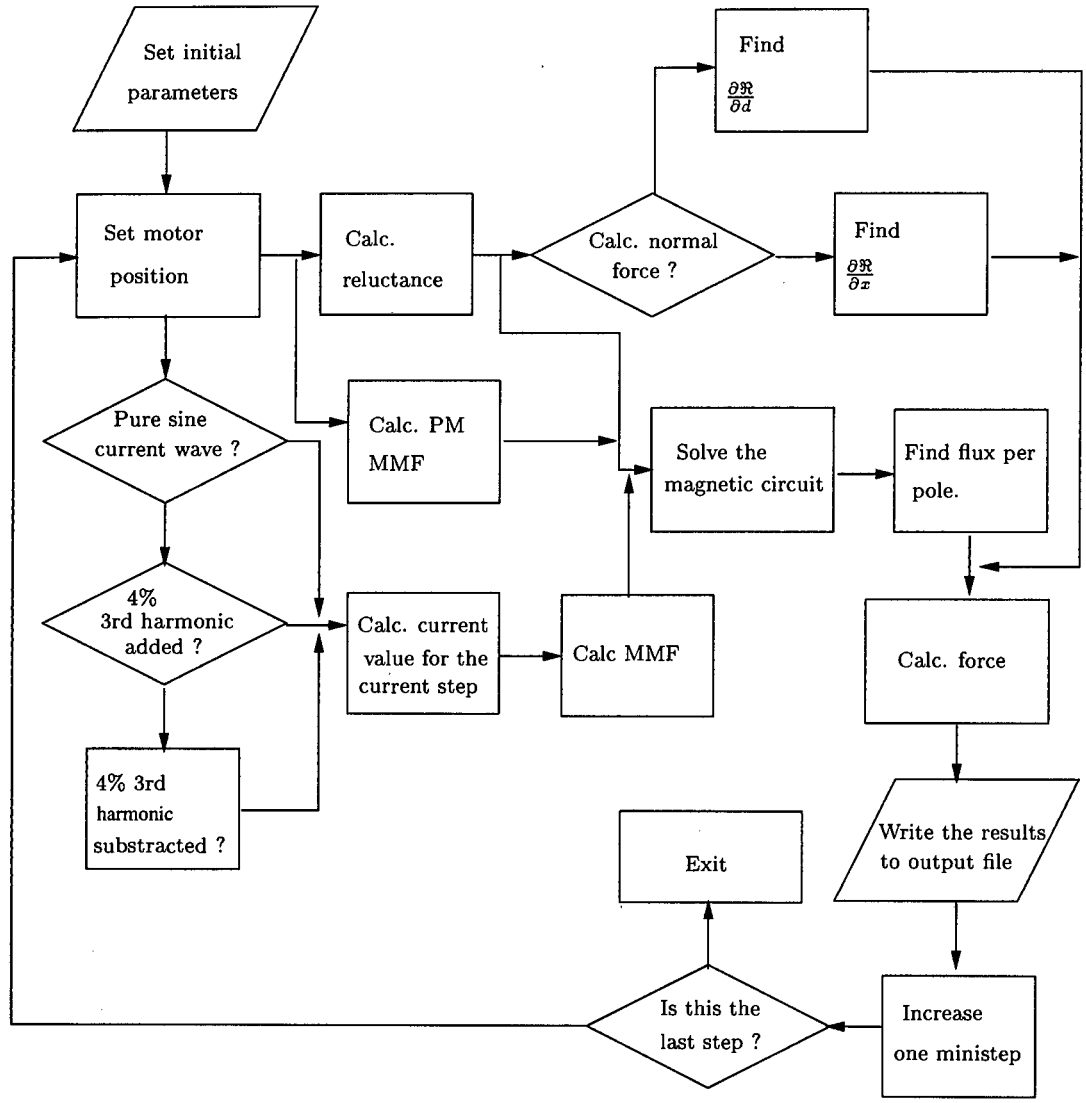

Figure 4.7: The chart of logical flow of the instantaneous force calculation

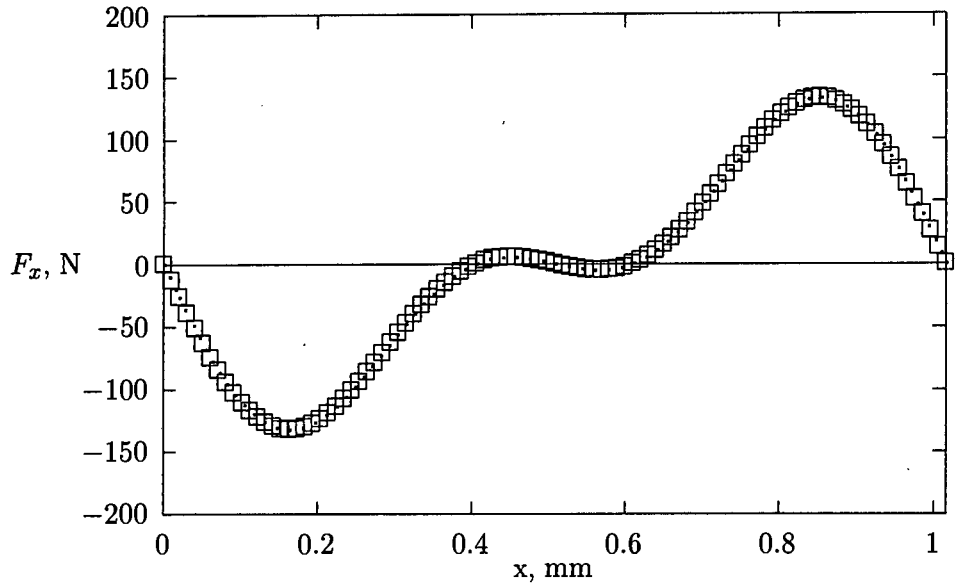

Figure 4.8: Calculated static characteristics using the RNA method (one phase is excited, current 2.721A)

Instantaneous characteristics

Figs 4.10 to 4.13 show the simulated instantaneous forces corresponding to different excitation profiles. It can be seen that the ripple forces cannot be effectively suppressed by either adding to or subtracting from the phase current 4% of the 3rd harmonic (as shown in Fig 4.12).

However, significant improvement of force ripple can be achieved by adding certain amount of the 3rd harmonic to one phase while subtracting the same amount from the other phase (see Fig 4.11). Fig 4.13 shows that the more the current is applied the larger the force ripple is produced.

Normal force characteristics

The normal force as a function of the airgap length when two phases are energised has been calculated and plotted in Fig 4.14. It can be seen that the attraction force between the forcer and the platen can be very high and very sensitive to the small change in the airgap length. The predicted normal force for an airgap of 0.0127 mm is about 493.86 N.

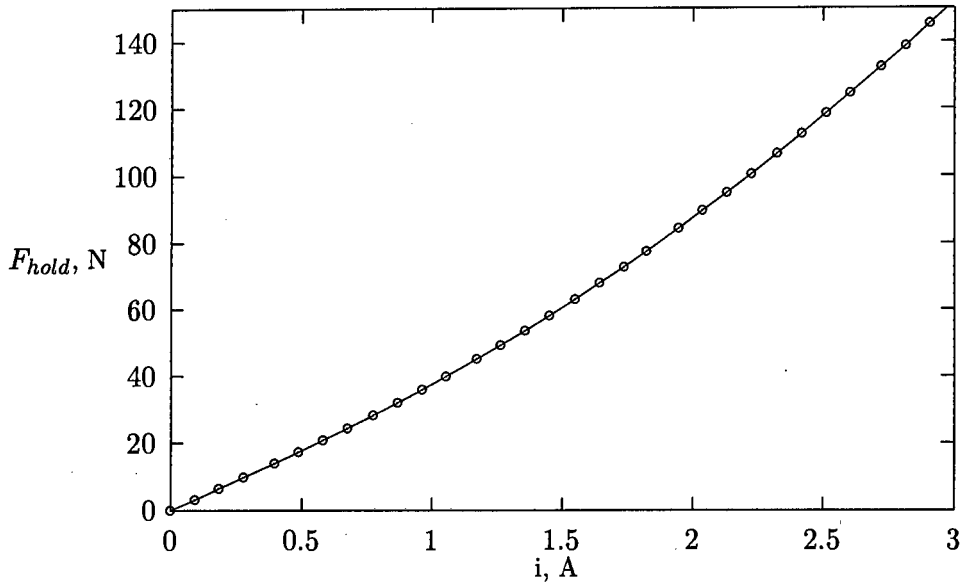

Figure 4.9: Holding force versus peak phase current

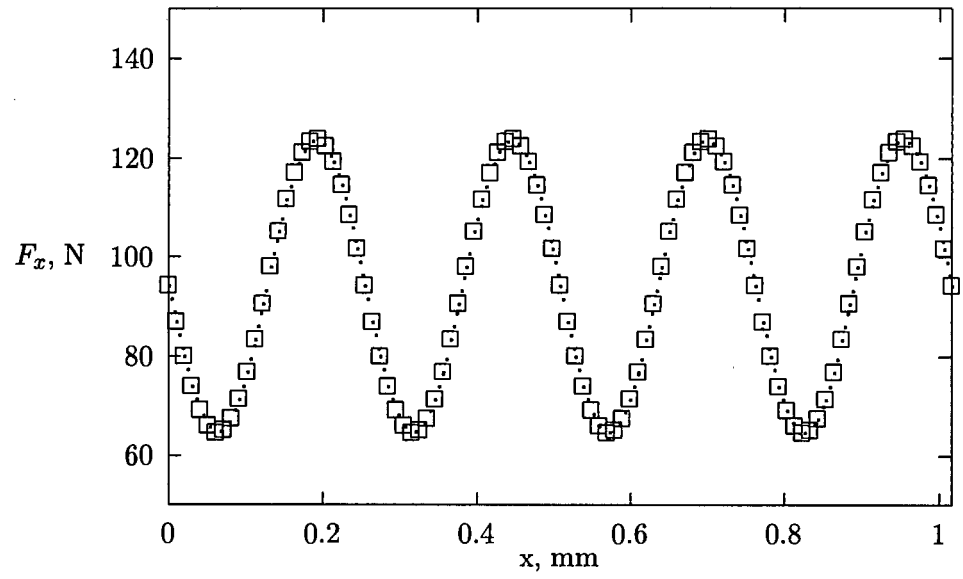

Figure 4.10: Calculated instantaneous force using the RNA method (when phase A is driven by pure sine wave and phase B with pure cosine wave)

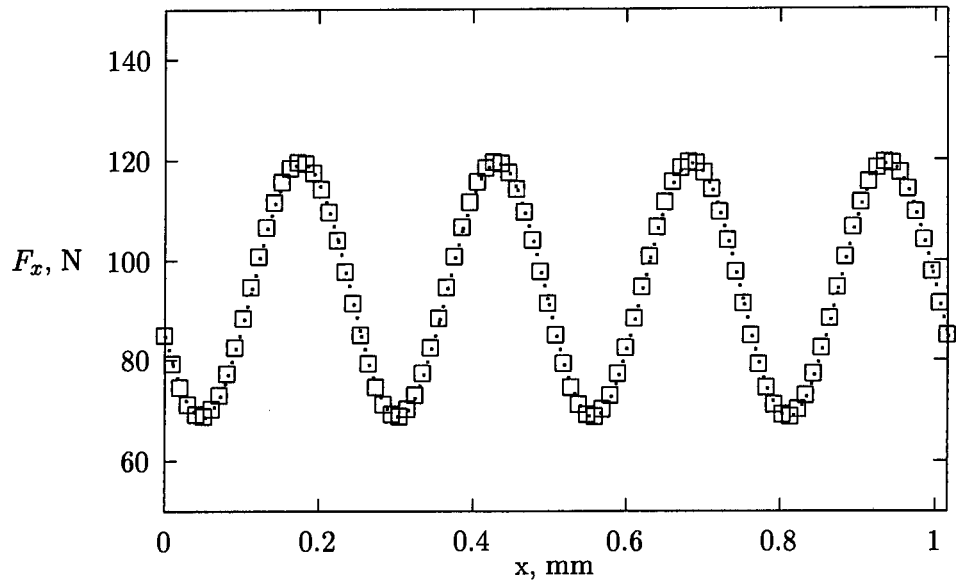

Figure 4.11: Calculated instantaneous force using the RNA method (when ±10% of the 3rd harmonic has been injected into phase current)

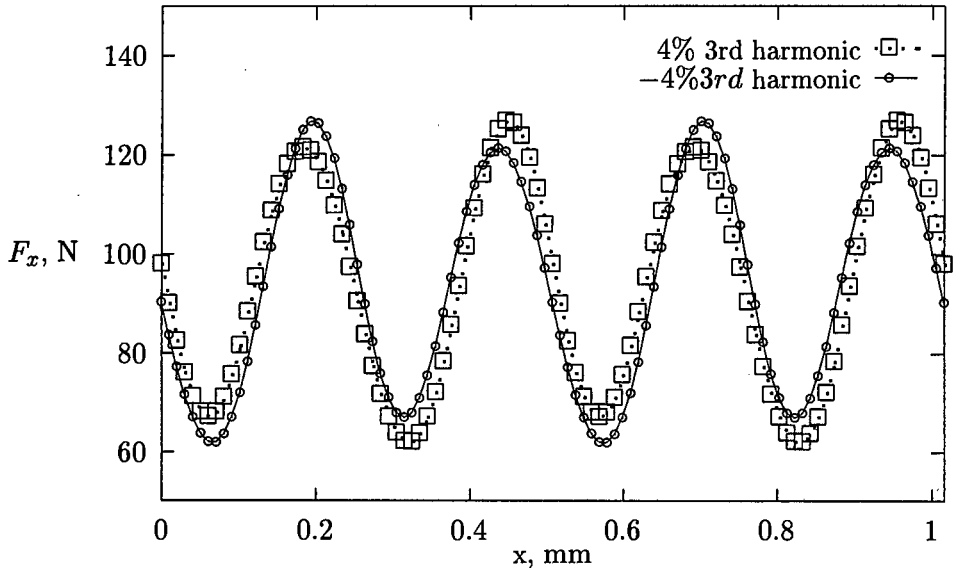

Figure 4.12: Calculated instantaneous forces using the RNA method (with ±4% of the 3rd harmonic injected into phase current)

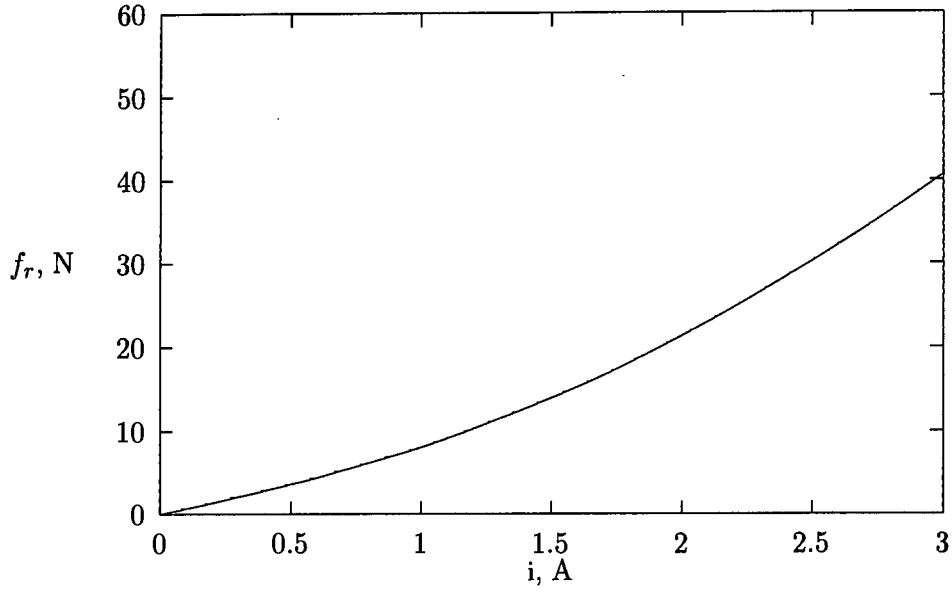

Figure 4.13: Amplitude of tangential force ripple as a function of peak current (two phases on).

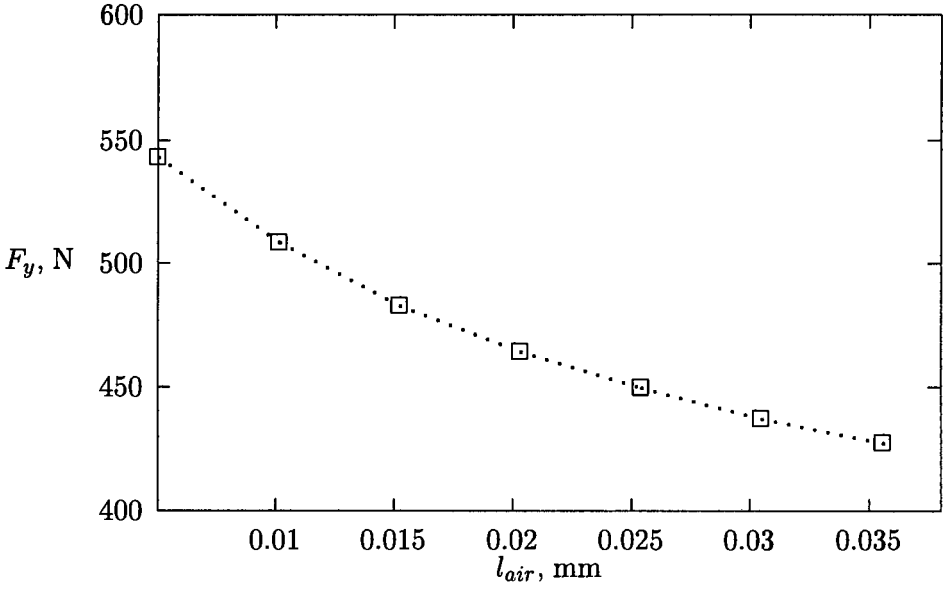

Figure 4.14: Normal force as a function of airgap length (two phases on).

Chapter 5

Comparison of Results Obtained from FEM, RNA and Measurements

5.1 Comparison of static characteristics

The following static characteristics have been compared: (1) static force versus forcer position and (2) holding force versus peak phase current when only one phase of the HLSM is fed with peak phase current. The results obtained from the FEM, RNA and measurements are shown in Figs 5.1 and 5.2.

It can be seen that the maximum holding force from the FEM, measurements and RNA are 70N, 85N and 120N, respectively. The FEM results correlate well with the experimental results in the case of static characteristics simulation. The RNA tends to overestimate the force since a lot of assumptions have been made to simplify the calculations.

5.2 Comparison of instantaneous characteristics

The instantaneous characteristic of the HLSM refers to the output tangential force versus motor position when the HLSM has been powered up and reaching its steady state. Different excitation current waveforms have been used in both testing and simulations. They are pure-sine wave excitation, quasi-sinusoidal (with 4% of the 3rd harmonic added), quasi-sinusoidal (with 4% of the 3rd harmonic subtracted), quasi-sinusoidal (with 10% of the 3rd harmonic added), respectively.

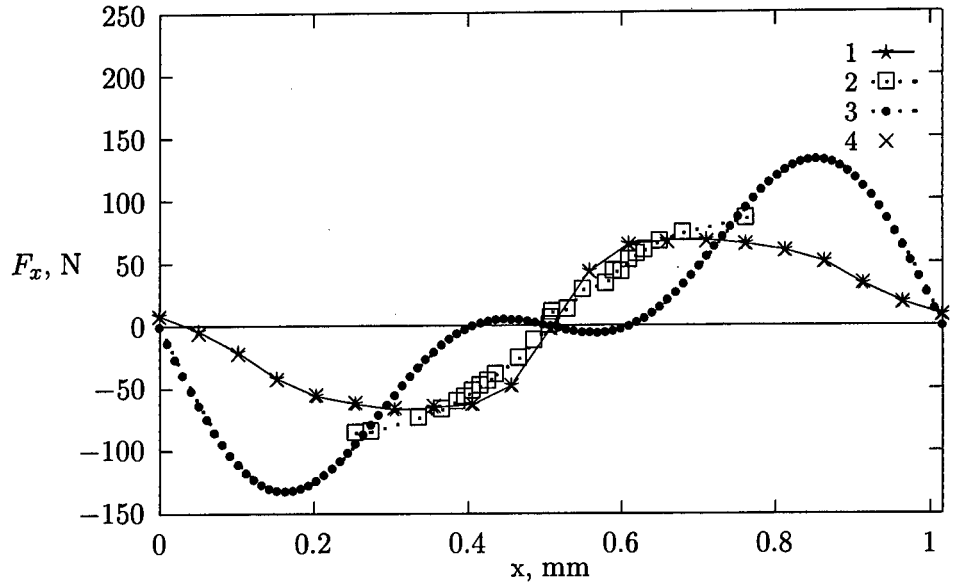

Figure 5.1: Comparison of tangential force-displacement characteristics (when one phase of the motor is fed with 2.7 A), where 1– Coulomb's approach, 2– measurements, 3– reluctance network approach, 4– Maxwell stress tensor.

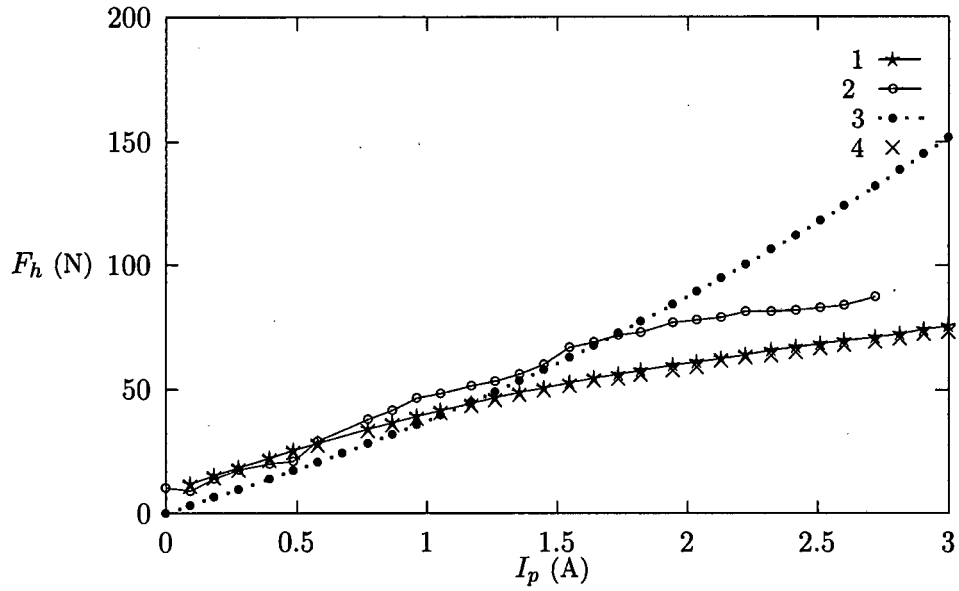

Figure 5.2: Comparison of holding force–current characteristics, where 1– Coulomb's approach, 2– measurements, 3– reluctance network approach, 4– Maxwell stress method.

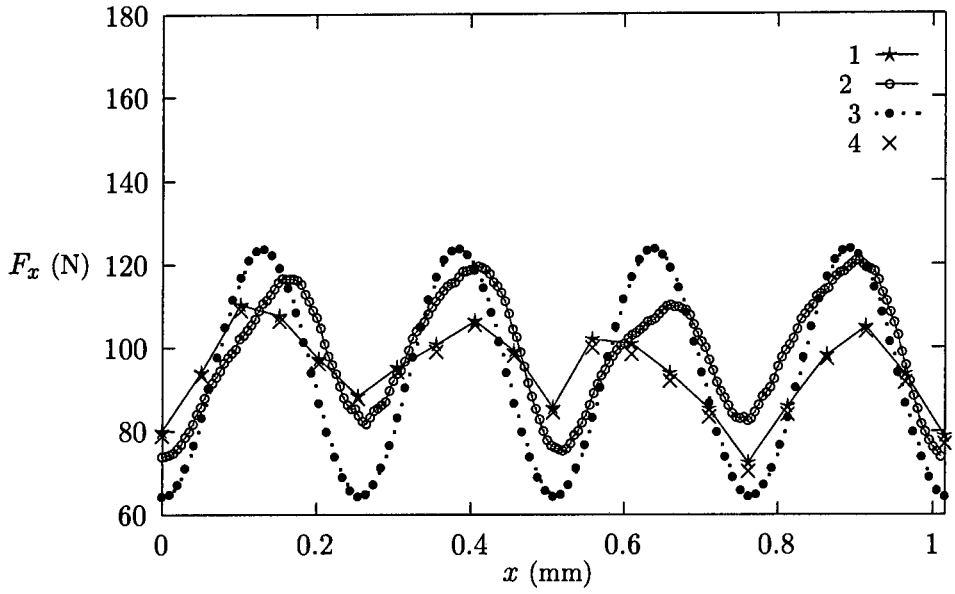

Figure 5.3: Comparison of instantaneous tangential force versus displacement (when the phase A of the HLSM is driven with pure sine wave and phase B with pure cosine wave): 1– Coulomb's approach, 2– measurements, 3– reluctance network approach, 4– Maxwell stress method.

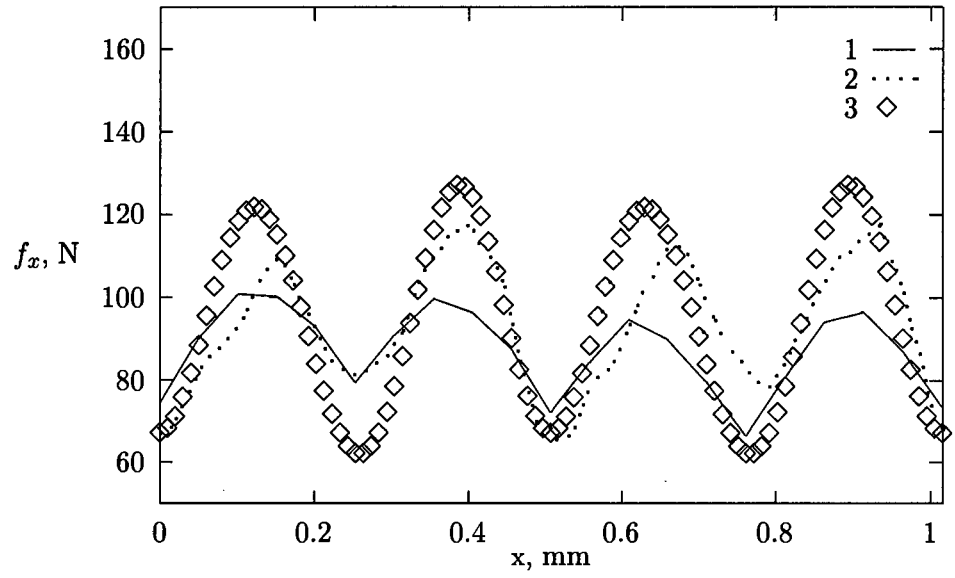

Figure 5.4: Comparison of instantaneous tangential force versus displacement (when 4% of $3rd$ harmonic has been injected into phase current): 1– Coulomb's approach, 2– measurements, 3– reluctance network approach.

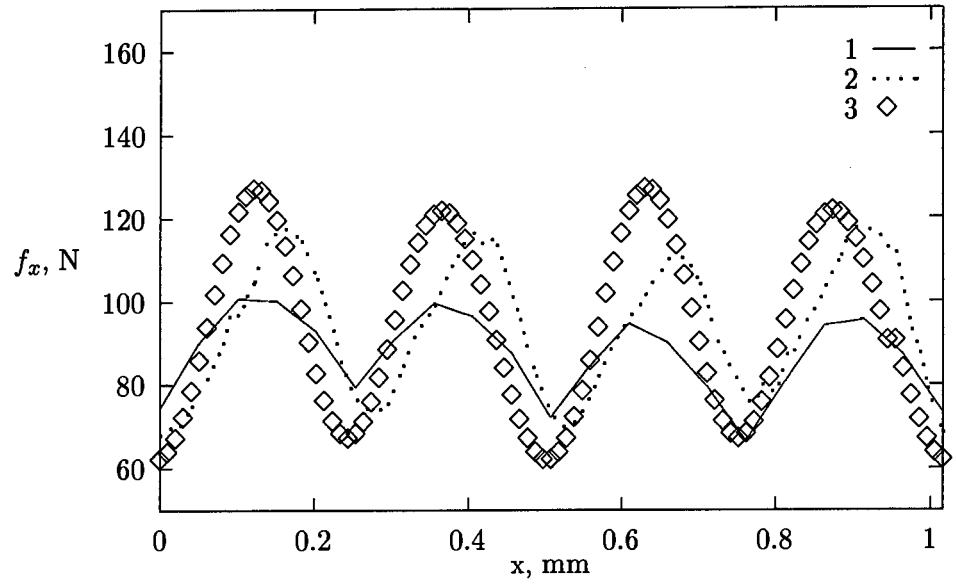

Figure 5.5: Comparison of instantaneous tangential force versus displacement (when 4% of $3rd$ harmonic has been subtracted from phase current): 1– Coulomb's approach, 2– measurements, 3– reluctance network approach.

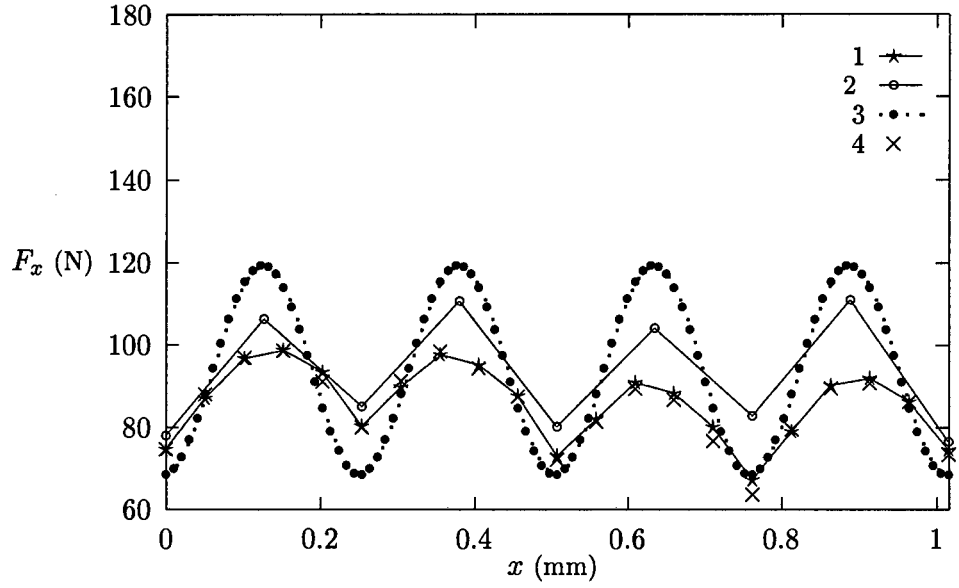

Figure 5.6: Comparison of instantaneous tangential force versus displacement (when 10% 3rd harmonic has been injected into phase current): 1– Coulomb's approach, 2– measurements, 3– reluctance network approach, 4– Maxwell stress method.

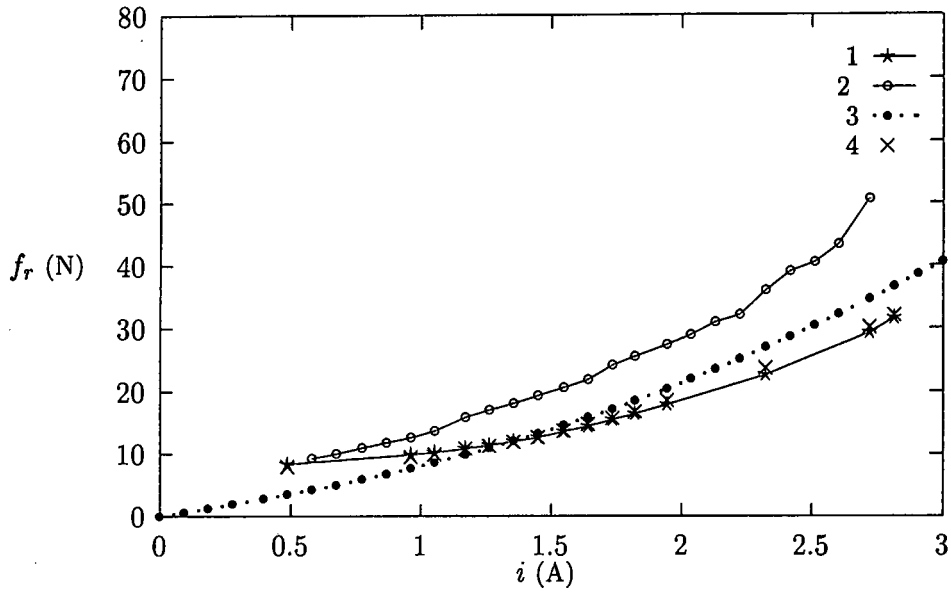

Figure 5.7: Comparison of tangential force ripple amplitude as a function of peak current, where 1– Coulomb's approach, 2– measurements, 3– reluctance network approach, 4– Maxwell stress method.

The simulated results from both the FEM and RNA are then plotted and compared with measurements as shown in Figs 5.3 to 5.7. Since the HLSM was moving at a constant speed 0.0508m/s, the force – time curves can be easily transferred to the force – displacement curves.

It can be seen (Figs 5.3 and 5.4) that the tangential force ripple can be improved by injecting the 3rd order harmonic into the phase current. The amplitude of tangential force ripple is defined as the difference between the maximum and the minimum force values within one period. Fig 5.7 gives the relationship between the amplitude of tangential force ripple and the peak current, which has been obtained by calculating the maximum force ripple for each peak value of the excitation current.

In general, both the RNA and the FEM show quite reasonable agreement with the experimental data. However, the RNA has a tendency to overestimate the forces while the Coulomb's approach produces results that are lower than measurements. The RNA is a very efficient approach considering the computation time.

Owing to the existence of the rare earth PMs, there is a very strong normal force between the forcer and the platen even when the HLSM is unenergised. The normal force measurements could not be done since the suitable equipment was not available.

5.3 Comparison of different approaches

5.3.1 Finite element method

The reasons for the discrepancies between the measured and the calculated results are numerous and differ for the RNA and FEM. The major factors contributing to the errors in the FEM computations are discussed below.

1. *Discretization of small airgap* might be insufficient. The HLSM possesses a very small airgap (less than 10^{-3} of the overall dimensions of the device) and the finite element simulation program has a limitation of $5,100$ nodes for each FE model, which made it only possible to put a single layer of elements in the airgap region. This may have remarkable effects on the accuracy of force calculations since several layers of elements are often needed across the airgap for achieving better accuracy.

2. *Edge effects* in the HLSM have been neglected. The used FE package can only conduct 2D FE analysis, thus the edge effects could not be considered. In the aligned position, the problem may not be serious. However, in the unaligned position, this can affect the accuracy of the field calculation and consequently performance calculations.

5.3.2 Reluctance network approach

The sources of the errors in the reluctance network analysis can be identified in a number of areas as discussed below.

1. The reluctance network analysis is based on the one-dimension model. For small electrical motor, the edge effects are significant and cannot be neglected.

2. The simplified permeance model is based on the assumption that the flux lines are perpendicular to the magnetic material surfaces. Thus it does not take into account any magnetic saturation, which does happen in the practical motor (especially in the tooth layer).

3. It has also been assumed that no MMF drop occurred when the flux pass through the laminated and solid cores, which results in overestimating the flux densities in the airgap region and certainly the output forces.

4. The inner pole of the HLSM has been considered equivalent to the outer two-piece pole. This is not the real situation since it can be viewed from the FE flux plot that there exists an imbalance of flux distribution between these poles.

5.3.3 Experimental investigation

In addition, the errors in the measurements cannot be ignored since it can affect the true accuracy of the simulations. For example, there are variations of the impedance of windings with temperature, non-uniform airgap and phase current shift of the controller.

5.4 Accuracy of the force calculation methods

5.4.1 Comparison of the methods for force calculations

The *Maxwell stress tensor*, Coulomb's approach and classical virtual work method are very often used in the calculation of forces and torques. They use different calculation algorithms and are favoured over one another from case to case [25, 30]. The first two methods need only one FE solution so that they are relatively time efficient while the last one requires two FE solutions to determine a force.

The *Maxwell stress tensor* method is regarded as the simplest method of force calculation since it needs only the magnetic flux density along a path within the airgap. However the discretization of the FE model and the selection of the integrating paths can greatly affect its accuracy.

In principle, the classical virtual work is an excellent method since it takes the energy of the whole model instead of a small region into account. This makes it possible to use much coarser mesh for force calculations. However, the finite difference approximation to the co-energy derivative can introduce significant round-off errors. Thus, determination of small incremental displacement is very important to the accuracy. Since the most suitable value of displacement is unknown and must be estimated first and then kept improving on until the satisfied results can be obtained.

The Coulomb's approach can avoid the lengthy trial-and-error procedure which is needed to find the ideal incremental displacement in the classical virtual work method. One FE solution is adequate for finding one force, which makes it an efficient approach in terms of the computation time needed.

From Figs 5.1 to 5.7 it can be seen that the *Maxwell stress tensor* method and the Coulomb's approach give very similar results in all the force calculations. Theoretically, the *Maxwell stress tensor* and the virtual work method should give the same results if a good integration path for the *Maxwell stress tensor* has been chosen. In the FE package used for the simulation, the field of interests is sampled at 1,024 points along the user-defined contour

to calculate the force. This cannot guarantee that each point lies in the centre of the element. The Coulomb's approach, however, extracts field value right from the centre of each element so that it is more accurate and flexible when the numerous airgap elements are used.

5.4.2 Comparison of computation time

The *Maxwell stress tensor* and the Coulomb's approach consume, in general, the same amount of time though the post-FE calculation in Coulomb's method takes 3-4 minutes extra time. However, the CVW method requires longer computation time that is twice as much as that needed by using the *Maxwell stress tensor*. A comparison of the processing time for using different approaches has been given in Table 5.1

Table 5.1: Processing time for different force calculation methods

Methods for force calculation	CPU time (s) 1st order solve.	CPU time (s) 2nd order solver	CPU time (s) 3rd order solver
Maxwell stress tensor	1536	6351	28579
Coulomb's approach	1587	6609	28877
Classical virtual work	3072	12662	57158

The computation time will be tremendously increased when a high-order solver is used to improve the accuracy of the solution. It has been noticed in the FE simulation that the improvement of the solution accuracy is less than 0.8% when the 3rd order solver is invoked to re-solve the model that has just been solved by using the 2nd order one. So the 2nd order solver is a good compromise between the computation time and the accuracy.

4. In the case of normal force pulsation, better improvement can be achieved by using the harmonic-subtracted profile than the harmonic-added scheme

5. An augment in the amplitude of excitation current results in an increase in the amplitude of force ripple, however, they are not a sort of linear relation

6. The steady-state tests also reveal that the stepping resolution of the HLSM has no significant influence on the amplitude of force ripple.

6.2.2 Transient tests

The transient tests covered the start-up and braking characteristics of the HLSM . It has been found that:

1. The higher the mass is attached the longer the settling time is needed in the start-up process while higher mass results in short settling time in the braking tests.

2. The higher the step resolution is set, the less the settling time is required in both start-up and braking processes.

6.3 Possible future research in the field

The recommendations that can be made about future research in the HLSMs are given as following:

1. The edge effects can not be ignored in small electric machines. It is thus recommended that the 3D FEM simulation should be performed.

2. A simplified reluctance network model has been used in the classical simulation. The magnetic saturation, reluctance of the iron core and the edge effect were not considered. A nonlinear 3D reluctance network may need to be formed to take into account these important aspects.

3. The combination of the finite element simulation with the classical circuital approach can take the advantage of a good accuracy from the FEM without significant increase in computation time when compared with the conventional classical approach. This can be done by using the following steps:

   (a) performing the FEM analysis on the tooth-layer models which calculates the tooth-layer permeances for different tooth alignments (as proposed in Appendix C)

Bibliography

[1] P. Acarnley. *Stepping motors: A guild in modern theory and practice.* Peter Peregrinus Ltd., Stevenage, UK, 1982.

[2] A. Basak and A. F. Filho. "Design, analysis and test of a novel slotless linear stepping motor,". *ICEM'94 Paris, vol.2,* pages 98–100, 1994.

[3] P. Campbell. *Permanent Magnet Materials and their Application.* Cambridge University Press, Cambridge, 1994.

[4] H. Chai. "Permeance Model and Reluctance Force between Toothed Structures,". *from the book, Theory and Applications of Step Motors, B.C. Kuo ed., West Publishing,* pages 141–153, 1974.

[5] M. Chari and P. S. ed. *Finite Element in Electrical and Magnetic Field Problems.* John Wiley & Sons, New York, 1980.

[6] E. communication with Professor H. Yamada's laboratory at Shinshu University, 1997.

[7] J. Coulomb and G. Meunier. "Finite Element Implementation of Virtual Work Principle for Magnetic or Electric Force and Torque Computation,". *IEEE Trans. Magnetics, Mag-20(5),* pages 1894–1896, 1984.

[8] J. Edwards and E. Freeman. *MagNet 5.1 User Guide - Using the MagNet Version 5.1 Package from Infolytica.* published by Infolytica,London and Montreal, 1995.

[9] S. Ellerthorpe and J. Blaney. "Force estimation for linear step motor with variable airgap,". In *25th Annual Symposium on Incremental Motion Control System and Devices,* pages 327–335, San Jose, CA, 1996.

[10] E. Favre, L. Cardoletti, and M. Jufer. "Permanent Magnet Synchronous Motors: A Comprehensive Approach to Cogging Torque Suppression,". *IEEE Trans. Ind. Applications, vol.29, no.6,* pages 1141–1149, 1993.

[35] I. C. on Linear Motor Analysis. "Today and Future of Linear Motor Analysis,". Technical report, (Part II) No.440, 1992.

[36] R. Parker. *Advances in Permanent Magnetism.* John Wiley & Sons, New York, 1990.

[37] Parker Hannifin Corporation. *Compumotor L drive user guide*, 1994.

[38] Parker Hannifin Corporation, Rohnert Park, CA, USA. *Compumotor Digiplan: Positioning Control System and Drives*, 1995.

[39] J. Pawletko and H. Chai. "Linear step motors,". *from the book, Theory and Applications of Step Motors, B.C. Kuo ed., West Publishing*, pages 316–326, 1974.

[40] J. Perho and E. Ritchie. "A motor design using reluctance network,". *2nd ISTC UEES'96, Szczecin and Miedzyzdroje*, pages 309–314, December 15–17, 1996.

[41] Published by *BRÜEL&KÆR. Instruction manual: Precision conditioning amplifier*, 1974.

[42] K. Rajagopal, M. Krishnaswamy, B. Singh, and B. Singh. "An improved high-resolution hybrid stepper motor for solar-array drive of indian remote-sensing satellite,". *IEEE Trans. Industry Application, vol.33, no.4*, pages 906–913, 1997.

[43] A. P. S. Wiak and J. Turowski. "Magnetostatic field calculation of 3-D non-linear model by reluctance network method (Problem No.13-Team Workshop,". *COMPEL, vol.11, No.1*, pages 217–220, 1991.

[44] M. Sanada, S. Ishikawa, and H. Takechi. "A Rotary-linear Pulse Motor with interior PM mover,". *ICEM'94 Paris, vol.3*, pages 454–459, 1994.

[45] P. Silvester and R. Ferrari. *Finite element for electrical engineers.* Cambridge University Press, Cambridge, 1983.

[46] E. So and S. Yang. "A Mathematical Model to calculate Stator Radial Vibration for a Hybrid Stepping Motor,". *ICEM'92 Manchester, UK vol.3*, pages 1030–1033, 1992.

[47] J. Turowski, M. Turowski, and M. Kopec. "Method of fast analysis of 3-D analysis of 3-D leakage fields in large three-phase transformers,". *COMPEL, vol.9*, pages 107–116, 1990.

[48] J. Wagner, D. Maga, and R. Ort-snep. "Magnetic field of high-torque stepping motor with multiphase supply,". *ISEF'95, Thessaloniki*, pages 291–294, 1995.

Appendix A

FEM implementation of Coulomb's virtual work

There are two methods that have been widely used for the evaluation of forces or torques of electro-mechanic devices with small airgap,i.e. *maxwell stress tensor* and its alternative — *virtual work* method. The former is a good choice for normal force calculation though integral path dependent, but prone to round-off errors for determination of torques or tangential forces. However, the virtual work method has been considered as a more accurate and consistent way for force and torque calculation.

Since the classical virtual work needs two solutions which are very sensitive to the selection of the amount of movement, Coulomb's virtual work uses differentiation of co-energy and needs only one solution.

A.1 Magnetic energy exact derivative concepts

A.1.1 Virtual work principle

For the majority of magnetostatic problems the current density $J \neq 0$, so the field cannot be expressed in terms of a scalar potential. Thus it is necessary to use the magnetic vector potential $\vec{A}$ which expresses the flux density $\vec{B}$ through the following equation

$$\vec{B} = \nabla \times \vec{A} \tag{A.1}$$

The magnetic energy is given by

$$F_x = -\sum_{\square e}\left(\frac{B^T}{\mu_0}\frac{\partial B}{\partial x} + \frac{B^T B}{2\mu_0}|G|^{-1}\frac{\partial |G|}{\partial x}\right)\cdot V_e \tag{A.15}$$

For linear triangular element,

$$V_e = \frac{|G|}{2} \tag{A.16}$$

To facilitate the implementation of eqns (A.15) and (A.16) into *MagNet 5.1* which employs three-node linear element for magnetic static field analysis. They need further simplifications.

A.2 Triangular element

A.2.1 Basic derivation

In this section, first the formulations for tangential force calculation will be deduced and then they are extended to their dual case, i.e. the normal force computation. For triangular elements, the Jacobian matrix becomes :

$$G = \begin{bmatrix} x_1 - x_3 & y_1 - y_3 \\ x_2 - x_3 & y_2 - y_3 \end{bmatrix} \tag{A.17}$$

If the airgap region of electro-mechanic device consists of two kinds of elements, say I and II (see Figure 1.1) and assuming that the upper nodes in the element of both types are movable and the lower nodes are fixed, the element I has two movable nodes while element II has only one node movable. Let's deal with element I first by taking partial derivatives of $|G|$

$$\frac{\partial |G|}{\partial x} = \frac{\partial |G|}{\partial x_1}\frac{\partial x_1}{\partial x} + \frac{\partial |G|}{\partial x_2}\frac{\partial x_2}{\partial x} \tag{A.18}$$

The two components can be written as :

$$\frac{\partial |G|}{\partial x_1} = y_2 - y_3 \tag{A.19}$$

$$\frac{\partial |G|}{\partial x_2} = y_3 - y_1 \tag{A.20}$$

It can be seen that it is possible to use one equation describing the virtual movement of either node by changing the subscripts of the other node as the order of node numbers satisfies certain condition (e.g. clockwise).

$$Q = \begin{bmatrix} \frac{\partial y}{\partial u} & -\frac{\partial x}{\partial u} \\ \\ \frac{\partial y}{\partial v} & -\frac{\partial x}{\partial v} \end{bmatrix} \tag{A.28}$$

and

$$B = Q^{-1} \begin{bmatrix} 1 & 0 & -1 \\ 0 & 1 & -1 \end{bmatrix} \begin{bmatrix} A_1 \\ A_2 \\ A_3 \end{bmatrix} \tag{A.29}$$

Finally,

$$B = \frac{1}{|Q|} \begin{bmatrix} A_1(x_3 - x_2) + A_2(x_1 - x_3) + A_3(x_2 - x_1) \\ A_1(y_3 - y_2) + A_2(y_1 - y_3) + A_3(y_2 - y_1) \end{bmatrix} \tag{A.30}$$

Obviously, the equation can keep the same format even when the subscripts being changed.

To make easier the matrix handling, the following functions will be defined

$$\Delta_1 = \frac{A_1(x_3 - x_2) + A_2(x_1 - x_3) + A_3(x_2 - x_1)}{|Q|} \tag{A.31}$$

$$\Delta_2 = \frac{A_1(y_3 - y_2) + A_2(y_1 - y_3) + A_3(y_2 - y_1)}{|Q|} \tag{A.32}$$

The derivative of the field (A.31) becomes :

$$\frac{\partial B}{\partial x} = \sum_e \frac{\partial}{\partial x}(\nabla N_i) \times A_i \tag{A.33}$$

and

$$\frac{\partial}{\partial x}(\nabla N_i) = -Q^{-1}\frac{\partial Q}{\partial x}\nabla N_i \tag{A.34}$$

Therefore

$$\frac{\partial B}{\partial x} = -Q^{-1}\frac{\partial Q}{\partial x}B \tag{A.35}$$

After some mathematical transformations involving the matrix calculus, the following relationships for movements in two nodes can be obtained, i.e.

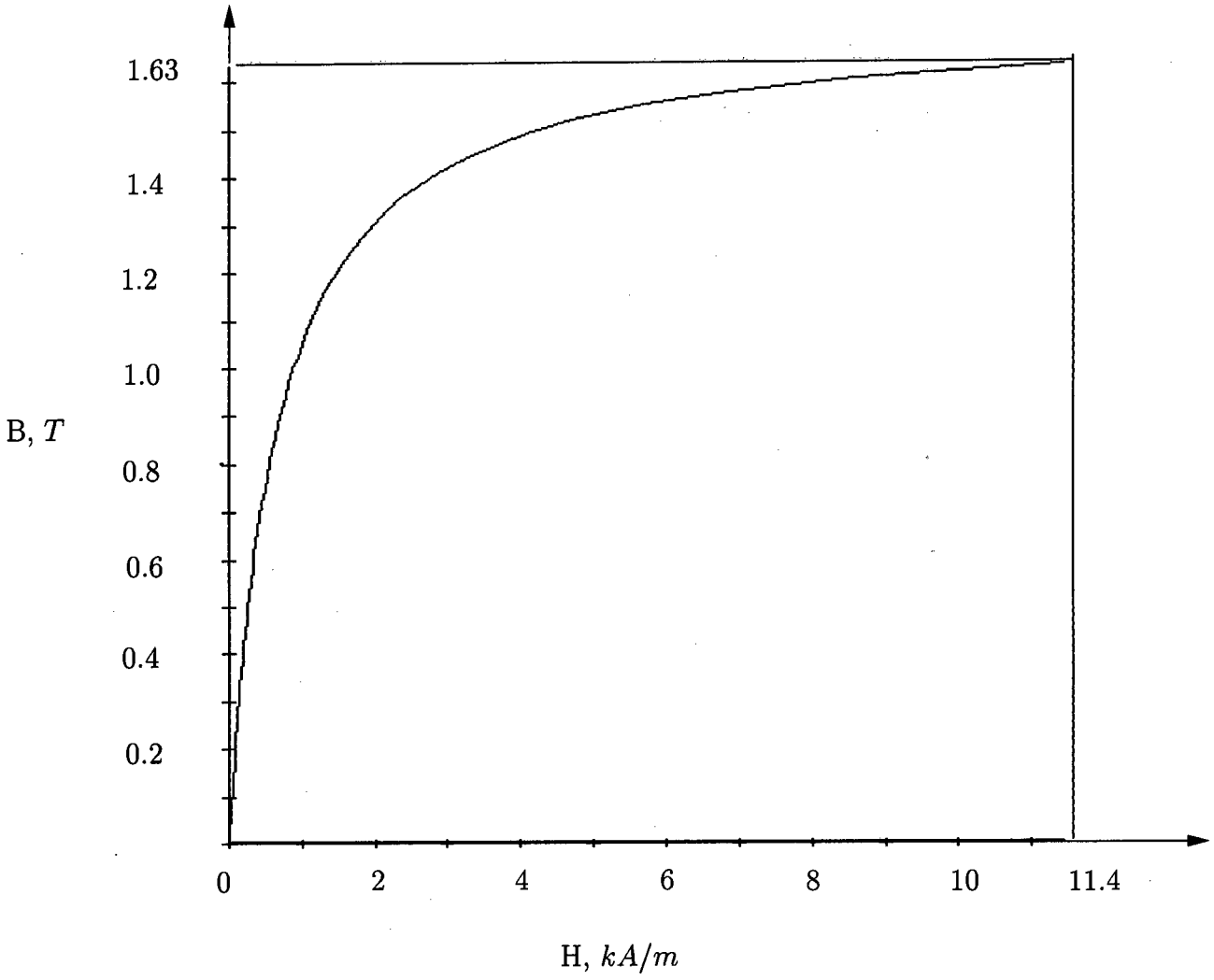

Figure B.2: B-H curve for the platen solid steel

Appendix C

Some Remarks on Calculation of Permeance by Using MagNet 5.1

In the majority of magnetostatic problems the current density **J** is not zero, so the field cannot be expressed in terms of a scalar potential. Thus many commercially available FE packages employ magnetic vector potential **A** for the magnetic field calculation.

The classical slot permeance problem with infinitely permeable iron is normally solved by electrostatic analogy by using scalar potential. Difficulties can arise when the magnetic saturation is taken into account in the calculation of permeances. The reason is that non-linear problem can not be defined in this way because of the absence of the non-linear dielectrics.

The proposed method here is to solve the problem directly. This will require an iterative approach, because the MMFs cannot be assigned directly to the boundaries of the FEmodel in *MagNet 5.1* package (only the magnetic flux can be input). The model is shown in Fig C.1.

The boundaries which would have had fixed potentials in the electrostatic analogy (i.e. with magnetic flux crossing normally) are left as natural (Neumann) boundaries. The magnetic flux line boundaries are defined as unary constraints.

The excitation is applied by assigning $\phi = 0$ to one of these, and the value to the other which represents the total flux in the problem. This is unknown, but must be estimated, (it can also be calculated from the complete model) and then successively improved on. Having obtained a solution, the next step is to switch to the *Post Processor*, and calculate the MMF difference between the two natural boundaries.

If the estimated value is reasonable, this will correspond with the MMF applied in the

Calibrated transducer range:

1 to 10999 pC/unit or mV/unit (4 digit conditioning)

Voltage sensitivity:

0.1 to 100V/V

Charge sensitivity:

0.1 to 100 mV/ pC

Output rating:

Transducer sensitivity pC/ unit or mV/ unit	Available Outputs V/ unit
1 to 11	0.001, 0.01, 0.1
10 to 110	0.01, 0.1, 1.0
100 to 1100	0.1, 1.0, 10
1000 to 11000	1.0, 10, 100

Accuracy:

better than 0.25% (0.5% in highest gain position)

Power supply:

100 to 240 VAC, 25 mA

Weight:

1.5 Kg

Max. output voltage:

± 10 V

Max. output current:

± 10 mA

Input impedance (voltage):

5 $G\Omega$ // 10 pF

Output impedance:

1Ω

Basic frequency range:

0.3 Hz to 200 KHz

Lower limiting frequency :

switchable to 0.3 and 3 Hz, and 2 KHz (3 dB limits)

Upper limiting frequency :

switchable to 1,3,10,30 and $\geq$200KHz

(3 dB limits)

Slew rate:

1 V/μs

Recovery time:

200 μs

Inherent noise:

$< 10\mu$V (Referred to input)

Figure D.2: Specifications of B&K 2650 conditioning amplifier